

AD A 051184

12

Technical Report

R 860



Sponsored by

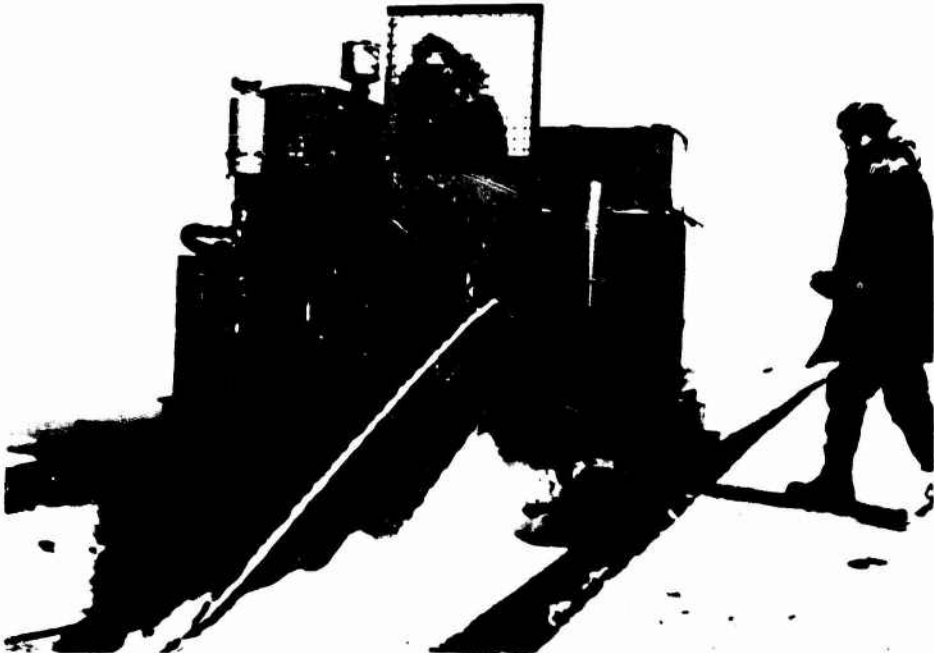
NAVAL FACILITIES ENGINEERING COMMAND

December 1977

CIVIL ENGINEERING LABORATORY

Naval Construction Battalion Center

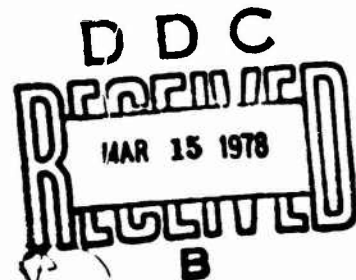
Port Hueneme, California 93043



ICE ENGINEERING - STUDY OF RELATED PROPERTIES
OF FLOATING SEA-ICE SHEETS AND SUMMARY OF
ELASTIC AND VISCOELASTIC ANALYSES

by K. D. Vaudrey, Ph.D.

Approved for public release, distribution unlimited.



Unclassified

SECURITY CLASSIFICATION OF THIS PAGE (When Data Entered)

REPORT DOCUMENTATION PAGE		READ INSTRUCTIONS BEFORE COMPLETING FORM
1. REPORT NUMBER CE -TR-860	2. GOVT ACCESSION NO. DN144027	3. RECIPIENT'S ADDRESS NUMBER <i>Crept</i>
4. TITLE (or SUBTITLE) ICE ENGINEERING - STUDY OF RELATED PROPERTIES OF FLOATING SEA-ICE SHEETS AND SUMMARY OF ELASTIC AND VISCOELASTIC ANALYSES.		5. TYPE OF REPORT OR PROGRAM COVERED Interim 1964 - 1976
6. AUTHOR(s) K. D/Vaudrey		7. PERFORMING ORG. REPORT NUMBER <i>FS2555</i>
8. CONTRACT OR GRANT NUMBER(s) <i>YF52555001.01.002; 627601 YF52555001</i>		9. PROGRAM ELEMENT, PROJECT, TASK AREA & WORK UNIT NUMBERS <i>Dec 1977</i>
10. CONTROLLING OFFICE NAME AND ADDRESS Naval Facilities Engineering Command Alexandria, Virginia 22332		11. NUMBER OF PAGES 81
12. MONITORING AGENCY NAME AND ADDRESS (if different from Controlling Office)		13. SECURITY CLASS. OF THIS REPORT Unclassified
14. DISTRIBUTION STATEMENT (of this Report) Approved for public release; distribution unlimited.		15a. DECLASSIFICATION/DOWNGRADING SCHEDULE <i>12/83 p.</i>
16. DISTRIBUTION STATEMENT (of the abstract entered in Block 10, if different from Report)		
17. SUPPLEMENTARY NOTES This study completes effort on study of sea-ice properties.		
18. KEY WORDS (Continue on reverse side if necessary and identify by block number) Ice mechanics, sea ice, tensile strength, flexural strength, compression strength, elastic modulus, creep behavior, fractured toughness, relaxation functions, field tests, load bearing prediction, elastic and viscoelastic finite element analytic techniques.		
19. ABSTRACT (Continue on reverse side if necessary and identify by block number) This report summarizes approximately 12 yr of research effort by the Civil Engineering Laboratory (CEL) for developing engineering data and analytical capability for calculating operational bearing capacity of sea-ice sheets. The objectives of the report are: (1) to summarize the CEL elastic and viscoelastic experimental programs; (2) to review the two CEL-developed finite-element techniques for analyzing the structural behavior of the <i>next page</i> continued		

DD FORM 1 JAN 73 1473 EDITION OF 1 NOV 65 IS OBSOLETE

Unclassified

SECURITY CLASSIFICATION OF THIS PAGE (When Data Entered)

iii 391 111

PRECEDING PAGE BLANK-NOT FILMED

Unclassified

SECURITY CLASSIFICATION OF THIS PAGE (When Data Entered)

20. Continued

material; and (3) to present bearing capacity limits for both short- and long-term ice-sheet operations.

At the outset of this research program little engineering data and only limited analytical techniques were available to assist the practitioner in evaluating ice-sheet bearing strength. Though much still remains to be learned, it is now possible to make qualitative engineering predictions on bearing strength as a result of the comprehensive laboratory and field research program directed at defining the tensile strength, compressive strength, flexural strength, elastic modulus, creep behavior, and their relationship to temperature and salinity. Bearing strength analysis, using the CEL-developed finite-element computer codes, can now be based on the material properties corresponding to the actual temperature and salinity gradient existing across the vertical profile of the ice plate.

Library Card

Civil Engineering Laboratory
ICE ENGINEERING - STUDY OF RELATED PROPERTIES
OF FLOATING SEA-ICE SHEETS AND SUMMARY OF
ELASTIC AND VISCOELASTIC ANALYSES by K. D. Vaudrey
TR-860 81 p illus Dec 1977 Unclassified

1. Sea-ice measurements

2. Finite element analyses

I. YF52.555.0+1.01.002

This report summarizes approximately 12 yr of research effort by the Civil Engineering Laboratory (CEL) for developing engineering data and analytical capability for calculating operational bearing capacity of sea-ice sheets. The objectives of the report are: (1) to summarize the CEL elastic and viscoelastic experimental programs; (2) to review the two CEL-developed finite-element techniques for analyzing the structural behavior of the material; and (3) to present bearing capacity limits for both short- and long-term ice-sheet operations.

At the outset of this research program little engineering data and only limited analytical techniques were available to assist the practitioner in evaluating ice-sheet bearing strength. Though much still remains to be learned, it is now possible to make qualitative engineering predictions on bearing strength as a result of the comprehensive laboratory and field research program directed at defining the tensile strength, compressive strength, flexural strength, elastic modulus, creep behavior, and their relationship to temperature and salinity. Bearing strength analysis, using the CEL-developed finite-element computer codes, can now be based on the material properties corresponding to the actual temperature and salinity gradient existing across the vertical profile of the ice plate.

Unclassified

SECURITY CLASSIFICATION OF THIS PAGE (When Data Entered)

CONTENTS

	page
INTRODUCTION	1
SEA-ICE PHYSICS	1
Macrostructure of Sea Ice	2
Microstructure of Sea Ice	3
Laboratory Sea-Ice Characteristics	4
Tensile Strength	9
Compressive Strength	12
Flexural Strength	18
Elastic Modulus	21
Fracture Toughness	25
Creep Behavior	29
ANALYSIS OF FLOATING ICE SHEETS	39
Elastic Plate on an Elastic Foundation	39
Elastic Finite Element Method	41
Viscoelastic Finite-Element Technique	44
BEARING CAPACITY OF FLOATING ICE SHEETS	49
Failure Criteria	49
Computer Code Input Parameters	50
Aircraft Load Curves	51
Vehicle Ice Thickness Table	51
Allowable Parking Times for Aircraft	52
Operational Field Procedure	52
CONCLUSIONS	52
RECOMMENDATIONS	55
ACKNOWLEDGMENTS	56
REFERENCES	56

JUSTIFICATION		
BY _____		
DISTRIBUTION/AVAILABILITY CODES		
Dist.	U.L. End / or	SPECIAL
A		

METRIC CONVERSION CHART

ft	meter (m)	3.048 000 E-01
gm/cm ³	kilogram/meter ³ (kg/m ³)	1.000 000 E+03
in.	meter (m)	2.540 000 E-02
in./in. sec ⁻¹	meter/meter-sec ⁻¹ (m/m·s ⁻¹)	2.540 000 E-02
in./min	meter/second (m/s)	4.233 000 E-04
psi (lb/in. ²)	pascal (Pa)	6.894 757 E+03
psi/sec	pascal/second (Pa/s)	6.894 757 E+03
°F	Celsius (C)	(°F - 32) x 0.556

INTRODUCTION

In recent years operational use of ice-covered waters in polar regions has greatly increased to coincide with the advent of a world-wide energy crisis. No longer can remote polar locations be considered too inhospitable or uneconomical to search for or harvest energy resources. In particular, Naval Antarctic operations continue to depend on sea-ice airfields and roads to provide heavy cargo and logistics support for United States activities. Therefore, a better understanding of the behavior of sea-ice sheets under aircraft and vehicular loading is required to ensure continued safe operations. To this end the Civil Engineering Laboratory (CEL) was initially engaged in performing experiments and developing analyses in which sea-ice sheets were assumed to behave elastically (1, 2, 3). The culmination of this elastic-properties research on sea ice was the development of an elastic finite-element computer code that has the capability of modeling temperature-dependent properties as a function of ice sheet thickness (4).

However, it is known that sea ice behaves elastically only for small to moderate load magnitudes applied over short time durations. Consequently, parked aircraft, cargo storage, over-ice platforms or stations, and even snow overburden cannot be correctly analyzed by elastic-behavior solutions to determine their actual effect on ice sheets. To define the range of greater load magnitudes and longer time durations, CEL conducted another series of laboratory and field experiments on the

creep behavior of sea ice. The theory of linear viscoelasticity was coupled with the finite-element technique to provide more realistic characterization of sea-ice sheet behavior (5).

The objectives of this report are: (1) to summarize the CEL elastic and viscoelastic experimental programs; (2) to review both finite-element techniques developed by CEL for ice-sheet analysis; and (3) to present bearing capacity limits for both short- and long-term ice-sheet operations.

SEA-ICE PHYSICS

Before proceeding with mechanical properties experimental programs on sea ice, it is necessary to review physical material properties of sea ice to understand its structure and provide insight into its behavior under load. Sea ice is sensitive to several influential parameters, e.g., salinity, temperature, crystal orientation, density, and seasonal changes. A typical phase diagram is presented in Figure 1 that shows the relationship between ice, brine, and solid salts as a function of temperature (6). For any specified temperature this diagram gives the relative volume of brine, ice, and solid salt in the system, as well as depicting the temperatures of crystallization of the major solid salts found in sea ice. This figure assumes that ion distribution is the same as in standard seawater; thus, any selective brine drainage would cause changes in this standard sea-ice phase diagram. Once these relative volumes of major sea-ice components are established, it is

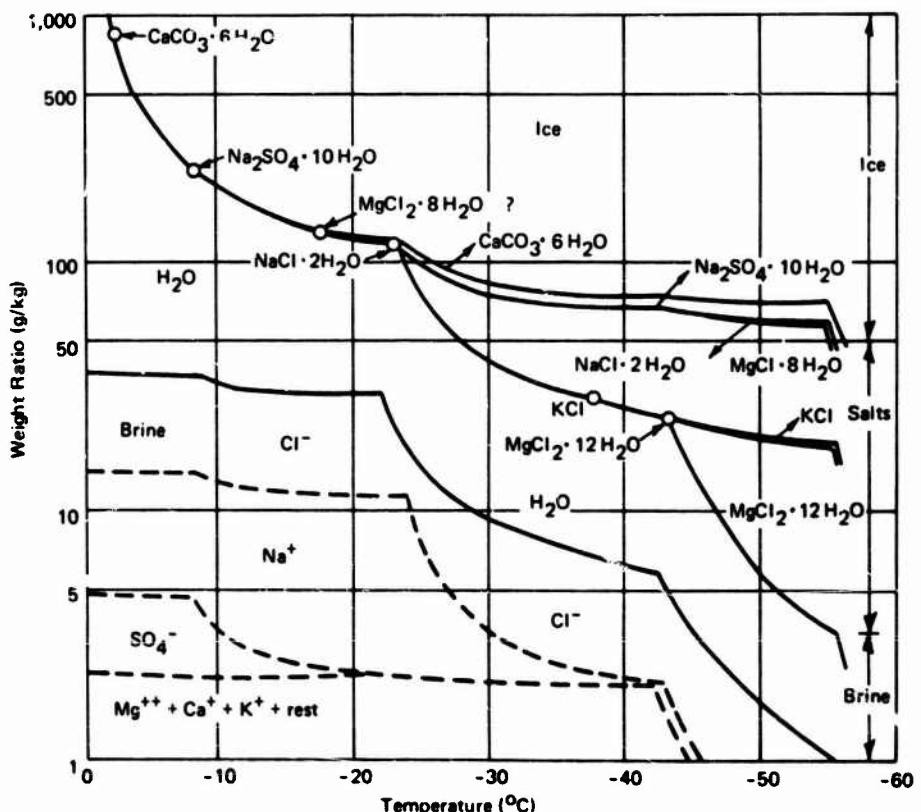


Figure 1. Phase diagram for sea ice (after Assur, Reference 7).

important to understand how sea ice forms, both its macrostructure and microstructure.

Macrostructure of Sea Ice

A sea-ice sheet begins to grow as minute spheres that quickly change into thin, wafer-like discs, and then into star-like crystals which float on the surface. These stars grow rapidly, overlap, and start to freeze together into a thin ice skim. If the water should remain calm, this ice skim would have a completely vertical c-axis orientation. However, since the water surface can never be perfectly calm, a number of star crystals

get tipped and caught with an inclined c-axis.

At this stage, the growth rate is determined by the thermal gradient in the young ice sheet. Those ice crystals with a vertical c-axis grow slower than the surrounding horizontal c-axis crystals. Thus, any tendency toward anisotropic growth produces geometric selection, finally eliminating all but those crystals having a horizontal c-axis. This transition takes place in a very thin surface layer, commonly only 1 to 2 in. thick. Because the transition layer is thin, it often sublimes away or recrystallizes into the snow cover. Therefore, over a single ice-growth season, a sea-



Figure 2. Horizontal thin section of natural seawater ice enlarged to show grain and subgrain structure. The grid is 1 cm on a side.

ice sheet can be considered to be columnar throughout its thickness. Columnar sea ice means that it has strong crystal elongation parallel to the direction of heat flow, a definite crystal orientation, and an increase in crystal size at the growth front (bottom) of the ice sheet. Average crystal diameter is about 0.4 in. at a level 12 in. below the ice-sheet surface.

Microstructure of Sea Ice

When seawater freezes, the dissolved salts are rejected by the ice, causing a solute concentration in "pockets" of liquid brine. Each sea-ice crystal forms as a "packet" of plates separated by an array of brine pockets. As shown in Figure 2, a single crystal can be identified easily under crossed

polaroids, since it forms a common extinction unit. There is a random orientation of crystal c-axes in a horizontal plane, but within each crystal the c-axis has only one horizontal direction.

Brine pockets are generally tubular cells standing vertically in the ice sheet. The distance between adjacent rows of brine pockets, parallel to the c-axis, is called the plate spacing. The spacing does vary with position in the ice sheet due to changes in growth velocity, but the distance is on the order of 0.02 in. On the other hand, the distance between individual brine pockets at a single plate interface varies much more than the plate spacing, primarily due to temperature. As ice temperatures become colder, sea ice will have smaller and more widely spaced brine pockets due to freezing of the water and precipitation of solid salts from the brine.

When analyzed structurally, a potential intragranular failure between cold ice plates would occur on a plane having a larger percentage of ice. Thus, sea ice should have a much higher strength at colder temperatures. A structural theory (7) has been developed relating sea-ice strength to a material property called brine volume, v , a function of ice temperature and salinity. Consequently, the following section describes the different ranges of test parameters used in the sea-ice mechanical properties experimental program and the rationale behind their selection.

Laboratory Sea-Ice Characteristics

As a naturally occurring material, sea ice is sensitive to several environmental parameters (e.g., salinity, temperature, seasonal changes, crystal orientation). To isolate and control these parameters, CEL has conducted comprehensive mechanical property studies in a cold-chamber environment, supplemented by appropriate field experiments to provide data checkpoints. An insulated freezing tank, 64 in. by 101 in., provided unidirectional ice growth from the surface to duplicate the natural environment for sea-ice growth (8). Since the freezing tank was not equipped for circulating the water to maintain constant salinity, the ice was grown from water that increased in salinity as brine was rejected during ice growth. Such a freezing system has previously been defined as a closed system (9).

During the freezing cycle for all ice production the temperature was maintained at -29°C. Prior to freezing, the water was prechilled to a temperature of 0.5°C to 1.5°C. During the prechill, the water was occasionally mixed to reduce chill time and temperature stratification. The freezing cycle was maintained

until there was an ice growth of 22 to 24 in.; from this point, the temperature of the chamber was adjusted to the scheduled test temperatures. Ice that formed after the beginning of the test phase was excluded from the sampling.

The salinity of the water under the ice sheet at the end of the freezing cycle was in the range of 60 ppt for the natural seawater ice and 9.5 ppt for the brackish water ice. Freezing and testing of the ice were performed in the same cold chamber, with the temperature fluctuating $\pm 2.2^\circ\text{C}$ from a given test or freezing temperature. The temperature cycle was sufficiently short to produce no observable effect on the steady-state temperature of the test specimens.

Test Temperature. The ice test temperatures, -4, -10, -20, and -27°C, were initially chosen to bracket the precipitation points of the two major salts in normal seawater: sodium sulfate ($\text{Na}_2\text{SO}_4 \cdot 10\text{H}_2\text{O}$) with a precipitation point of -8.2°C, and sodium chloride ($\text{NaCl} \cdot 2\text{H}_2\text{O}$) with a precipitation point of -23.3°C (see Figure 1). By performing strength property tests at temperatures on both sides of the major salt precipitation, the effects, if any, of solid salt reinforcement could be observed.

Salinity. Natural seawater was used to provide a laboratory sea ice of 7 to 9 ppt salinity for tensile, flexural, compression, and shear strength experiments. Also, tensile, flexural, and shear strength experiments were run on 1-to-2-ppt brackish ice, a mixture of distilled water and natural seawater. Representative salinity profiles for tanks containing both types of ice are shown in Figures 3 and 4. The most distinguishing feature contrasting the vertical profiles of the two ice types, aside from difference in actual salinity value, is a more uniform

salinity distribution for the brackish ice and its very low surface salinity. The 8-to-9-ppt salinity of the natural seawater ice, which began at about the 4-in. depth, is fairly typical of salinities reported for young natural sea ice (10). The representative horizontal salinity profiles in Figure 4 demonstrate a fairly uniform distribution, and they are in good general agreement with the vertical profile data at the same depth.

Brine Migration. To investigate effects of season changes and detect brine migration, salinity profiles associated with thermal activity in several laboratory-grown sea-ice blocks were plotted (Figure 5). The predominant shift in salinity distribution was in the top 5 in. of the ice block. In blocks B and C, the decrease was 8 ppt and 5 ppt, respectively, in the surface stratum between the first and second samplings. No shift was observed between the second and third samplings. Prior to the second sampling, both ice blocks had been subjected to a condition of thermal stability; that is, the temperature environment had remained constant. Between the second and third samplings, both ice blocks had been subjected to a condition of thermal activity by the temperature change. The brine loss in the upper stratum is weakly indicated by the peaking trends picked up in the lower stratum for the second and third samplings; however, no appreciable degree of brine migration developed, even under thermal activity, during the 800-to-1,000-hour observation period. The early loss of salinity in the first few inches of the surface stratum occurred during a condition of thermal stability.

Density. The ice density for natural seawater was found to center around

0.920 to 0.925 gm/cm³, while that for brackish ice was found to be slightly less, with mean values ranging from about 0.900 to 0.915 gm/cm³. Representative density profiles are presented in Figure 6. Both liquid displacement and dimension measurement techniques were used to calculate volumes.

Grain Size. The laboratory-grown sea ice was very similar in petrographic structure to natural sea ice, having almost identical plate spacing (between 0.3 and 0.5 mm). However, this distance increased to almost 1.0 mm for brackish ice. A pronounced increase in grain size with depth was noted for natural seawater ice, while grain size variation was less evident for brackish ice (see Figure 7).

MECHANICAL PROPERTIES OF SEA ICE

In formulating a comprehensive experimental program for measuring mechanical properties of sea ice, every attempt was made to isolate variable parameters and to carefully record testing conditions. In addition to the sea-ice characteristics described previously, it is known that sea ice under load behaves differently, depending on whether the stress is applied perpendicular or parallel to crystal growth. Laboratory tests were conducted to determine the strength of ice specimens extracted both horizontally and vertically from the ice block. All of the strength values obtained for each loading condition are related to the square root of brine volume, which is expressed as a function of salinity and ice temperature. The following sections discuss several strength property test series performed on sea ice.

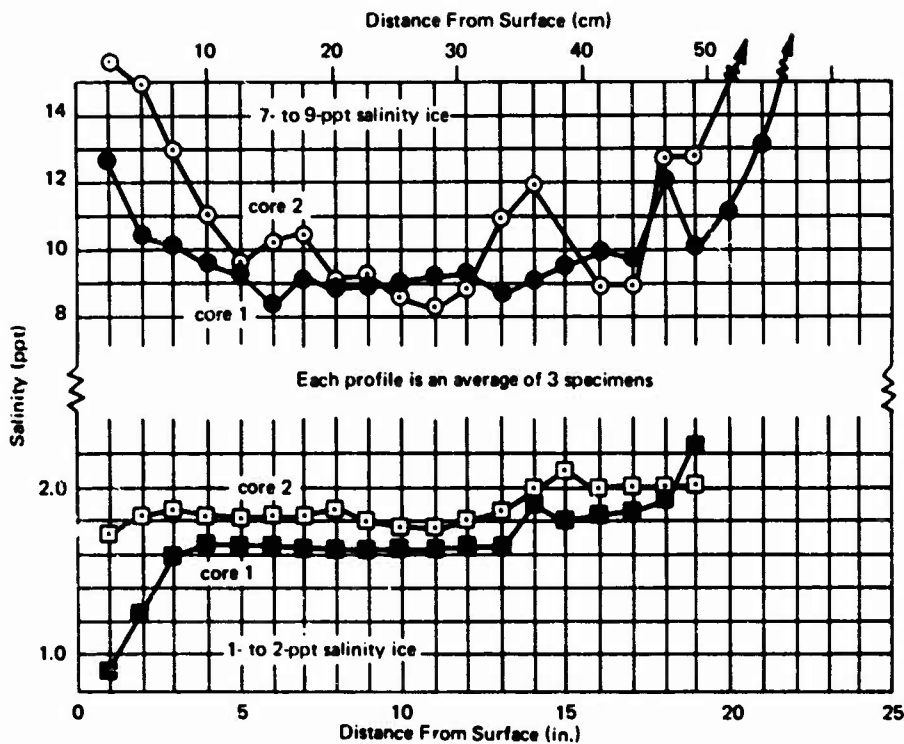


Figure 3. Vertical salinity profiles.

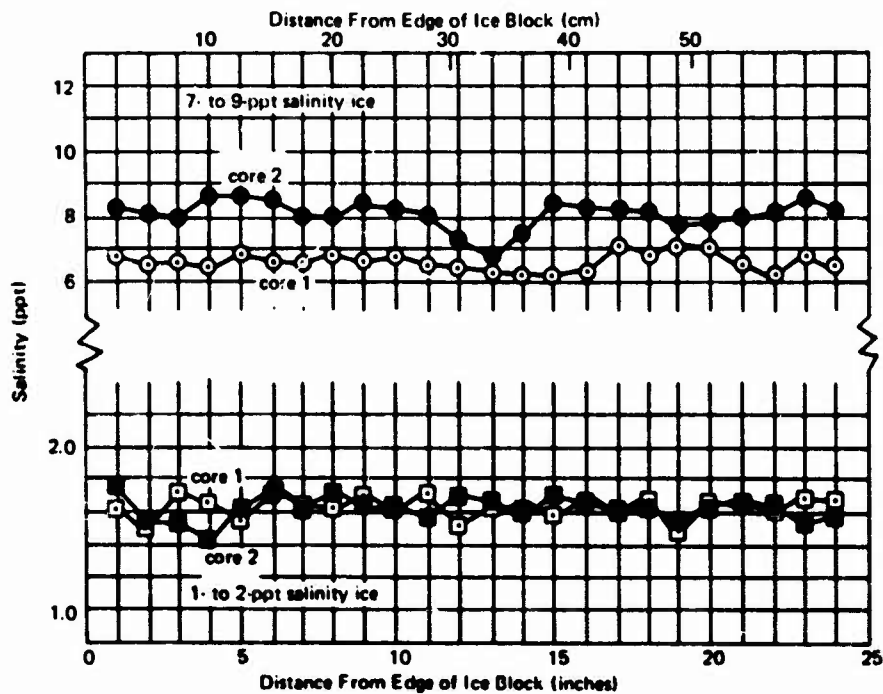


Figure 4. Horizontal salinity profile 6 in. below surface.

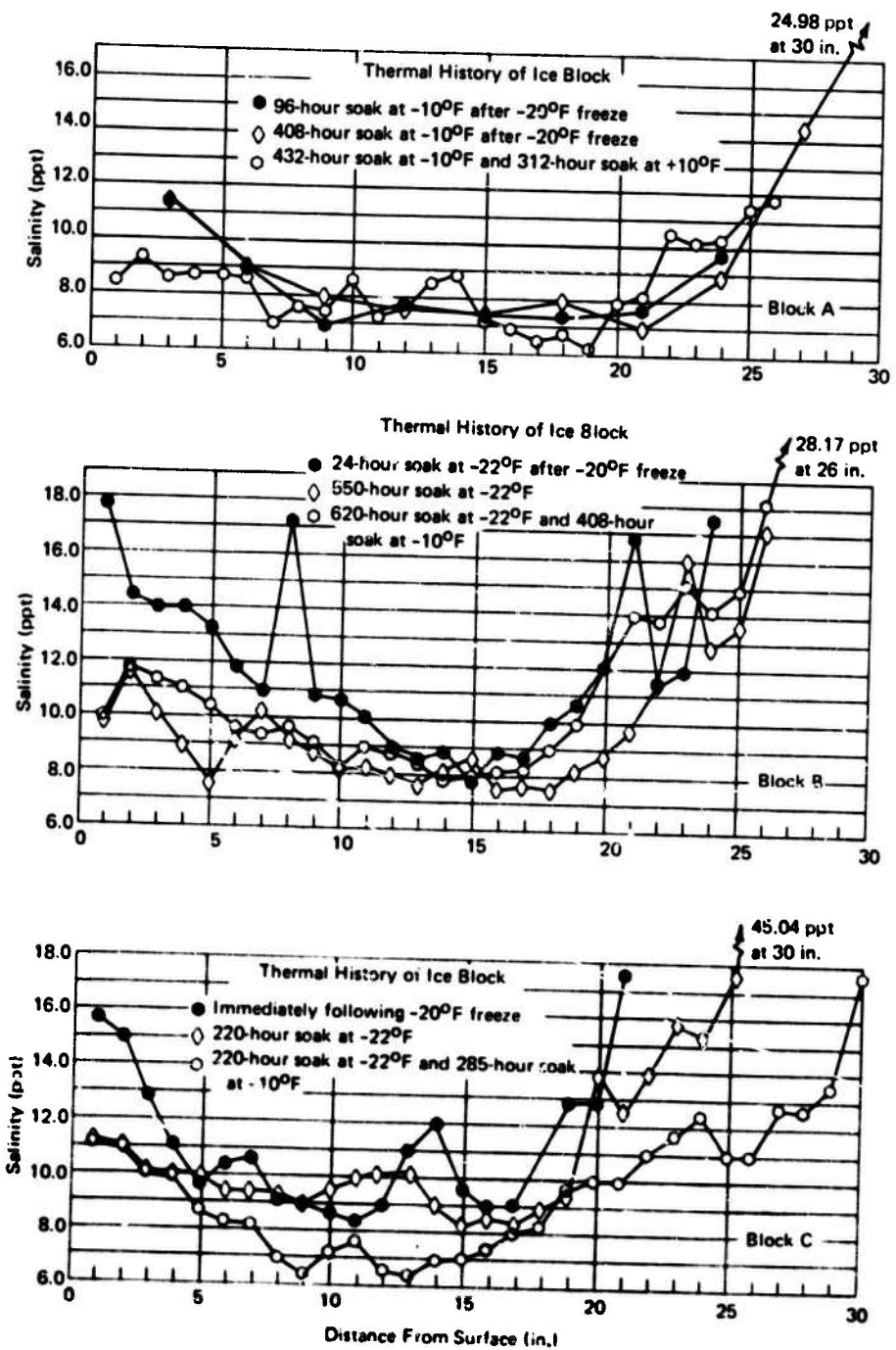


Figure 5. Vertical salinity profiles of seawater ice showing extent of salinity change or migration of brine during a variable thermal regime.

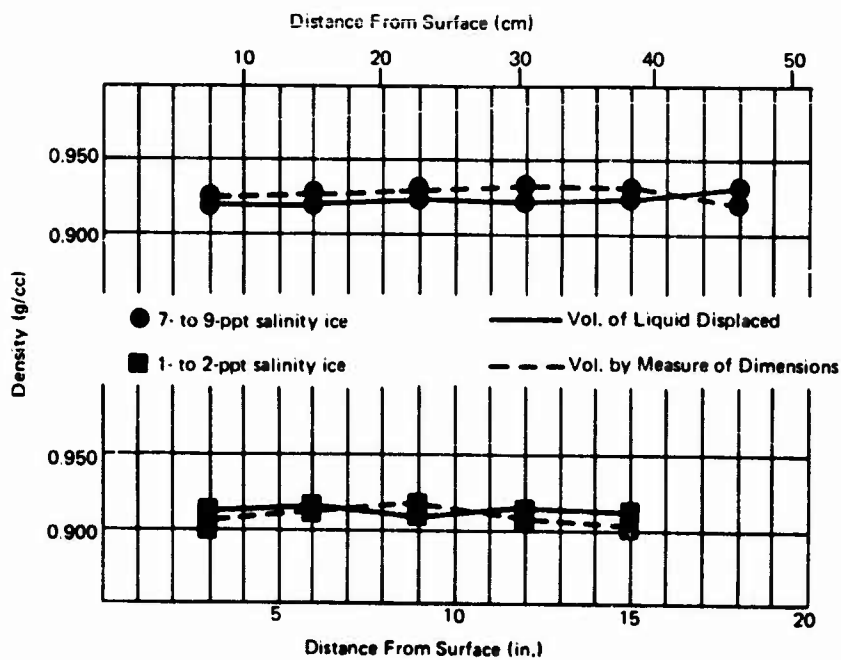


Figure 6. Vertical density profiles.

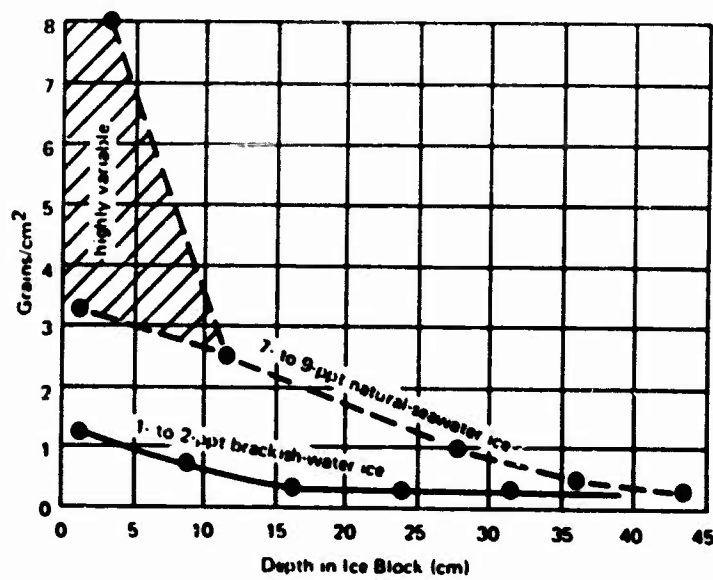


Figure 7. Increase in grain (crystal) size with depth.

Tensile Strength

Tensile strength is best determined by direct uniaxial tension testing. Any substitute for the direct test method, such as ring tensile, brazil, or flexural tests, induce complicated stress states within the sample that must be taken into account when calculating the test results. However, uniaxial tensile testing for brittle materials is extremely sensitive to any slight stress concentrations that can cause premature failure and give erroneous results. Therefore, special care was taken in designing the testing method and preparing the ice specimens.

Preparation of Dumbbell Ice Specimens. Tensile tests were performed on dumbbell-shaped ice specimens to reduce end-effect errors. First, rough cylindrical cores were extracted from sawed blocks cut out of laboratory-grown sea ice and cut into right circular samples by using a cut-off saw. A special alignment tray to hold the samples during cutting was necessary to ensure plane and parallel ends. These cylindrical specimens were cut approximately three core diameters long to provide a test section length of approximately one core diameter. The test section diameter was one-half of the core diameter. The transition region between the test section and enlarged ends must avoid stress concentrations due to short-radius fillets. For this reason a transition radius was chosen almost equal to the core diameter - large enough to minimize possible stress concentrations. The tensile ice specimens were machined on a regular metal-turning lathe, using a single compound cutting tool to form the radius and contact seat for mating with the test head. The entire machining setup is shown in Figure 8. After machining, the dumbbell specimens were cold-soaked at the test temperature for 3 to 4 hours prior to testing.

Tensile Pulling System. Most past tensile testing procedures have favored freezing the dumbbell ice specimen into metal end caps (11). As an alternative, CEL developed a tensile pulling system that consisted of split aluminum end cups with a load-applying pin insert and a keeper ring; the end cups were machined to receive the finished ice specimen. Both the gripping heads and a dumbbell ice specimen are shown in Figure 9. The truncated conical section of the ice specimen bears on its mating cup holder surface and transmits the uniaxial load without freezing the specimen in. Alignment of the testing machine was periodically checked, and a universal joint was inserted to ensure concentric load application. This system has certain flexibility to readjust the specimen after preloading to check opposing strain output. In most cases, however, the specimen slid into proper position guided by the beveled bearing surface. This gripping technique made testing easier to perform, thus allowing a greater number of specimens to be tested.

To check the alignment of the tool, a model ice specimen was machined out of acrylic plastic, a photoelastic material. The fringe pattern symmetry shown in Figure 10 indicates uniform tensile stress in the test section. Photoelastic stress distributions were checked at four different angles around the specimen. Since birefringence is a function of thickness, a plot of the number of fringes over the diameter should describe a semicircle, another check on stress uniformity. In addition to this photoelastic test, the same acrylic specimen was strain-gaged at three points, 120 deg apart, around the circumference of the test section. Surface strains were checked under different tensile loads for uniformity. The strain measurements from the three gages were found to be within 3 to 5% of each other for three separate loading and unloading cycles.

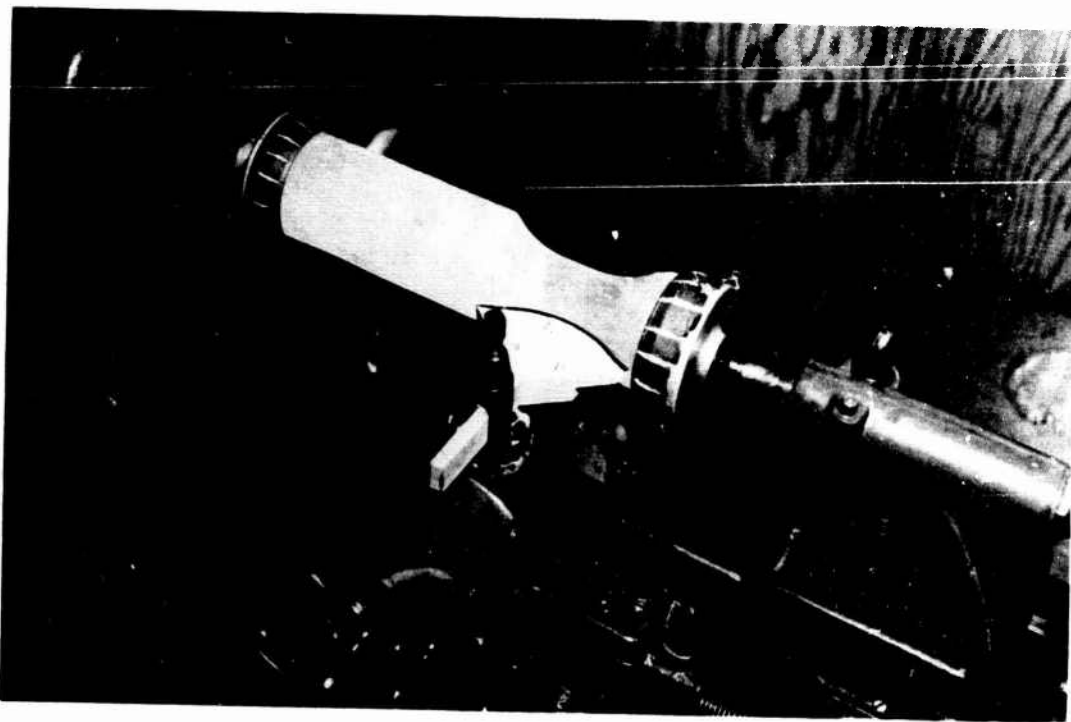


Figure 8. Machining tensile specimen with compound cutting tool.

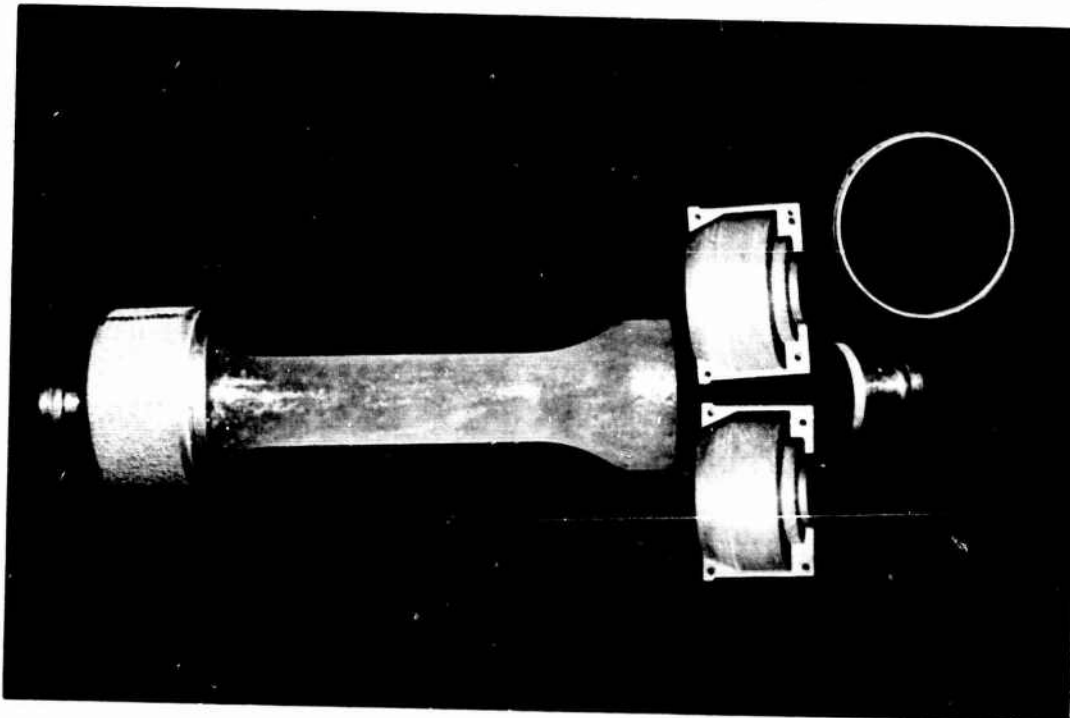


Figure 9. Tensile specimen and gripping heads.

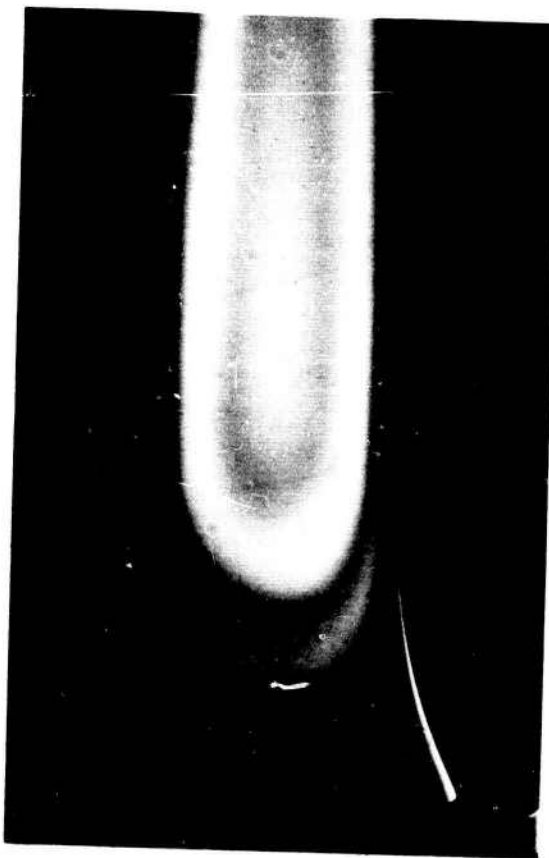


Figure 10. Symmetric fringe pattern in model of dumbbell specimen under tension.

Testing Procedure. All tensile ice specimens has a nominal 1.6-in. diameter to ensure failure without end effects; strength calculations were based on actual diameter. The test frame (a 10,000-lb universal testing machine) was located in the cold chamber to maintain a constant specimen temperature during the test. A constant crosshead velocity of 0.5 in./min was maintained throughout the tests to provide an elastic ice response. This produced a stress loading rate of 15 to 35 psi/sec for horizontal specimens and 25 to 45 psi/sec for vertical specimens. A special test series indicated the horizontal tensile strength

of sea ice to be virtually independent of the applied stress rate within the above ranges of stress loading rate (2). Every sea-ice specimen loaded in tension failed by cleavage, producing, in general, a smooth failure plane perpendicular to the axis of the applied load.

Laboratory Results. The laboratory series of uniaxial tensile tests on sea ice included four test temperatures (-4, -10, -20, and -27C), two sample orientations (horizontal and vertical), and two salinity ranges (7 to 9 ppt and 1 to 2 ppt). The sample population ranged from 38 to 138 for each of the 16 possible combinations of the above parameters. A summary of the tensile strength results is shown in Figure 11 as a function of the square root of the brine volume, v . The average of each sample group is plotted with a 95% confidence level. These statistical limits indicate that if another sample group were to be tested with the same variables held constant, there would be a 95% chance the mean of that sampling would lie within the confidence interval. A curve-fitting technique, employing linear regression by the method of least squares, is used to determine straight-line equations for both horizontal and vertical tensile strengths, σ_{th} and σ_{tv} , respectively, where σ_t is found in lb/in.² and v in parts per thousand.

$$\sigma_{th} = 118 - 10.0 \sqrt{v} \quad (1)$$

$$\sigma_{tv} = 224 - 12.7 \sqrt{v} \quad (2)$$

By the least-squares method, different sample groups from both salinity levels are averaged and weighted by the amount they differ from the mean. Both Equations 1 and 2 are plotted on Figure 11. The y-intercept of these equations

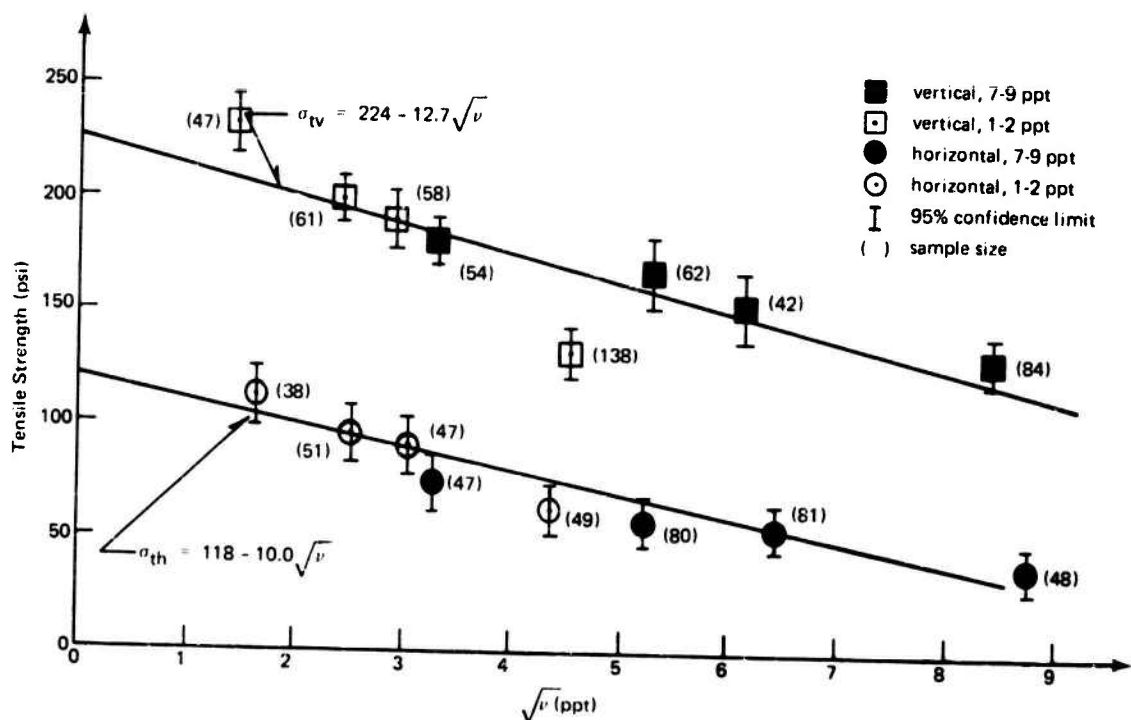


Figure 11. Tensile strength versus brine volume.

indicates the tensile strength of ice having zero brine content, but the same structure as sea ice. The negative slope indicates the strength of ice deteriorates as v increases; i.e., as the salinity increases and/or ice temperature becomes warmer. Complete test results on CEL's tensile strength of sea ice are presented in References 1 and 2.

Compressive Strength

Laboratory and Field Test Results. Both extensive laboratory and Antarctic field studies were performed on right-circular cylinders of sea ice loaded elastically in compression to failure (12). Each specimen had a length-to-diameter ratio of 2:1. The laboratory test series included four test temperatures (-4, -10, -20, and -27°C), two specimen orientations (horizontal and vertical), and one

salinity level (7 to 9 ppt). The sample population ranged from 46 to 81 for each of these eight combinations of sensitive parameters. Loadhead speed was kept constant at 0.5 in./min, producing a strain rate on the order of 10^{-3} in./in. sec $^{-1}$. Both the load and longitudinal deflection were monitored during each test.

The field test series included just two ice temperatures (-4 and -10°C) and only the vertical crystal orientation. The salinity range (4 to 6 ppt) was considerably lower than normal young sea ice, since the test specimens were extracted from year-old sea ice.

While every attempt was made to eliminate salinity as a variable, the average salinity varied 1 to 2 ppt within the 7-to-9-ppt range. In Figure 12 both horizontal and vertical compressive strength are plotted as a function of the

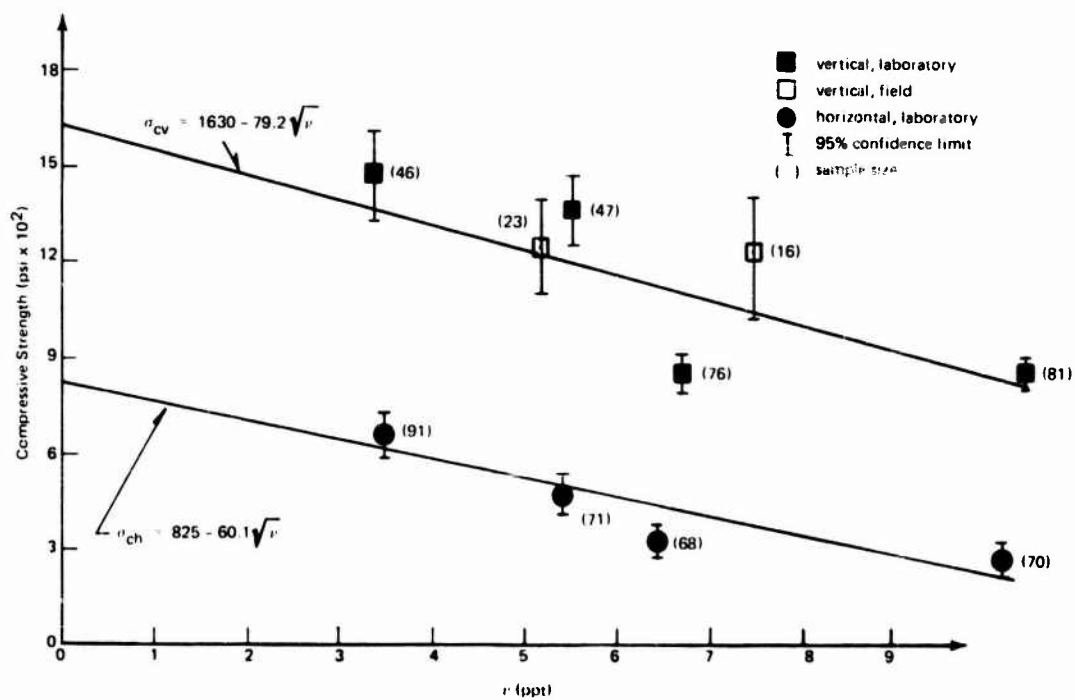


Figure 12. Compressive strength versus brine volume.

square root of brine volume, v , again using the linear regression technique called the least-squares method. By this method different data groups, shown in Figure 12 as individual points with 95% confidence limits, are averaged, weighted by the amount they differ from the mean, and approximated by straight lines governed by the following equations:

$$\sigma_{ch} = 825 - 60.1\sqrt{v} \quad (3)$$

$$\sigma_{cv} = 1,630 - 79.2\sqrt{v} \quad (4)$$

where σ_{ch} and σ_{cv} are the horizontal and vertical compressive strength (lb/in.²) of sea ice, respectively. Again the y-intercept of the above equations simply indicates the compressive strength of ice

having no brine content but the same as sea ice.

It is interesting to compare the least-squares analyses of the uniaxial tensile strength tests with those of the uniaxial, unconfined compression experiments. Two significant findings can be determined from the ratios that show the relationships between (1) tensile and compressive strengths for each specimen orientation and (2) horizontal and vertical specimen orientation for each uniaxial loading mode. First, both the horizontal and vertical compressive-to-tensile strength ratios are approximately 7:1, using the zero brine values for comparison. Second, both the compressive and tensile vertical-to-horizontal strength ratios are approximately 2:1, again comparing zero brine volume values.



Figure 13. Horizontal, compression specimen tested at -20°C, showing typical shear failure.

Compressive Failure Modes. The modes of failure of compressive sea-ice specimens vary, depending on ice temperature, specimen crystal orientation, end restraints, and strain rate during testing. The strain rate was held constant at 10^{-3} in./in./sec $^{-1}$ for these particular tests. Of course, compression itself does not tend to form or propagate cracks and, thus, cause failure. But the same does not hold true for the secondary tensile and shear stresses generated during uniaxial compression (13). In brittle materials, such as very cold sea ice, tested at relatively high strain rates, shear fractures inclined to the compression axis are quite common (Figure 13).

Another typical failure mode of cylindrical specimens is fracturing along a plane parallel to the compression axis. This is termed axial cleavage and is

caused by secondary tensile stresses in the end thirds of the specimen. Theoretically, these tensile stresses can attain values up to one-half of the axial compressive stress. However, they generally are suppressed by friction between the heads of the testing machine and the specimen. This end restraint causes an abnormal increase in the required compressive load in order to build up the tensile stresses sufficiently to cause failure. End confinement can be reduced by placing low friction material, such as Teflon, between the loadheads and specimens. Alternatively, platen-specimen matching can provide the condition of equal radial strain by forcing the quotient of Young's modulus divided by Poisson's ratio to have the same value for both specimen and platen materials (11). To study the effects of

friction-reducing materials on compressive strength, CEL undertook a small-scale laboratory effort discussed in a later section.

Almost all of the horizontal ice specimens tested in compression failed in shear, with higher temperature (-4 and -10C) specimens failing less demonstrably than those at lower temperatures; that is, they developed a series of small, criss-crossing shear cracks, but remained intact. The greater density of brine inclusions at these higher ice temperatures may create more points of stress concentration which ultimately reduce the load-carrying capacity of the specimen without its destruction. At lower temperatures a more definitive shear plane develops, because the sea ice has become a more homogeneous crystalline material after increasing salt precipitation.

Occasionally, vertical ice specimens demonstrated a cleavage failure due to secondary tensile stresses developing perpendicular to the crystal growth. These tensile stresses tend to separate crystals at their boundaries or within crystals at platelet boundaries. This failure mode may govern, particularly under higher load rates (~300 to 400 psi/sec), since tensile stresses develop spontaneously as axial compression is rapidly applied.

Strain Rate Effects. It is known that different loading rates affect compression testing significantly; therefore, a series of strain-rate compressive strength experiments was performed on laboratory-grown sea ice. The tests were conducted at two different ice temperatures (-10 and -20C) on right-cylindrical samples cored both parallel to (vertical) and perpendicular to (horizontal) the direction of crystal growth. Average values for the square root of the brine volume, v , were 6.10 ppt for -10C and

5.20 ppt for -20C. The cylindrical ice cores had either a 2- or 3-in. diameter and were cut having a length-to-diameter ratio of 2:1. No special friction-reducing material was employed between the loading platens and ice specimens. Crosshead travel speeds ranged from a high of 20 in./min to a low of 0.05 in./min. In Figures 14 and 15 both horizontal and vertical compressive strengths are plotted, respectively, for two ice temperatures and one complete range of loading strain rates. All of the curves show a maximum compressive strength occurring at or near 8.5×10^{-4} in./in. sec $^{-1}$, which corresponds to 0.5 in./min crosshead speed of loading machine. Shear failure planes were the predominant feature in most of the horizontal ice specimens (Figure 16); however, at the faster rates, several specimens failed abruptly by cracking vertically due to secondary tensile stresses (Figure 17). This latter behavior pattern was universal in the vertical ice cores, but instead of a single separation, they fractured at grain boundaries to form many splintered bundles of columnar ice crystals.

Failure planes develop more slowly corresponding to slower loading rates. Even though the ice specimen remains intact at slower rates, obviously greater longitudinal deformation and more microcracking have occurred due to plastic flow. Plastic flow is the sole cause of failure below 3.4×10^{-4} in./in. sec $^{-1}$, while above 8.5×10^{-4} in./in. sec $^{-1}$ sea-ice specimens behave in a brittle manner. As the load is rapidly applied, a bursting process follows the occurrence of brittle cleavage cracks and the linkage of grain boundary micro-cracks. There appears to be a transition phase between brittle and ductile response at loading rates ranging from 3.4×10^{-4} to 8.5×10^{-4} in./in. sec $^{-1}$, where both slippage and brittle cleavage

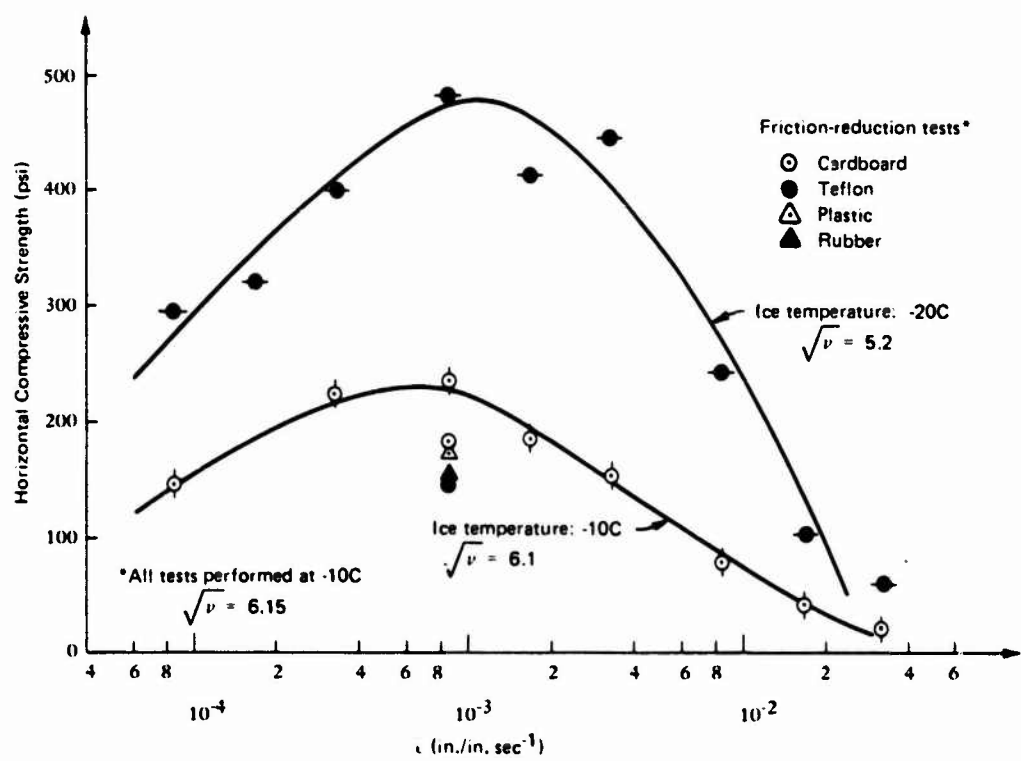


Figure 14. Horizontal compressive strength versus strain rate.

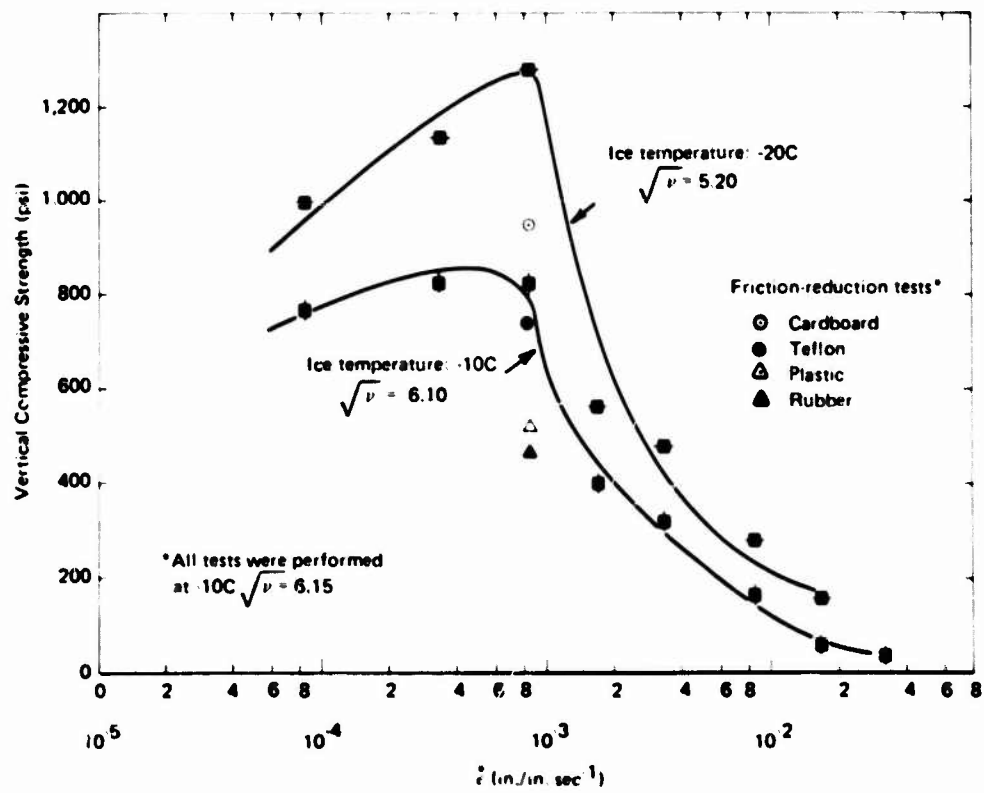


Figure 15. Vertical compressive strength versus strain rate.



Figure 16. Horizontal compressive ice specimen tested at -20C and loaded at a rate of 1 in./min (1.7×10^{-3} in./in. sec $^{-1}$).



Figure 17. Horizontal compressive ice specimen tested at -20C and loaded at a rate of 5 in./min (8.5×10^{-3} in./in. sec $^{-1}$).

cracks may occur together. Generally, microcracks are initiated at grain boundaries and are followed closely by abrupt cleavage cracking. But even after cleavage cracks form, the specimen is able to sustain additional loading and usually attains its maximum load without explosive rupture.

Friction-Reduction Tests. Secondary tensile stresses, which normally would

cause failure at lower compressive strengths, are suppressed due to friction building up between the ice specimen and the loading heads. To reduce this friction, some type of material is generally placed between the specimen and platens to permit lateral movement. Four different materials - cardboard (0.023-in. thick), rubber (0.068-in.), Teflon (0.033-in.), and polyethylene plastic (0.007-in.) - were evaluated as

friction-reducers in a series of tests on saline-ice specimens at -10°C. A constant strain rate of 8.5×10^{-4} in./in. sec⁻¹ was maintained throughout the tests. The results are also shown in Figures 14 and 15. While these tests produced the expected result of lowering the compressive strength, shear planes were still the dominating failure mechanism of horizontal ice specimens with vertical cleavage cracking notably absent. However, lateral bulging of most horizontal specimens was reduced, and this would probably have a small effect on longitudinal deflection measured by an extensometer attached to the surface of the ice sample. It was observed that the thicker rubber caused plastic flow in several ice specimens even at this moderate strain rate, while cardboard absorbed moisture and had to be replaced often. It is recommended that a thin sheet of some friction-reducing material (such as plastic or Teflon) be used during compression testing of sea ice; however, previously mentioned compressive strength tests without friction-reducers are still valid, since they provide an upper limit for design considerations of ice action on a structure.

Flexural Strength

Both laboratory and field tests were performed to determine the flexural strength and apparent elastic modulus of sea-ice beams (1, 3, 4, 12). Laboratory specimens were all 2 x 2 x 16-in. span beams, tested under a symmetrical two-point load, spaced 6 in. apart. The test setup is shown in Figure 18. All beams were sawed from the ice block with their longitudinal axis parallel to the ice surface (horizontal beams), and tested in an orientation that placed the normal vertical ice crystal growth in the same plane as the applied load. Once roughly cut from the ice block, these beams were

finished on a planer to a nominal 2 x 2-in. cross section. However, analysis was based on calculating the section modulus of each beam from its actual cross-sectional dimensions. Five test temperatures (-4, -7, -10, -20, and -27°C) and one salinity level (7 to 9 ppt) were the independent variables for all laboratory flexural strength tests. A strain-gage-type extensometer with a 4.5-in. gage length attached to the underside of the beam provided continuous strain output. The gage was positioned symmetrically with the beam centerline to account for only strain within the constant moment section of the beam.

Flexural strength data on annual sea ice at McMurdo, Antarctica, and Barrow, Alaska, come from testing large in-situ beams approximately 40 in. wide by 66 to 96 in. deep and ranging from 50 to 100 ft in length. The apparatus for cutting and testing large in-situ beams is shown in Figures 19 and 20. The ice saw (Figure 19) is capable of cutting ice up to 10 ft thick, and the load frame (Figure 20) can apply loads up to 200,000 lb, which is measured with a strain gage load cell. To avoid the necessity of including shear deformation in the analysis, all of the large field beams maintained a length-to-depth ratio between 8 and 10. These beams were tested under three boundary conditions (cantilever, fixed-fixed, and simply supported) with an LVDT having a 6-in. stroke that continually monitored deflections. Except for a few beams tested at -2.5°C (essentially isothermal), the remainder of the large field beam tests were conducted with a thermal gradient across the beam. Ice-sheet temperature as well as salinity profiles were continuously logged during the tests. The general salinity data range for all field tests was 5 to 7 ppt.

In addition to the large in-situ beams, several medium-sized beams with a cross section from 30 to 60 sq in. were

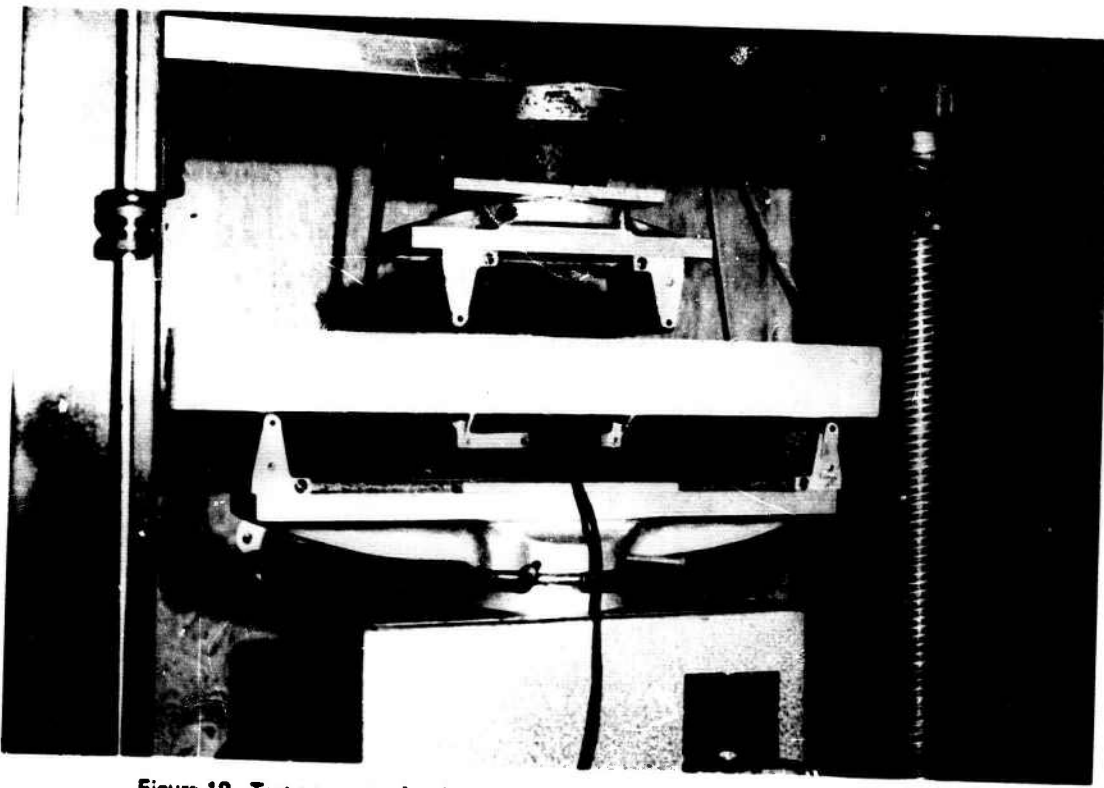


Figure 18. Test apparatus for determining flexural strength and apparent elastic modulus of 2 x 2 x 16-in. span beam.

extracted from the ice sheet and center-point loaded as simply supported beams. Several groups of small 2 x 2 x 16-in. beams were also cut from ice sheet blocks and tested identically to laboratory experiments. The typical stress rate for applying the failure flexural load in the field was greater than 14 psi/sec, while typical stress rates for laboratory beam tests ranged from 25 psi/sec for warm (-4C) sea ice to 50 psi/sec for cold (-27C) sea ice.

The flexural strength from both laboratory and field tests is shown in Figure 21 as a function of the square root of the brine volume present in the ice. The same analytical technique used to relate tensile and compressive strength to the combined effect of salinity and temperature was employed.

The data were plotted using the individual field data points and the mean value for each laboratory sample group. A weighting factor was applied to give more significance to the field tests by assuming 25 laboratory specimens equaled one large-scale field test. The equation of the straight line based on least-square analysis is:

$$\sigma_f = 139.1 - 8.82 \sqrt{v} \quad (5)$$

where v is the brine volume in ppt and σ_f is the flexural strength in lb/sq in. Again, each isothermal laboratory data group is shown with a 95% confidence level about its mean. If one extrapolates the best fit line, it is found that Equation 5 predicts a flexural strength (modulus of

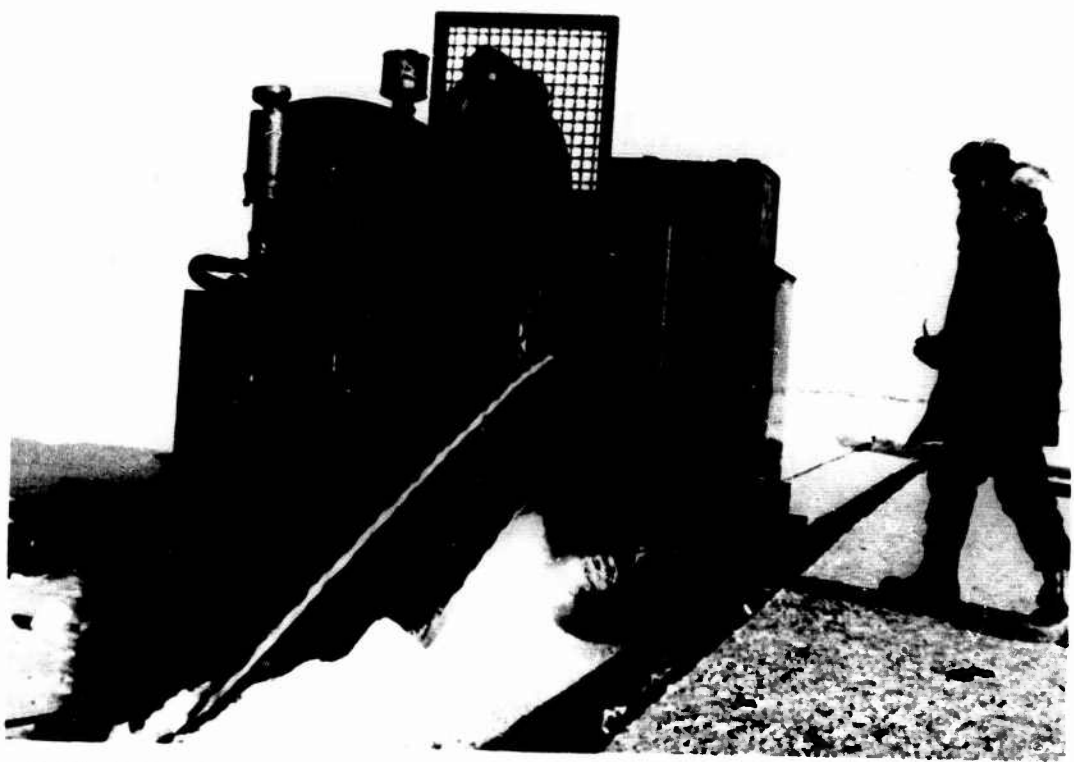


Figure 19. Gasoline-hydraulic chain saw with 12-ft blade used for cutting large in-situ sea-ice beams.

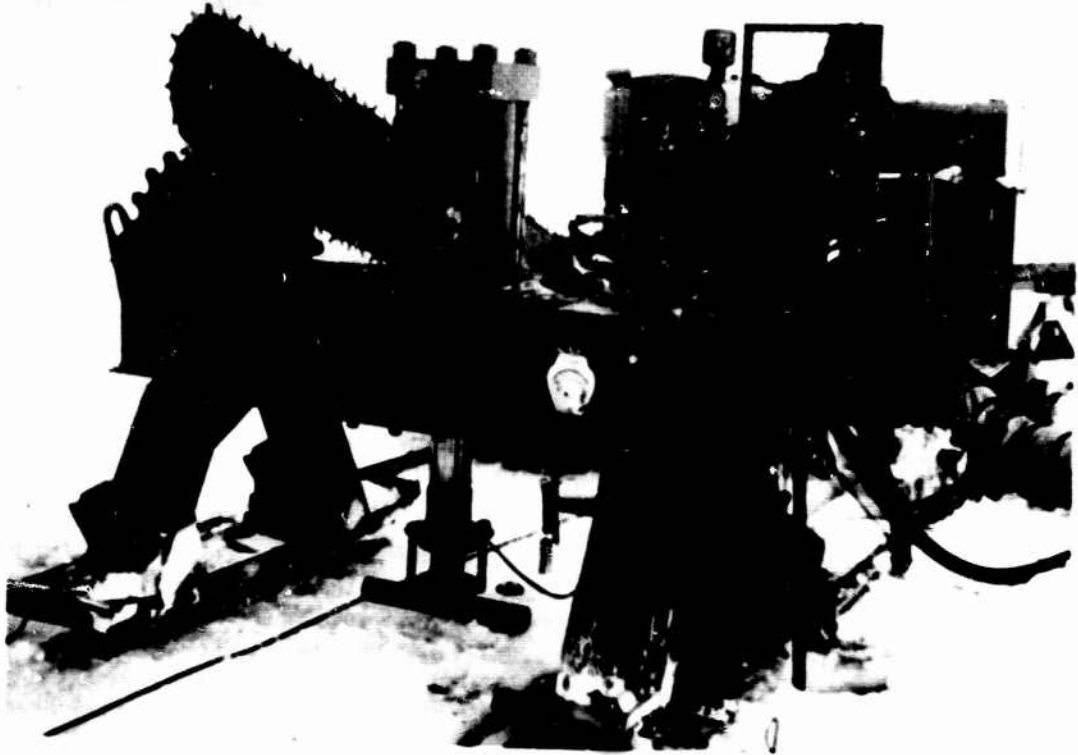


Figure 20. Hydraulic test frame with 200,000-lb capacity for loading large in-situ sea-ice beams.

rupture) of about 140 psi for ice of zero brine content but the same microstructure as sea ice.

Figure 22 shows the effect of temperature-salinity on both flexural and horizontal tensile strength as a function of the square root of brine volume. It is significant that the analysis for each case resulted in first order equations that have nearly the same line slope, that is, -8.82 and -9.99. Of course, this is as it should be since the portion of the beam below the neutral axis is under tension and represents a tension failure. The indicated ultimate tensile strength of the ice based on beam flexural formula is approximately 20 psi greater than the observed uniaxial tensile strength (horizontal). This disparity is a common characteristic of brittle materials that do not have the same tension and compression properties. The neutral axis in the beam specimen must shift towards the stiffer side of the beam (compression side for ice) in order to maintain equality of the resultants of the tension and compression forces. Thus, the fiber stress computed by the flexural formula is less than the true fiber stress on the stiffer side of the beam and is greater than the actual fiber stress on the other side.

Elastic Modulus

In addition to strength properties, the single most important material property of sea ice is its elastic (Young's) modulus, which is necessary for analyzing ice plate behavior. Consequently, strain values obtained during the beam tests were used to determine the apparent modulus of elasticity for sea ice as a function of brine volume. All laboratory strain data were measured with extensometers bonded to the underside of 2 x 2 x 16-in. simply supported beams subjected to two-point loadings. In

addition to the laboratory experiments, the large-scale field beam tests measured deflections with a 6-in. stroke LVDT. These results are displayed in Figure 23, and a straight-line approximation using least squares is calculated for all flexural tests.

$$E_f = [771 - 63.2 \sqrt{v}] \times 10^3 \quad (6)$$

where E_f is the apparent flexural modulus of elasticity in lb/sq in. and v is the brine volume in ppt.

Another method for finding the modulus of elasticity is to measure the strain corresponding to a given stress state in a right-circular cylinder subjected to either uniaxial compression or tension. During compressive strength testing, deflection measurements were recorded with extensometers having a gage length of 2.4 in. that were attached directly to each specimen by bonding with freshwater ice. However, elastic modulus values found by compression testing are strain-rate sensitive. The results of three different compressive strain-rate tests performed at one brine volume value on horizontal sea-ice specimens are shown in Figure 23. The moduli averages for a limited statistical sample for both 1.7×10^{-3} and 3.4×10^{-3} in./in. sec $^{-1}$ strain rates are shown as triangles on Figure 23. Since these values bracket the flexural data, these two strain rates are deserving of a more complete evaluation. Another possible contribution to greater compressive deformation measurement in horizontal specimens that cause unrealistically low elastic moduli values is end constraints. No investigations were made of end-constraint effects on the elastic modulus of sea ice. In addition to further strain-rate and end-constraint testing, better strain and deflection measurement techniques, especially at warm temperatures, are required to properly assess the deformation behavior of sea ice.

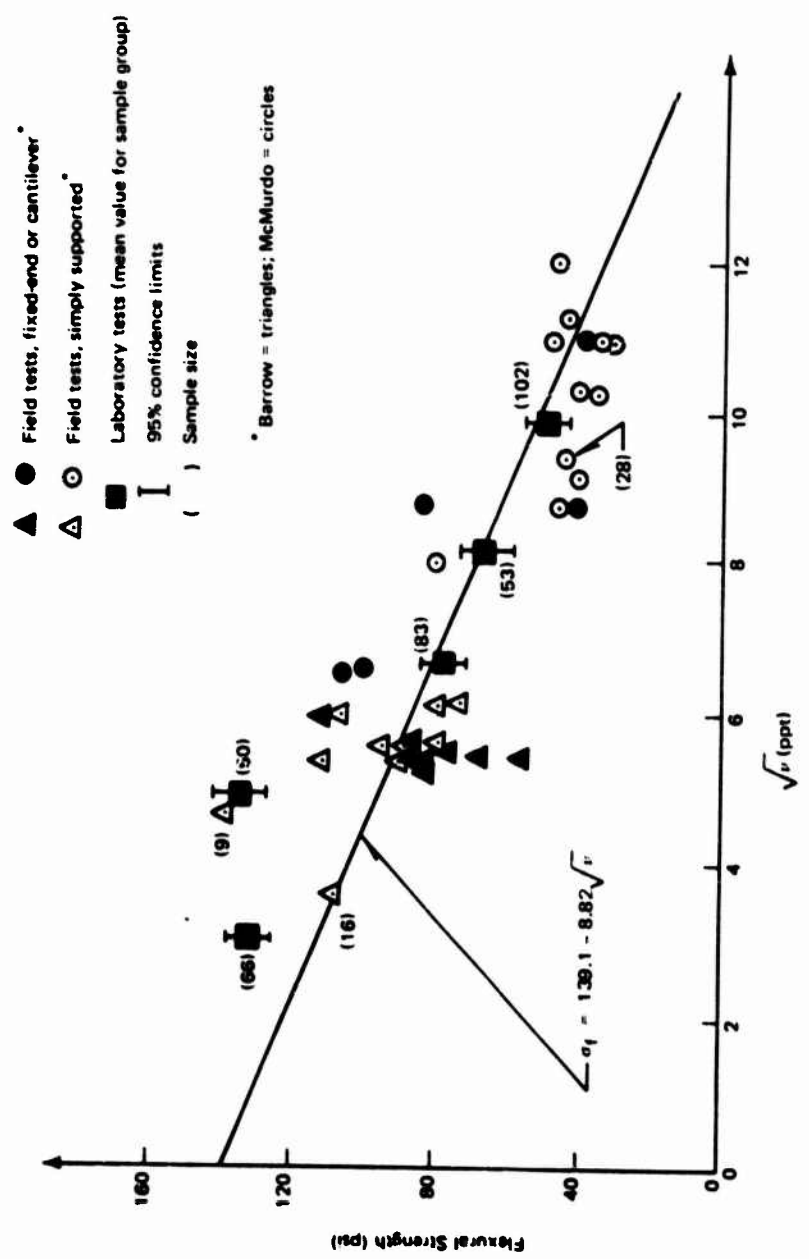


Figure 21. Flexural strength versus brine volume.

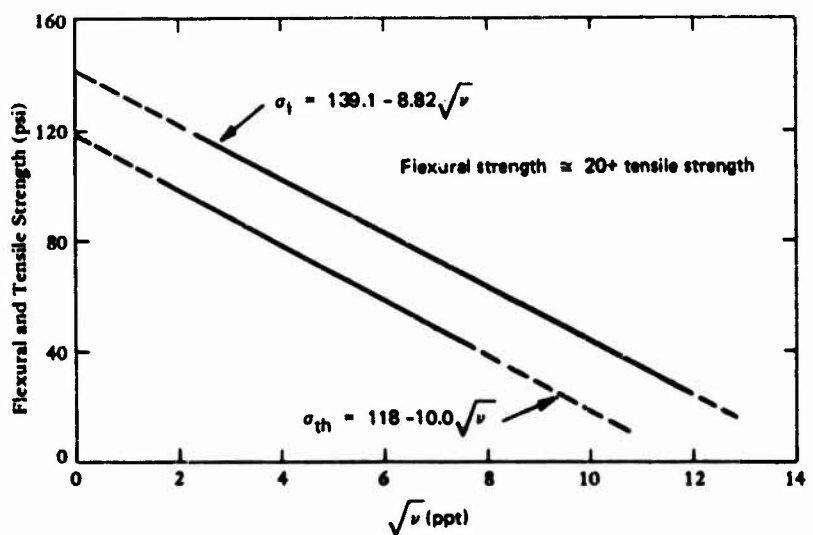


Figure 22. Flexural strength (rupture modulus) and horizontal tensile strength versus brine volume.

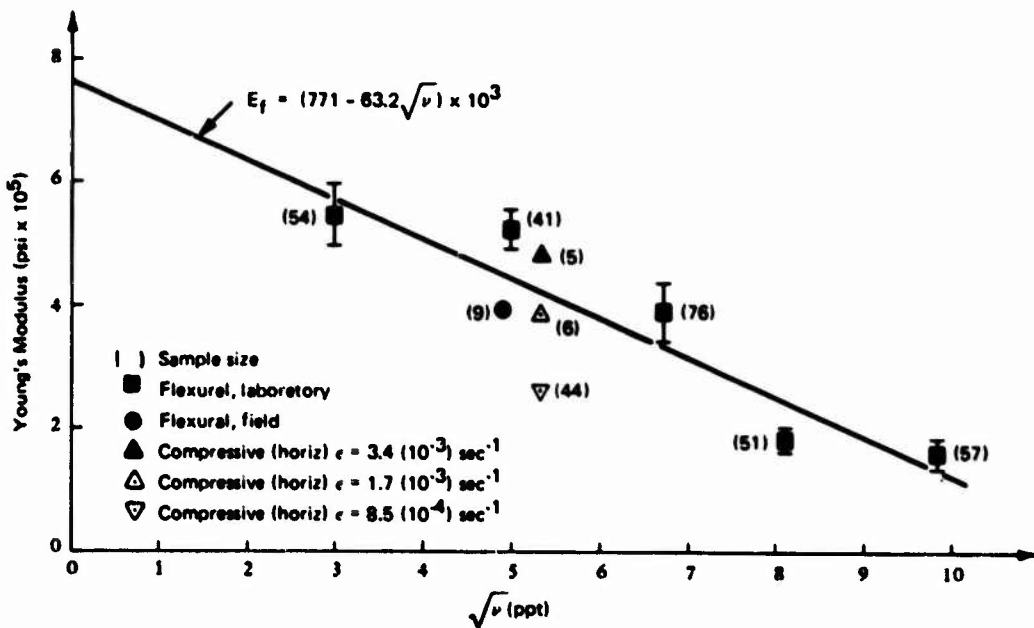


Figure 23. Young's modulus of sea ice versus brine volume.

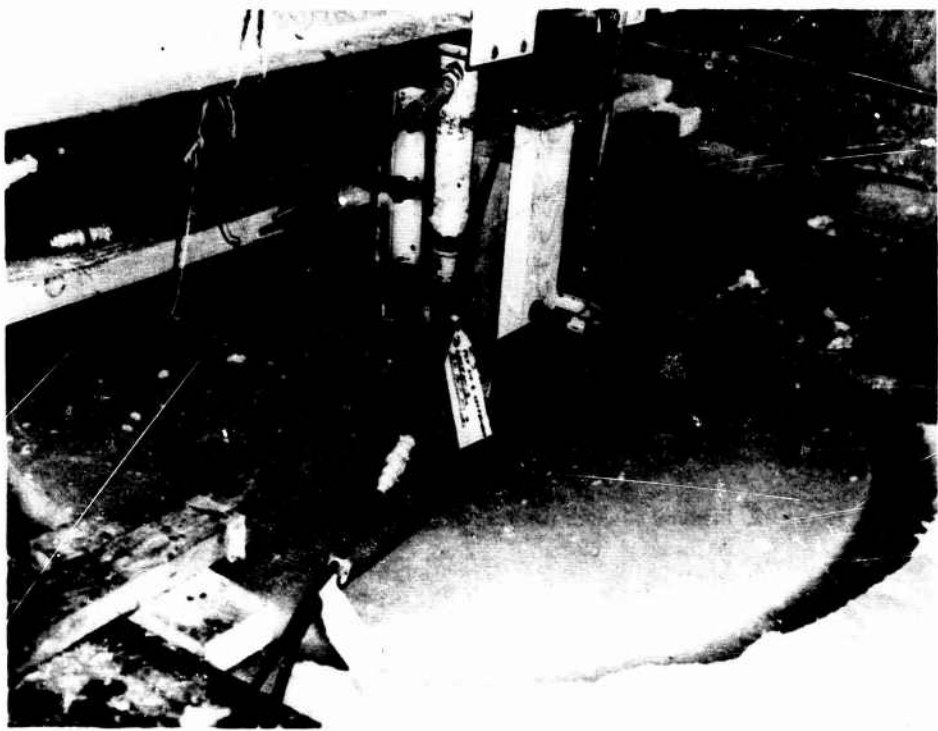


Figure 24. Laboratory setup for plate experiments.

Several sea-ice plate experiments were performed in the laboratory to investigate the behavior of a CEL-developed sea-ice strain transducer (14) and to determine the modulus of elasticity by monitoring strains and deflections of sea-ice plates under load. Simply supported sea-ice plates (9 ppt salinity), 4.5 in. thick and 42 in. in diameter, were subjected to a circular ring loading applied by a hydraulic ram. The laboratory setup is shown in Figure 24, while Figure 25 illustrates the geometry, ring loading, and location of embedded strain gages common to all plate tests. The gages were grouped in two pairs so that each pair measured strain in two orthogonal directions to cancel any anomalies arising from asymmetry. Gages 1 and 4 were made of two active arms that were temperature-compensated and encased in a pliant

material called Gagekote 5, while gages 2 and 3 were identical except that they were encased in Plexiglas. All four gages had an active length of 5.5 in. and a gage factor of 2.0. Their development and testing are discussed in greater detail in Reference 14.

In order to induce elastic behavior, loading was applied at stress rates ranging from 7.5 to 15 psi/sec until a preselected peak load was reached; then the load was released. The strains were continuously recorded, and peak strains were easily distinguished. This pattern was repeated for different peak loads. Some scatter of peak load versus peak strain was noted for all gages during different tests. However, the top gages in the compression zone exhibited a linear relationship with the load, whereas the tension gages suggested a nonlinear response, perhaps due to tension cracking

of the sea ice. In addition to the embedded strain gages, deflections were monitored by a single centerline LVDT with a 6-in. stroke plus two extensometers with gage lengths of 2.5 in. bonded to both the top and bottom of the sea-ice plates.

Plate tests were performed at four constant temperatures: -4, -10, -20, and -30C. The elastic modulus values for each test temperature, which were calculated from plate theory equations, are shown in Figure 26. The averaged values from gages 1 and 4 provided the strain input, while the output from the LVDT and both extensometers were averaged to supply deflection data. The apparent elastic moduli found from the flexural tests are superimposed on this same figure for comparison. In a later section on analytical methods, output from the elastic finite-element computer code will be compared with the sea-ice plate strain data.

Fracture Toughness

In the analysis of ice sheet behavior under sudden or sustained loading, an allowable flexural stress has been traditionally considered as the design (or application) criterion. Normally, this allowable stress condition represents an arbitrary reduction in a known ultimate flexural strength, usually an average value of a set of laboratory and field experiments. Both fracture mechanisms and failure modes of sea ice are being studied in an attempt to define a suitable failure criterion for ice sheets. Once a failure criterion is determined, a factor of safety can be established with greater confidence.

One possible approach to the ice-sheet cracking problem is to treat it by Griffith theory as a brittle fracture (13). First, the point is defined at which an existing crack becomes unstable. Once

either the stress intensity factor, K, or the strain energy release rate, γ , are known, the stress field at the crack tip becomes completely defined. The factor K increases with an increase in applied load, but a small area of plastic deformation ahead of any growing crack can partially offset the intensification of the local stress field caused by the applied load, P, and crack length, c. However, K increases faster than the plastic strain area, and its value rises rapidly during this initial period of slow crack growth. At some combination of P and c, represented by a critical value of K, the stress intensity at the crack edge becomes so large that the crack can propagate without supplying additional energy. At this time P reaches a maximum, the crack becomes unstable and propagates rapidly instead of slowly. The critical value of K is called the fracture toughness, K_{Ic} , of the material and is related to γ_c , the critical strain energy by

$$K_{Ic}^2 = \frac{\gamma_c E}{1 - \mu^2} \quad (7)$$

where E is Young's modulus and μ is Poisson's ratio. According to Griffith, cracks will propagate rapidly and produce a brittle fracture (the area of plastic strain is very small) when the applied stress reaches a failure value of

$$\sigma' = \left[\frac{2\gamma_c E}{\pi c(1 - \mu^2)} \right]^{1/2} \quad (8a)$$

or rewritten using Equation 7

$$\sigma' = \sqrt{\frac{2}{\pi c}} K_{Ic} \quad (8b)$$

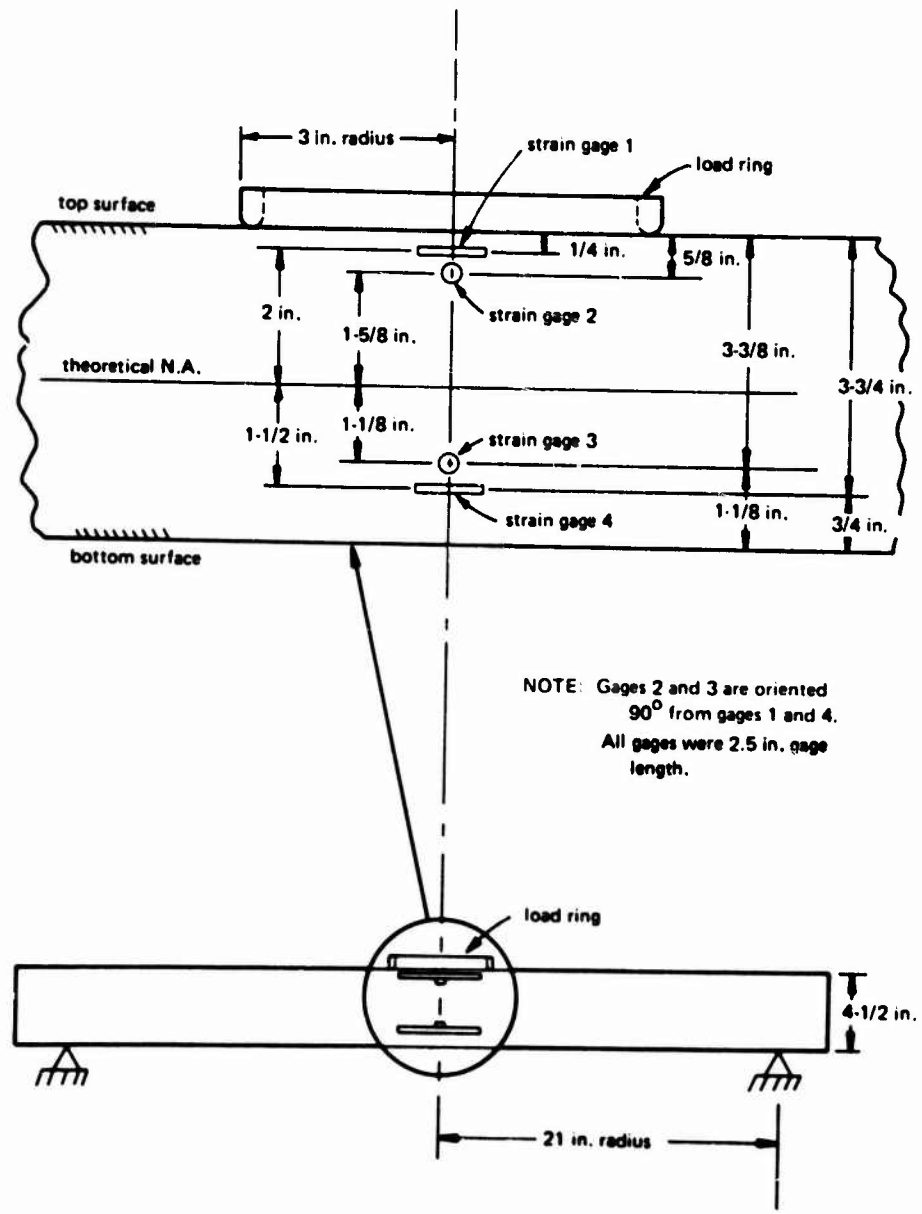


Figure 25. Experimental sea-ice plate.

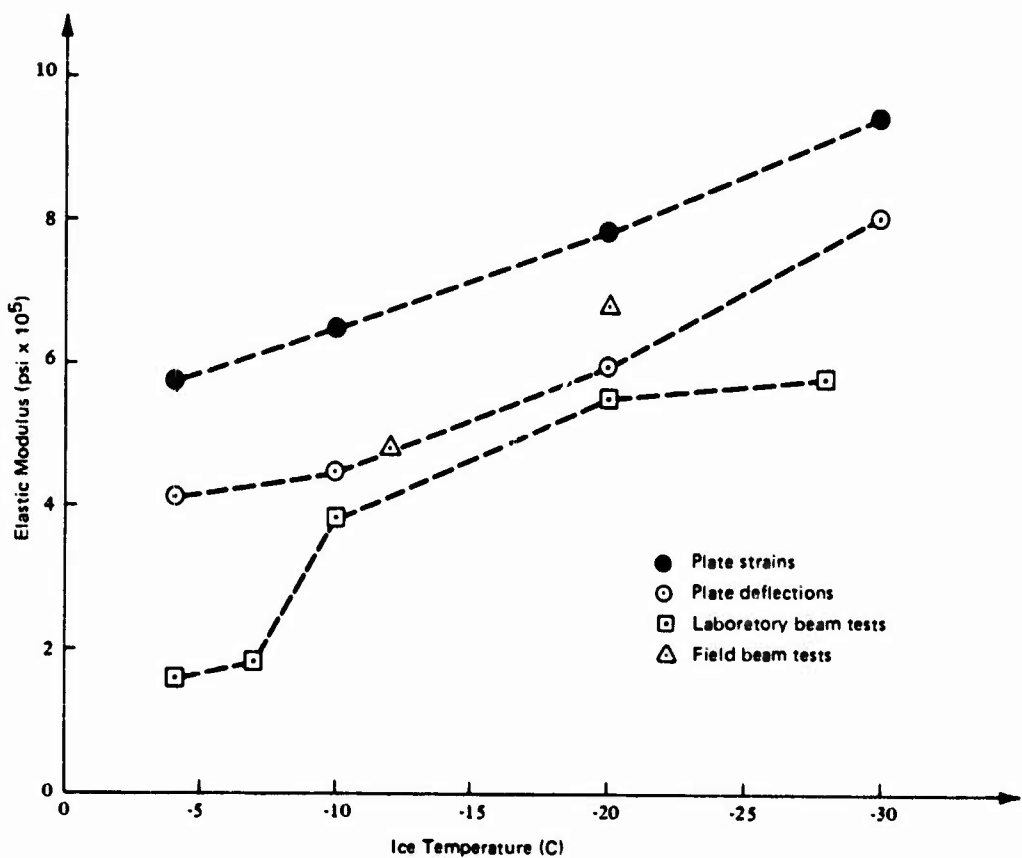


Figure 26. Sea ice elastic modulus versus ice temperature.

where c is the critical crack length.

While γ_c is difficult to evaluate, K_{Ic} , the fracture toughness property, is easier to find by experimentation. To determine K_{Ic} for sea ice as a function of brine volume, laboratory tests were performed on 2 x 2 x 16-in. beams with central saw-cut notches 0.5 in. deep. A two-point loading with a 6-in. spacing was applied at a loadhead speed of 0.2 in./min. Approximately 25 notched sea-ice beams were tested at each of two test temperatures: -20 and -10°C. All of the beams failed instantly with a crack initiating at the root of the notch and rapidly propagating through to the top

surface. A binomial expression can be written to calculate the fracture toughness as a function of the notch-to-beam-depth ratio (15).

$$K_{Ic} = \frac{3Pb^{1/2}(l_1 - l_2)}{2wd^2}\beta \quad (9)$$

where P is the applied load, b is the notch depth, l_1 is the beam support spacing, l_2 is the two-point load spacing, w is the beam width, d is the beam depth, and

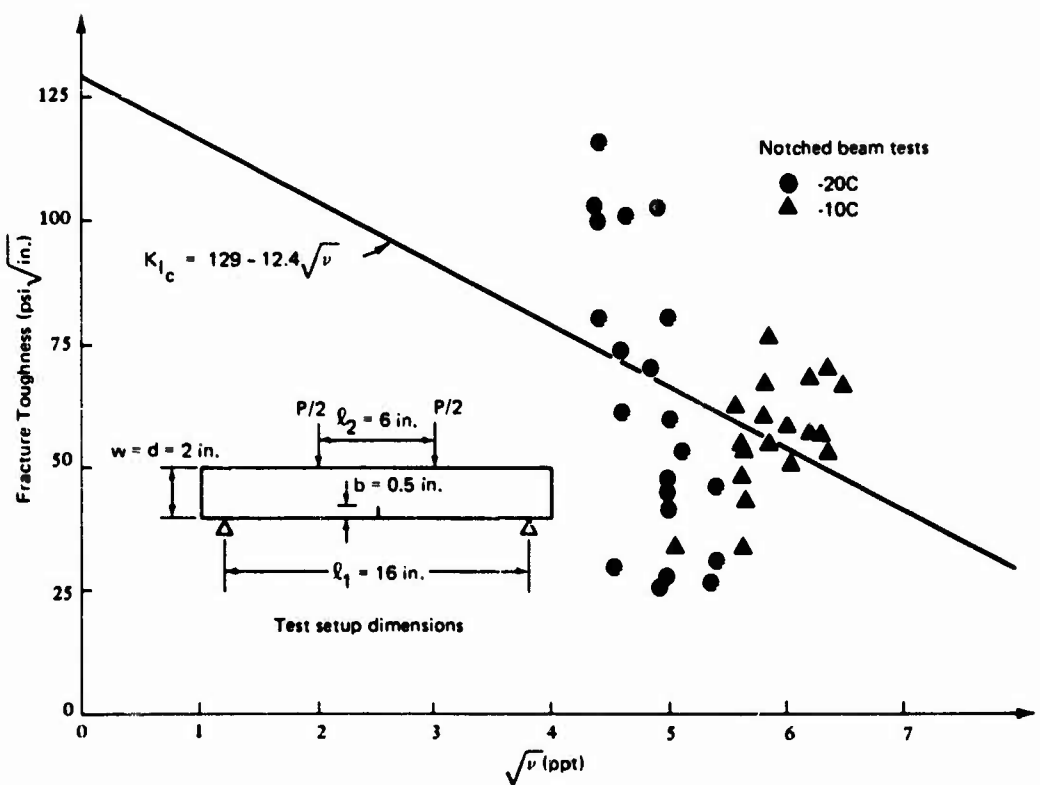


Figure 27. Fracture toughness versus brine volume.

$$\begin{aligned}
 \beta &= 1.99 - 2.47(b/d) + 12.97(b/d)^2 \\
 &\quad - 23.17(b/d)^3 + 24.80(b/d)^4 \\
 &= 1.918 \text{ (for } b/d = 0.25) \quad (10)
 \end{aligned}$$

Using the geometric constants from the insert of Figure 27 and Equation 10, Equation 9 can be rewritten as

$$K_{I_c} = 2.543 P \quad (11)$$

The fracture toughness results from the laboratory experimentation are shown in Figure 27 as a function of brine volume, v . The straight-line approximation is calculated by the linear regression

technique of least squares and represents a tentative relationship between K_{I_c} and v .

$$K_{I_c} = 129 - 12.4 \sqrt{v} \quad (12)$$

where K_{I_c} is the material property fracture toughness expressed in $\text{psi} \sqrt{\text{in.}}$ and v is the brine volume in ppt. Using Figure 26 to obtain a range for the modulus of elasticity and letting $\mu = 0.3$, one can calculate the critical energy γ_c which causes a crack to propagate without any additional energy required, from Equation 7. For sea ice, $\gamma_c \approx 1 \times 10^{-2}$ in.-lb/sq in. The size of a critical crack can be found by rewriting Equation 8b as

$$c = \frac{2 K_I C^2}{\pi \sigma' ^2} \quad (13)$$

If nominal values of 65 psi $\sqrt{\text{in.}}$ and 100 psi are chosen for $K_I C$ and σ' , respectively, then the critical crack length would be approximately 0.25 in. Of course, sea ice contains brine inclusions that are around 0.05 in. in diameter, considerably smaller than the 0.25 in. There is no doubt that these brine pockets serve as stress concentration points and provide a source for crack initiation. However, it does seem probable that some dislocation movement due to localized plastic strain could occur that would cause slow crack propagation until the critical crack length is reached by linking several brine pockets with small subcritical cracks.

It is not sufficient to attempt to formulate a failure criterion for sea-ice sheets solely on the basis of fracture mechanics theory and small notched-beam tests in the laboratory. As in other material properties experiments, however, it is necessary to investigate and understand microscopic behavior before it is applied to the macroscopic scale of a floating ice sheet.

Creep Behavior

It is well known that the assumption of elastic behavior for sea ice is valid only for a narrow range of load magnitude and length of application. Many previous studies have considered viscoelastic ice behavior (16, 17, 18). At CEL two laboratory investigations have been made on sea-ice creep response: one on simply supported beams (3), and one on uniaxial compressive and tensile specimens (19). In addition, field experimentation on long-term sea-ice behavior

of in-situ cantilever beams has been performed as a large-scale verification of laboratory efforts.

Uniaxial Laboratory Tests. An extensive laboratory experimental program has been performed to define uniaxial deformation time history of sea ice. Both uniaxial compressive and tensile creep tests were conducted on cylindrical specimens having a length-to-depth ratio of 2:1 that were cored either horizontally or vertically from sea-ice blocks. A constant load was applied to each specimen through a deadweight lever arm system (commonly used in soil compaction testing). This applied constant load was predetermined as a percentage of the average elastic compressive or tensile strength for a given ice temperature and crystal orientation. Three different percentages (10, 25, 50%) were considered as load level parameters. Several tests at each parametric combination of loading conditions, crystal orientation, and load levels were conducted as a series for each of four ice temperatures (-4, -10, -20, -27°C). Consequently, a total of 48 different parametric combinations had to be considered.

Ice growth has been controlled to maintain a constant salinity range, density, and crystal size representative of natural sea ice. Still, for time-dependent tests this became an awesome task requiring multiple-specimen testing over a single time interval. Two test frame setups (Figures 28 and 29) were devised to accommodate four compression and two tension tests at the same time. Both frames are deadweight systems with the compression loading in Figure 28 applied through a 40:1 lever arm. Figure 29 shows a 10:1 lever-arm compression loading frame. Still, over 300 specimens had to be tested to assure proper statistical sampling.

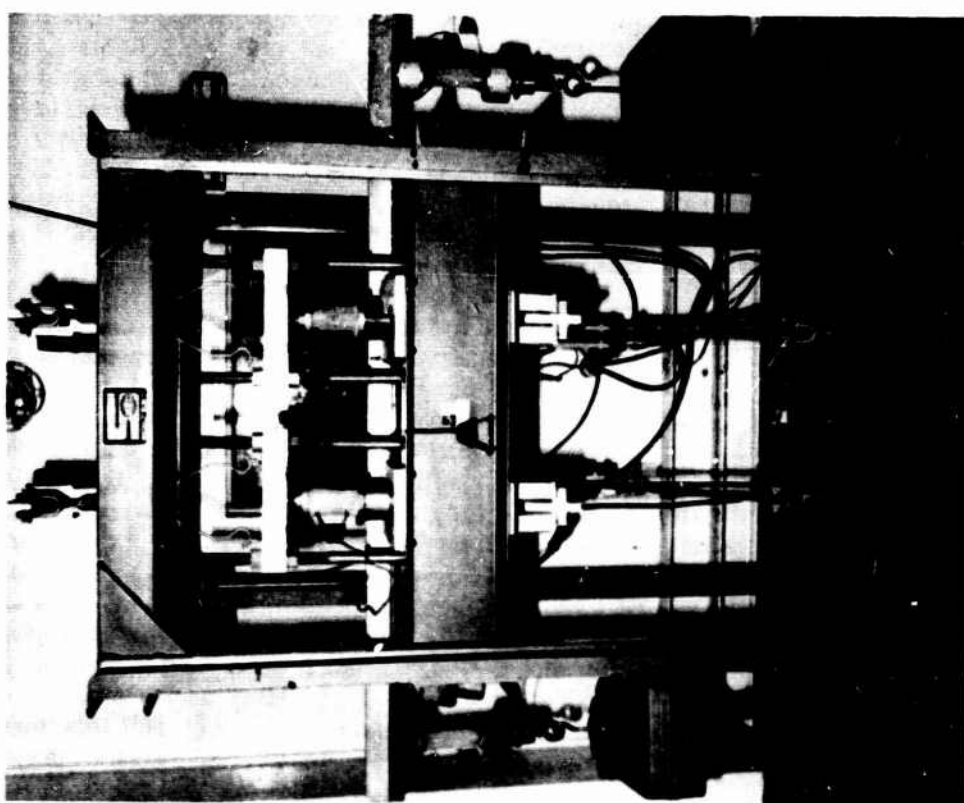


Figure 28. Deadweight test frame
for loading two compression
and two tension ice specimens.

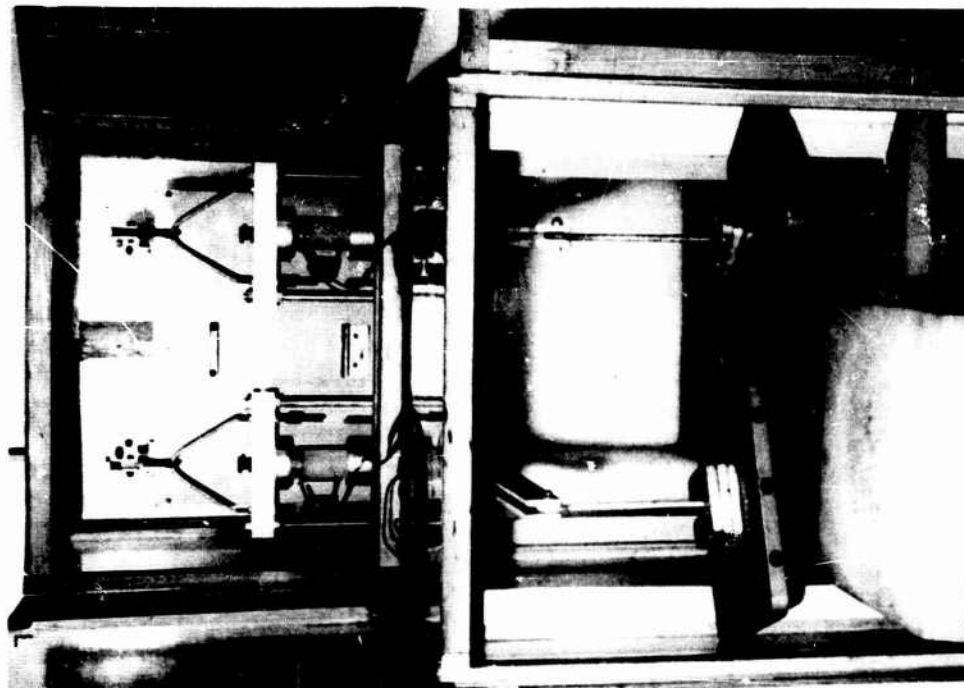


Figure 29. Deadweight test frame
for loading two compression
ice specimens.

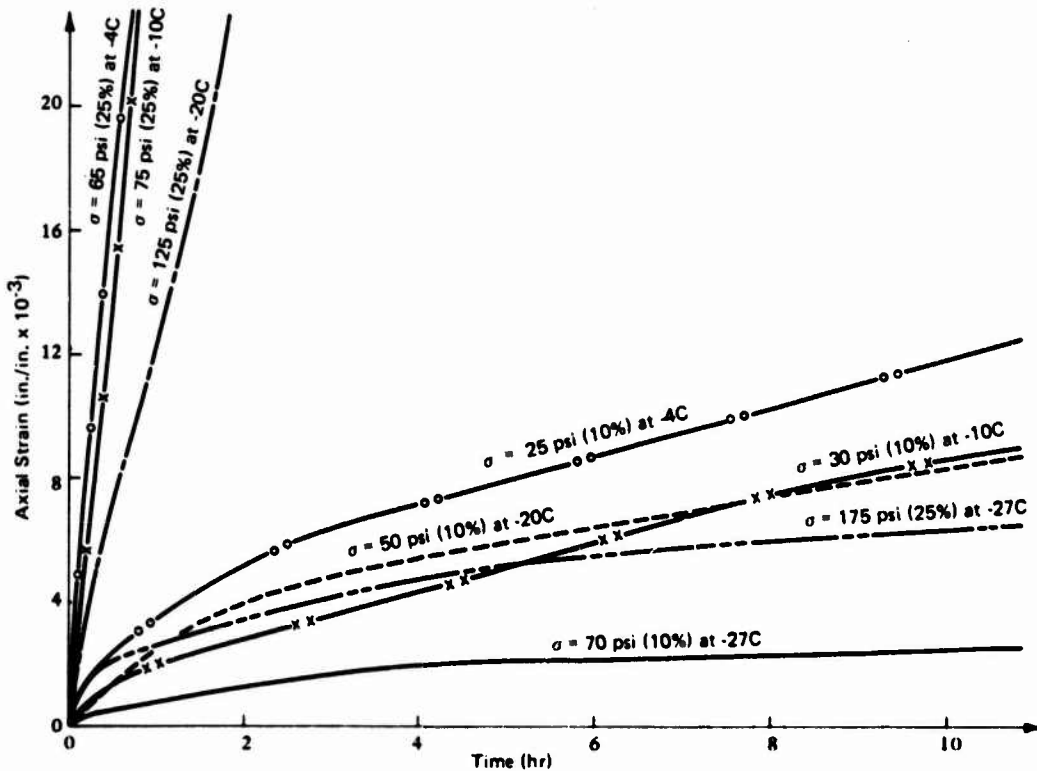


Figure 30. Viscoelastic behavior of sea-ice specimens with compression loading and horizontal (perpendicular) crystal.

The output for each individual test is the strain history, shown in Figures 30 through 33, but each curve represents an average for a sample size ranging from 3 to 6 specimens. The deflection is measured by extensometers with a gage length of 2.4 in., attached directly to the ice specimens. Each figure displays different temperature and stress level curves for a specified loading condition and crystal orientation.

Theoretically, each figure should display 12 curves, but higher stress levels fail ice specimens very quickly. Therefore, those fast-acting and virtually nonexistent strain histories have been deleted. In Figures 30 and 31 compressive strain histories are shown for only

10 and 25% stress levels, since the 50% stress level produced failure within 5-10 min. On the other hand, the tensile strain histories in Figures 32 and 33 are shown for those stress levels that produced good creep data. First, a 10% stress level produced little creep response in tension specimens over the 30-hr test period, so several attempts were made to substitute a 75% stress-level loading. However, most 75% stress-level loadings produced instantaneous failure. Several 50% stress-level curves are also missing due to instantaneous failure, while absent 25% curves, especially at lower temperatures, represent no observable response over the testing time period. It is intended to fill out data-deficient

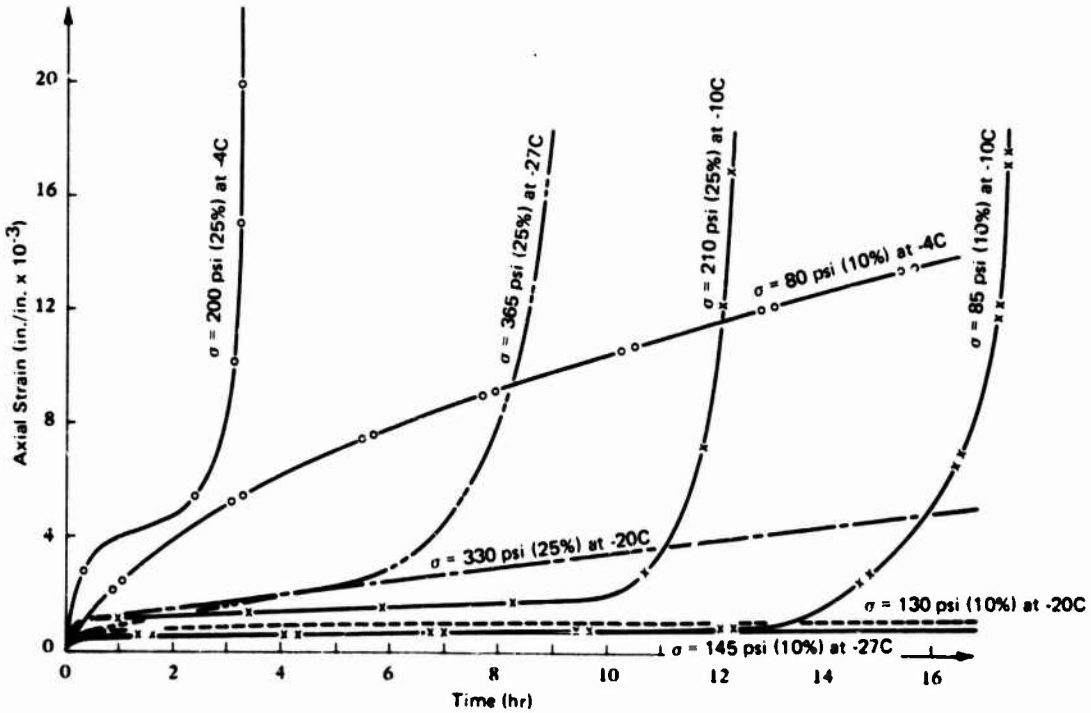


Figure 31. Viscoelastic behavior of sea-ice specimens with compression loading and vertical (parallel) crystal.

tension tests if required to adequately predict time-dependent ice-sheet performance.

While conducting uniaxial compression tests on sea ice, one can observe the failure planes develop as a function of time. Generally, specimens loaded parallel to their preferred crystal orientation failed along vertical cleavage planes, but macroscopic fracture occurred only at 25 and 50% stress levels, while the 10% stress level produced only microscopic cracking. The horizontal specimens, loaded perpendicular to ice crystal growth, universally failed along developed shear planes independent of ice temperature and

stress level. However, different combinations of these two parameters did have a significant effect on the rapidity of failure.

Laboratory Beam Tests. Observations were concerned with both creep deflection and strain measurements of 2 x 2 x 18-in. sea-ice beams with a two-point load applied at the one-third point. However, only the strain measurements over a 2.4-in. gage length will be considered in this discussion. Strain-gage-type extensometers were used for continuous strain monitoring during testing.

To determine creep properties it

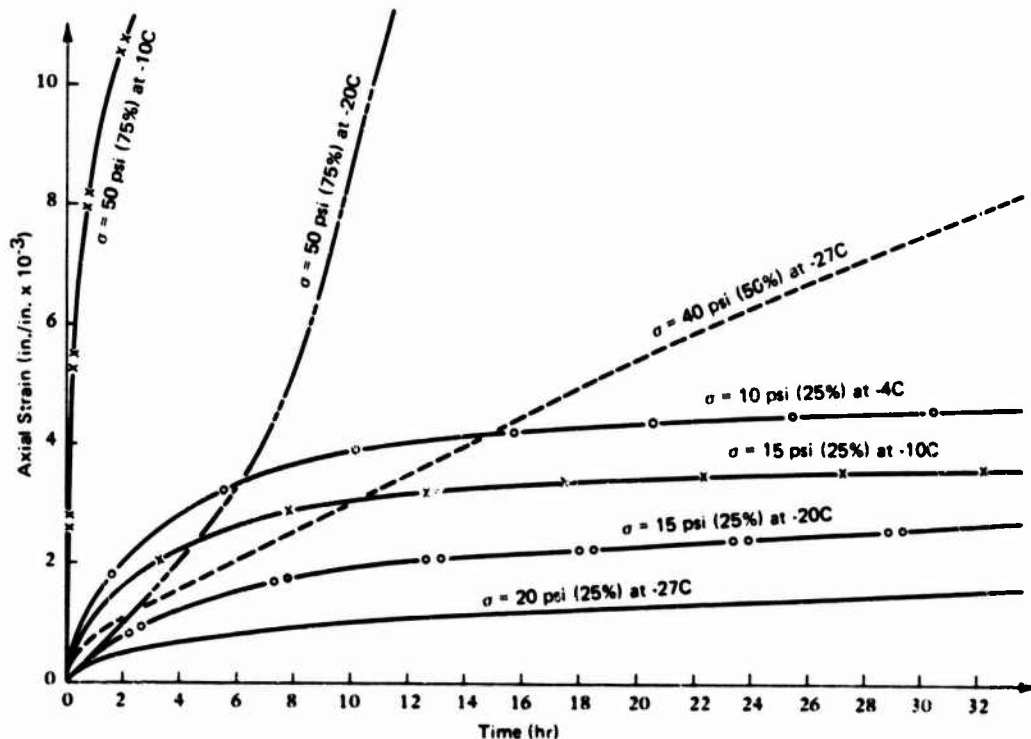


Figure 32. Viscoelastic behavior of sea-ice specimens with tension loading and horizontal (perpendicular) crystal.

was found necessary to enclose the test apparatus holding the beam in a plastic shroud (1) to shield the beam and the instrumentation from the effects of air movement within the test chamber and cyclic temperature variation ($\pm 2.2^\circ\text{C}$) of the chamber, and (2) to minimize sublimation of the specimen during the long term of the test. Continuous temperature monitoring within the plastic enclosure indicated fluctuation was reduced to a nominal $\pm 1/2^\circ\text{C}$. The test apparatus for the 18-in.-span beam was a small soil-test frame shown in Figure 34 which had been modified to accommodate a beam specimen. The end supports for the beam and the loading yoke, having multiaxis freedom of movement

for alignment, had rounded bearing surfaces to minimize the resistance of the specimen to rotation. Thin metal shims were inserted between the ice beam and load bearing points to prevent pressure penetration of the ice.

Creep strain histories are presented in Figure 35 for two stress and temperature parameters. Each curve represents an average of five individual beam tests. The salinity range was 7 to 9 ppt for all beam creep tests measuring strain.

Cracks in the tension face of the beam occurring particularly at crystal boundaries were frequently found during inspection of the specimen upon test completion. An effective method of detecting the surface and internal cracks

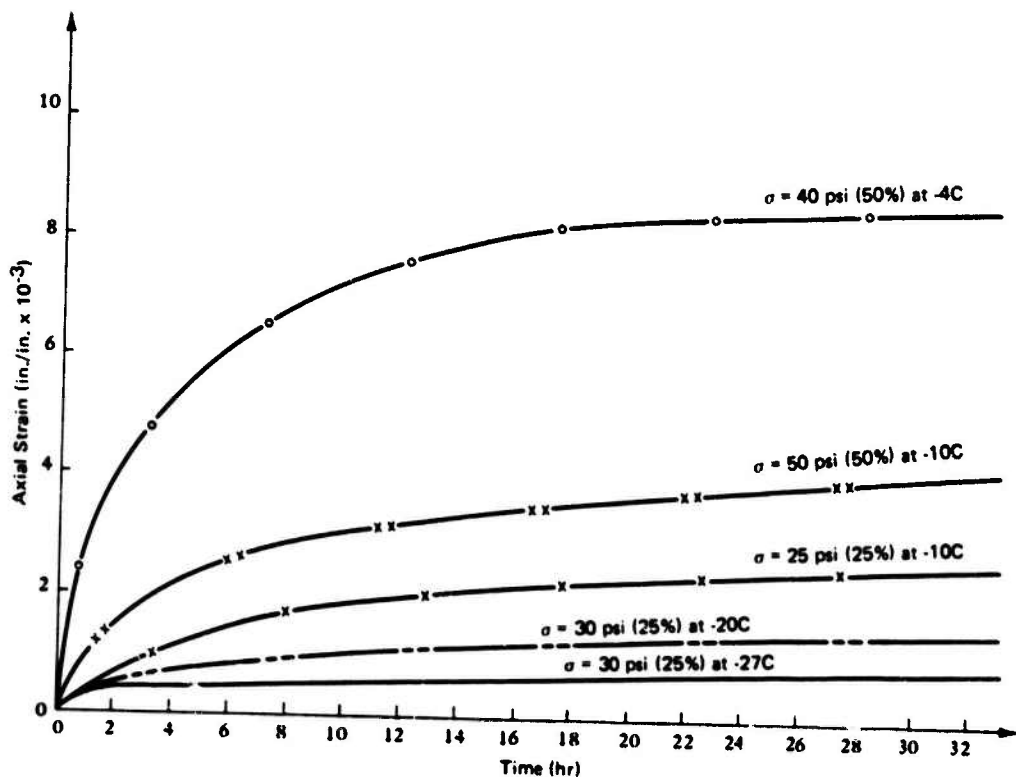


Figure 33. Viscoelastic behavior of sea-ice specimens with tension loading and vertical (parallel) crystal.

at the time of occurrence has yet to be developed; however, even with such a capability, analysis of the stress-strain state resulting from crack development would be difficult. A rarely observed creep phenomenon, that of deformation and slippage in the crystal lattices occurring at a triple crystal intersection, is shown in Figure 36.

Field Beam Tests. This large-scale experiment was designed to provide data points to help verify the extensive laboratory program defining the viscoelastic properties of sea ice. Tests were conducted on large in-situ cantilever ice beams cut from annual sea ice -

ungrounded, level, and generally crack-free. Beams had cut dimensions of approximately 3 ft in width and 45 ft long. The ice-sheet thickness was 75 in. during the testing period. A 30-hp, ladder-type trencher with specially designed conical teeth cut the beams, leaving 8-in.-wide open water trenches. However, it became necessary to employ heat-tape floating in the trenches to prevent freezeback.

A deadweight, 4:1 lever arm system provided an instantaneously applied, constant, downward load to the free end of the beams. The actual load applied to each beam was continuously recorded by a load cell, while beam deflection was

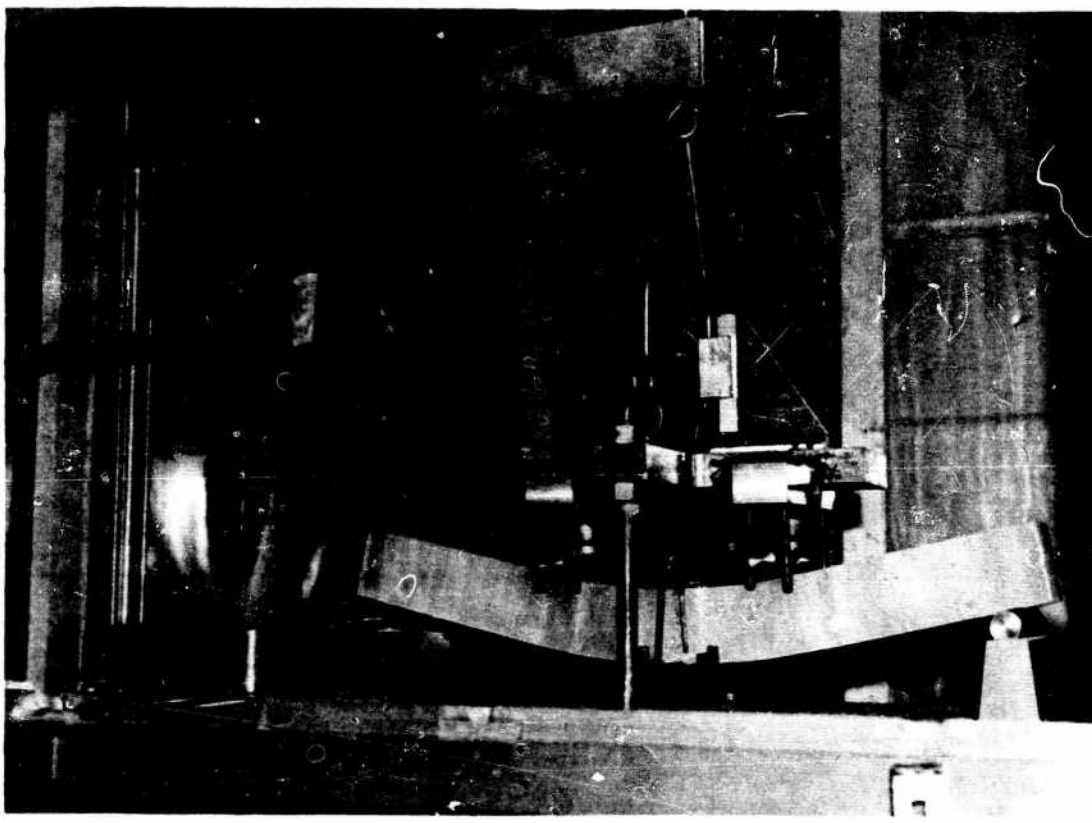


Figure 34. Small-beam creep test frame strain-gage-type extensometer measures strain over a 2-in. gage length.

monitored at the load application point by an LVDT (linearly varying displacement transducer). The entire setup is shown in Figure 37. The data are plotted in Figures 38 and 39. A salinity profile was recorded for each of the seven ice beams with salinities falling in a narrow range between 5.2 to 5.7 ppt. Ice surface temperatures ranged from -12 to -20°C during the test period. During each test a temperature profile of the ice sheet was periodically recorded.

Each test was run for a period of 45 to 70 hr, with step loads added at different times in an attempt to identify boundaries of viscoelastic-viscoplastic behavior as a function of stress-temperature levels. All the beams showed an elastic response after their initial step loads, and both beams 4 and 7

(Figure 38 and 39, respectively) were displaying elastic behavior after the second step loads at stress levels of 27.9 and 30.6 psi applied at times 45 and 65 hr into the tests, respectively. On the other hand, beams 2 and 6 (Figure 38) showed slightly plastic behavior under their third step loads occurring at 23 and 40 hr and at stress levels of 23.9 and 42.8 psi, respectively. This very limited information is not sufficient to adequately define elastic-plastic behavior boundaries. However, it appears that for sea ice at temperatures between -10 and -15°C inelastic behavior can occur at relatively low stress levels applied over a time period greater than 24 hr. A series of controlled laboratory tests should be performed to determine viscoelastic and plastic limits on sea-ice behavior.

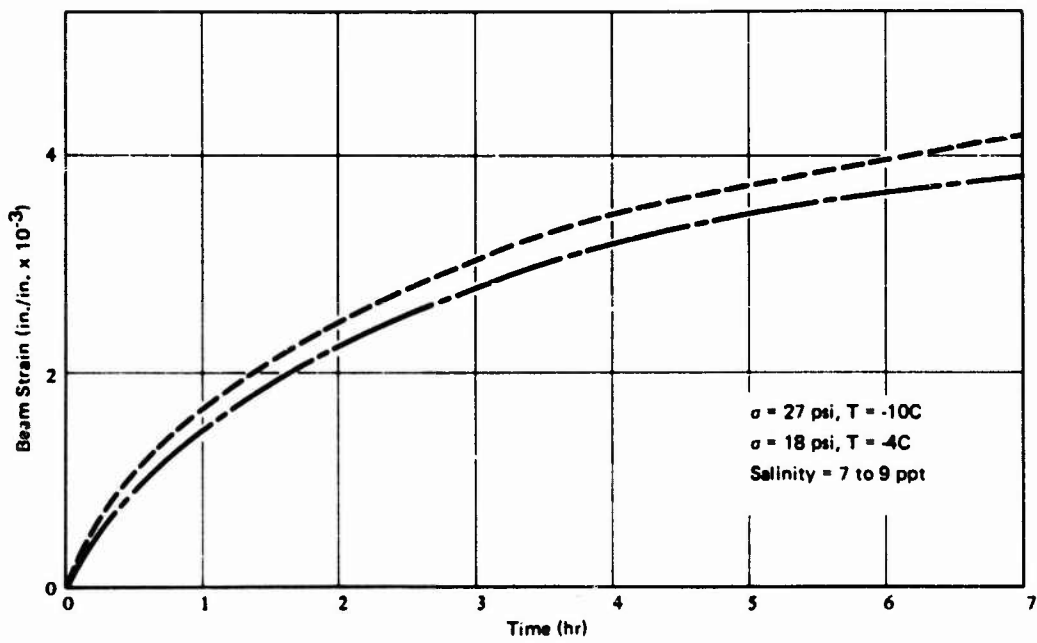


Figure 35. Creep strain versus time for 2 x 2 x 18-in. span beams loaded at third points.



Figure 36. Strain slippage at boundary intersection of three crystals.

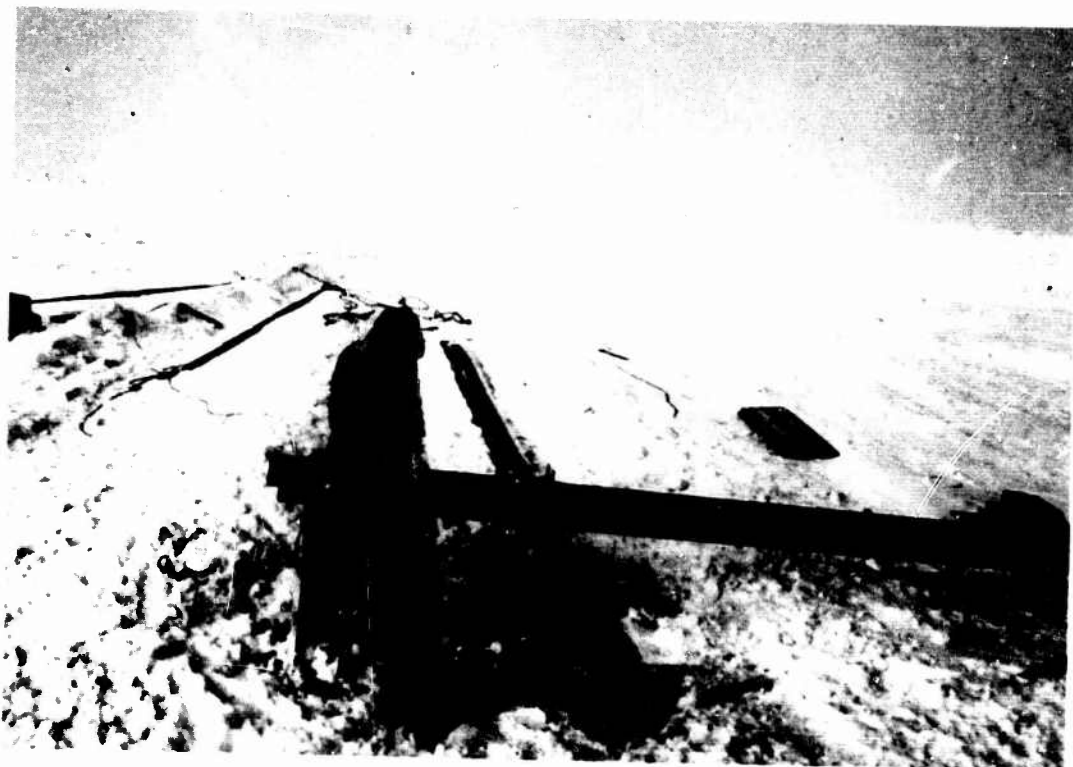


Figure 37. Test setup for field effort to define viscoelastic sea ice behavior.

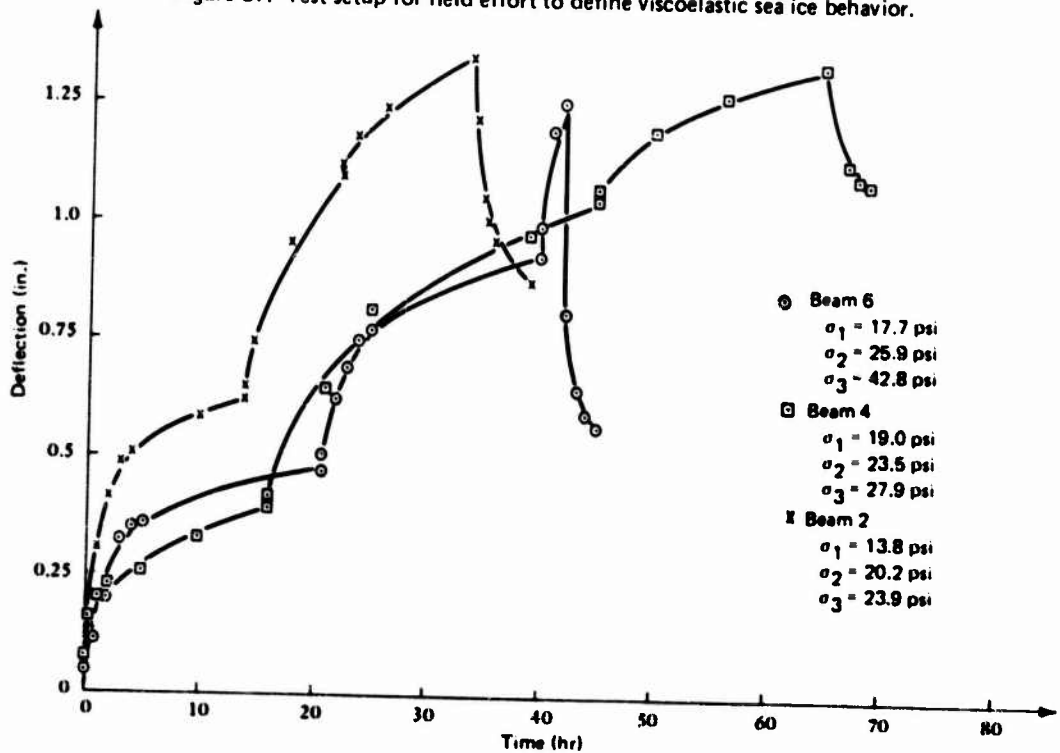


Figure 38. Creep time history for in-situ cantilever beams 2, 4, and 6.

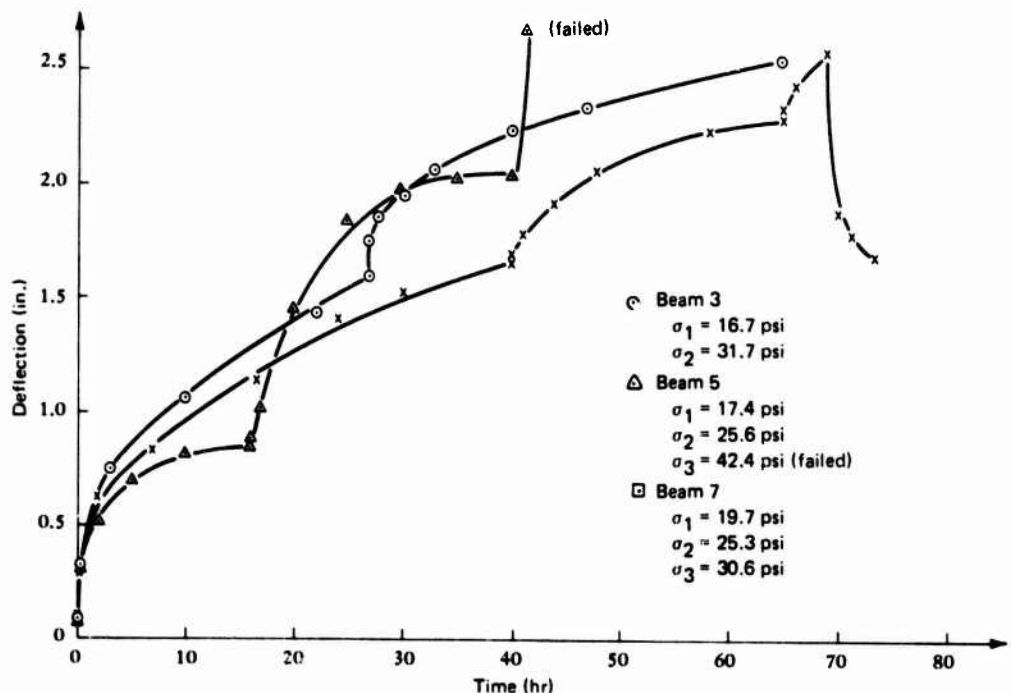


Figure 39. Creep time history for in-situ cantilever beams 3, 5, and 7.

Of course, field tests cannot have the controlled temperature environment of the laboratory; in fact, when a beam is cut in situ, the sides are exposed to seawater, slowly warming the beam from three directions. Consequently, the ice beam is continually warmed throughout the test; therefore, in order to discuss stress-temperature relationships, an average temperature gradient was determined for each test.

The creep curves (deflection-time history of the six cantilever test beams) can be given in the form of strain functions based solely on beam geometrics. First, a displacement function, $u(x)$, is assumed to be of the form

$$u(x) = A_0 + A_1 x + A_2 x^2 + A_3 x^3 \quad (14)$$

and the coefficients can be found from evaluating boundary conditions. Then, strain can be written as

$$\epsilon(x,t) = y \frac{\partial^2 u(x,t)}{\partial x^2} \quad (15)$$

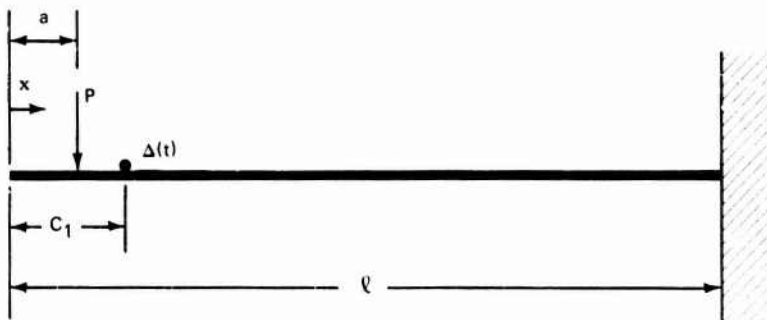


Figure 40. Loading geometry for field testing of viscoelastic sea-ice beams.

where y is the distance from the extreme beam fiber to its neutral axis. For the field ice beams with the geometric configuration of Figure 40, the strain function becomes

$$\epsilon(x,t) = \frac{6y(x-a)\Delta(t)}{(l-c)^2(2l+c-3a)} \quad (16)$$

where $x > a$, l is the beam length, a and c are the distances from the free end to the points of load application and deflection measurement, respectively, and $\Delta(t)$ is the deflection time history for each individual beam test. Equation 16 will be used in a later section on viscoelastic finite-element analysis to determine relaxation functions required for input to the computer code.

ANALYSIS OF FLOATING ICE SHEETS

Initially, the problem of safe bearing capacity of floating ice sheets was analyzed by thin-plate theory, assuming the ice to be an elastic plate resting on an elastic foundation of the Winkler type. Then, development of an elastic finite-element computer code provided

an analytical approach based on two-dimensional elasticity which can easily handle the temperature gradient across the ice-sheet thickness. More recently, the finite-element technique has been expanded to include viscoelastic, as well as elastic, behavior of sea-ice sheets. All three analytical approaches are summarized in the following sections.

Elastic Plate on an Elastic Foundation

A floating annual ice sheet of infinite size can be analyzed by elastic theory as a plate resting on an elastic foundation (20, 21). The ice sheet has flexural rigidity; as it deflects, there is a restoring force due to the water pressure that is proportional to the deflection. Simplifying assumptions in the criteria were: (1) the ice behaves as an isotropic medium, (2) its relaxation characteristics are outside the domain of the loading times, and (3) the moving surface loads do not create resonance wave conditions in the plate.

Plate theory with small deflections may be used to determine the critical stress causing the initial cracking of the plate. Hertz (22) was the first to solve this problem for a uniform load

distributed over a circular area. Wyman (23) expressed the solution in terms of Kelvin functions, where the maximum stress and deflection occurring under the loading center are

$$w_{\max} = \frac{P}{\pi k l^2} \left[\frac{1 + (a/l) \operatorname{ker}'(a/l)}{(a/l)^2} \right] \quad (17)$$

$$\sigma_{\max} = \frac{3P(1+\mu)}{\pi h^2} \left[\frac{\operatorname{kei}'(a/l)}{(a/l)} \right] \quad (18)$$

where w_{\max} = the maximum vertical deflection

σ_{\max} = the maximum tensile stress

P = the total load

k = the foundation modulus (unit weight of seawater)

a = the radius of load distribution

$l = \left[\frac{Eh^3}{12k(1-\mu^2)} \right]^{1/4}$ is a characteristic length called action radius

h = the plate thickness

E = the modulus of elasticity

μ = Poisson's ratio

One limitation on the above theory is that the radius, a, of the loaded area should be large in comparison to the thickness h of the plate. Tracked vehicles usually meet this requirement, but wheeled vehicles or aircraft do not. For a small radius of loading, thin-plate theory predicts a stress that is too high. Westergaard (24) investigated this problem for a simply supported plate and

determined numerically that when $a/h > 1.724$, the critical stress given by thin-plate theory is valid. For $a/h < 1.724$, the radius of the load circle should be recomputed by the following equation,

$$a_1 = (1.6a^2 + h^2)^{1/2} - 0.675h \quad (19)$$

where a_1 = adjusted load circle radius

a = actual load circle radius

h = ice sheet thickness

Of course, superimposing the load effects of several aircraft landing gear, vehicle wheels, or tracks is necessary to determine the actual stress and deflection in the ice sheet. The superposition of the components of stress for the remaining loads onto the initial stress condition produced by the load at the zero coordinate point and given by Equation 18 can be accomplished by a summation of partial derivatives of the bending effect relative to the coordinate position of the particular load. If we let $v_i = w_i/P$, where w_i = plate deflection produced by any one of the off-zero coordinate loads, then

$$\begin{aligned} \frac{\delta^2 v}{\delta x^2} &= \sum_i \frac{\delta^2 v_i}{\delta x^2} \cdot \frac{\delta^2 v}{\delta y^2} = \sum_i \frac{\delta^2 v_i}{\delta y^2} \cdot \frac{\delta^2 v}{\delta x \delta y} \\ &= \sum_i \frac{\delta^2 v_i}{\delta x \delta y} \end{aligned} \quad (20)$$

The total deflection of the ice plate from loading by aircraft or vehicles was calculated by the same general technique used for stress calculation, starting with Equation 17 for the deflection of the zero-coordinate load.

Elastic Finite Element Method

To avoid the limiting assumption of thin-plate theory with regard to the loading circle radius, to incorporate thermal gradient effects of the ice sheet, and to provide a versatile numerical tool for evaluating ice-sheet bearing capacities, an elastic finite-element computer code was developed at CEL. The program is based on two-dimensional elasticity with the structural system idealized as an axisymmetric solid composed of an arbitrary number of layers (4, 25). These layers may have orthotropic or temperature-dependent material properties. The solid is supported by a fluid foundation and loaded by transverse uniform circular loadings of arbitrary radius and magnitude. A superposition routine allows positioning of loads to simulate aircraft gear configurations, half tracks, or other heavy equipment vehicles. The full details of the development and limitations of the code, as well as a user manual and example input, are given in Appendix A.

Of primary importance is that the finite-element code does not embody any assumptions deviating from classical elasticity - aside from the fundamental, assumed, displacement field over each element, which is characteristic of the finite-element technique. However, it has been shown that, as the number of elements is increased, the solution will converge to the exact solution; therefore, by successive trials an "exact-as-you-wish" solution may be obtained.

As a check on the computer code the strain results of the sea-ice plate studies are compared with analytical solutions from the finite-element method. A description of the laboratory plate experiments has already been presented in a previous section.

Consequently, only details pertinent to strain measurement will be discussed. The four gages (Figure 25) were grouped in two pairs, so that each pair measured strain in two orthogonal directions and their average cancelled any anomalies arising from asymmetric responses. Strains were continuously recorded, and peak values were easily distinguished. This pattern was repeated for different peak load values. The top gages in the compression zone exhibited linear behavior, whereas the tension gages suggested a nonlinear response, perhaps due to tensile cracking of the sea ice.

Four constant-temperature tests were conducted on a single 4.5-in. plate at the temperatures: -4, -10, -20, and -30 C. Figure 41 shows the average experimental radial strains for both gages located in the tension and compression zones at each test temperature. The analytical strain distributions predicted by the finite-element technique for each plate test are superimposed on each figure. For the analytical approach, the sea ice was assumed to be homogeneous, isotropic, and elastic, with Poisson's ratio taken as 0.3 for all temperatures. Young's modulus was determined from plate-theory equations by using the experimental strains as input. The experimental strains deviated somewhat from plate-theory kinematics in that the experimental strain values at the tension and compression zone did not form a straight line through the plate centroid. Therefore, in determining Young's modulus, more weight was given to the compression gage as it was postulated that the tension strains were influenced by cracking. The computed modulus is noted in each figure.

Examination of the results of the constant-temperature plate tests yields the following observations.

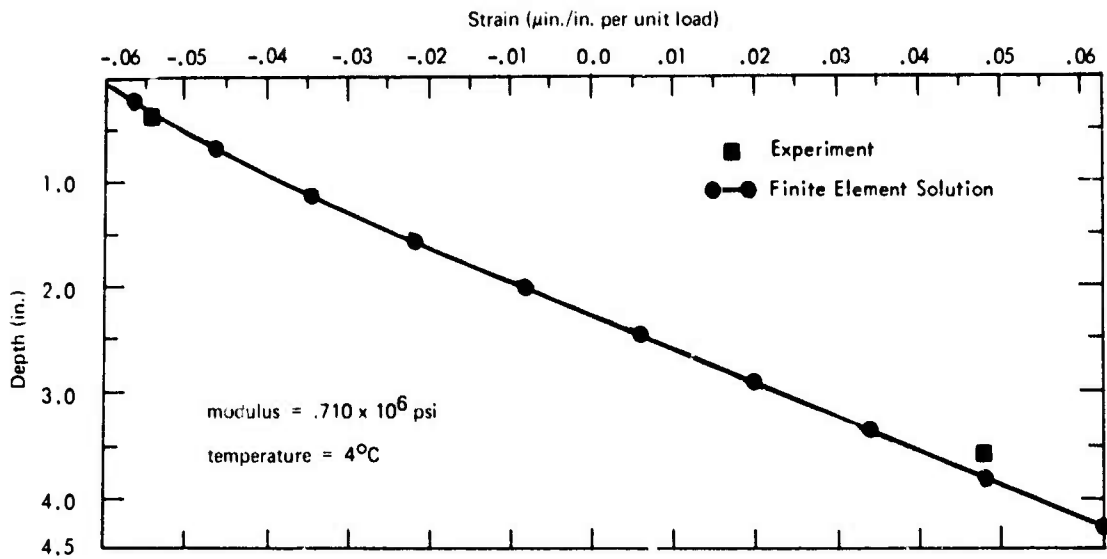


Figure 41a. Strain profiles on centerline of 4-1/2-in. sea-ice plate at a temperature of -4°C .

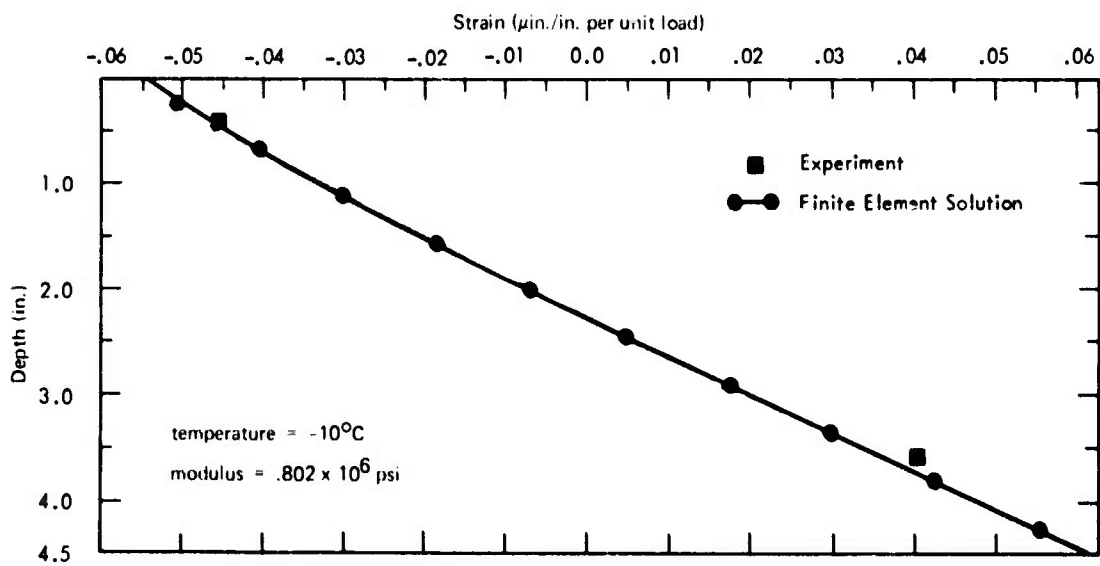


Figure 41b. Strain profiles on centerline of 4-1/2-in. sea-ice plate at a temperature of -10°C .

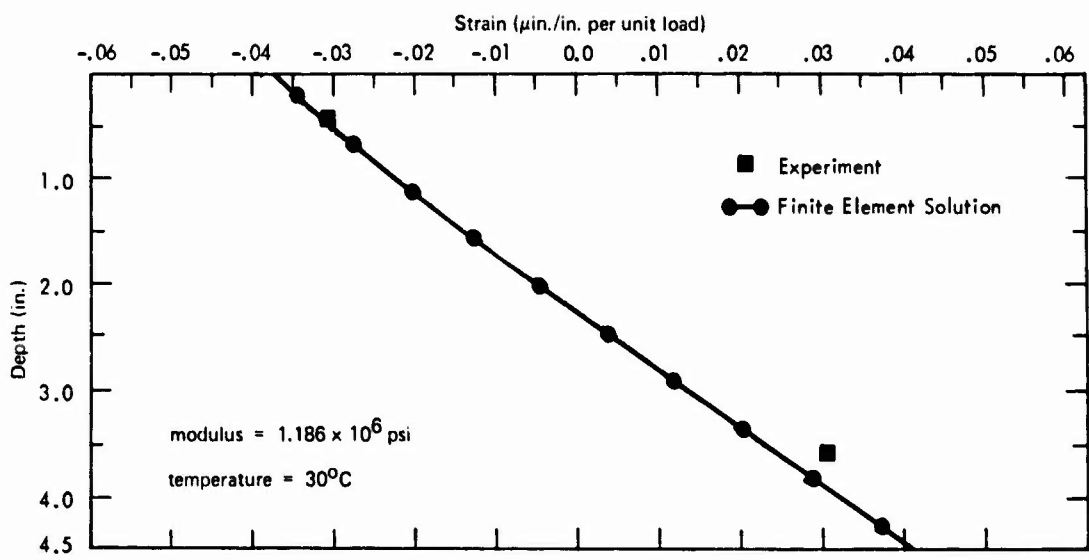


Figure 41c. Strain profiles on centerline of 4-1/2-in. sea-ice plate at a temperature of -20°C .

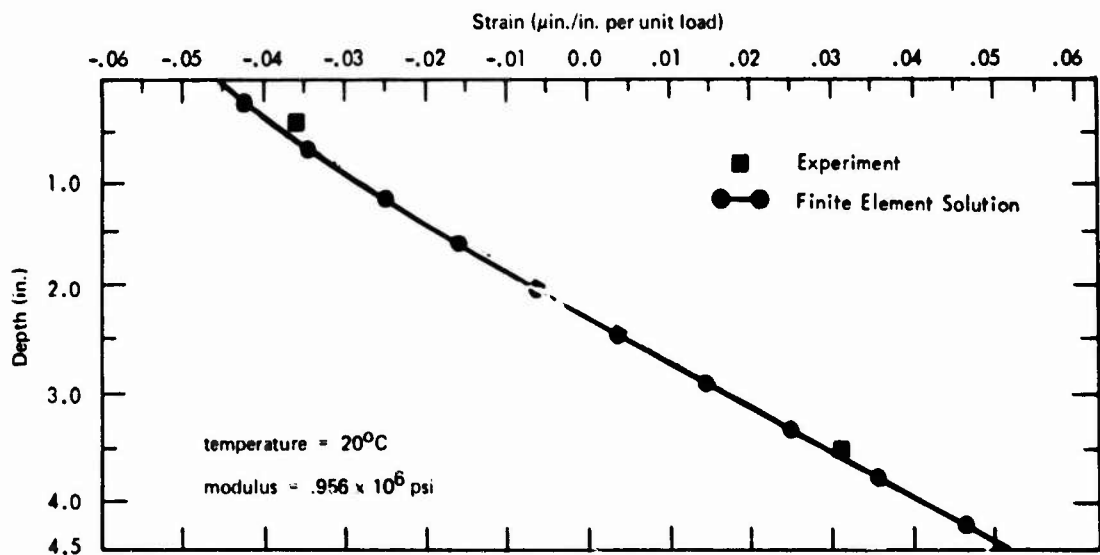


Figure 41d. Strain profiles on centerline of 4-1/2-in. sea-ice plate at a temperature of 20°C .

1. The analytical approach is in excellent agreement throughout the ice thickness, even in the top fiber compression zone. This agreement is to be expected, since the plate dimension ratio - diameter-to-thickness - is on the order of 10, which is the rule-of-thumb if thin-plate theory is to be valid for plates of finite extent.

2. It can be observed that the experimental strains in the tension zone are consistently larger than the analytical predictions, which motivated the contention that the tension gages experienced a nonlinear response, perhaps due to tension cracks.

3. It is confirmed that the calculated moduli demonstrate a consistent relationship with the plate temperature, such that colder temperatures produce higher moduli.

Two experiments were conducted on sea-ice plates with linear temperature gradients induced across the plate thickness: -11 to -6°C and -19 to -9°C from top to bottom, respectively. Otherwise, the tests were identical to those with constant-temperature plates. Figures 42a and b show the average measured radial strains along with the radial strain profile from the finite-element solution.

Again, in determining the analytical solution, the sea ice was assumed isotropic and elastic with Poisson's ratio set at 0.3; however, the modulus was assumed to vary linearly across the plate thickness. In order to determine this linear distribution, the unique modulus distribution which produced a strain profile capturing both the compressive and tensile experimental strains was chosen. These modulus distributions are given in their respective figures in terms of the maximum and minimum moduli at the top and bottom of the ice plate.

Viscoelastic Finite-Element Technique

Viscoelastic materials are often called "memory" materials; that is, the stress in the material is determined not only by the current state of deformation but also by all past deformation states. Moreover, the "memory" exhibits a fading phenomenon in that past deformation states influence the current stress state to a lesser degree than do more recent deformation states.

It is known that sea ice behaves elastically only for small to moderate load magnitudes applied over short time periods. To expand the range of load magnitudes and time durations, the theory of linear viscoelasticity (26, 27) has been coupled with the finite element technique to provide more realistic characterization of sea-ice behavior.

A general summary of the viscoelastic finite element formulation (5) is presented in this section while details of the development, as well as computer code user instructions, appear in Appendix B. The general, isotropic, two-dimensional viscoelastic stress-strain relationship is presented as a matrix of Stieltjes integrals along with a special characterization of the material relaxation functions known as a Prony series. Then the viscoelastic constitutive relation is incorporated into a finite-element formulation for axisymmetric/plane strain geometry (5). The scope of the mechanics is limited to isothermal linear viscoelasticity, small-deformation theory, and quasi-static loading. However, the inclusion of inertial terms for dynamic analysis is a straightforward extension of this work. The principle of virtual work is utilized to develop a displacement formulation for the viscoelastic model for a generic class of two-dimensional finite elements.

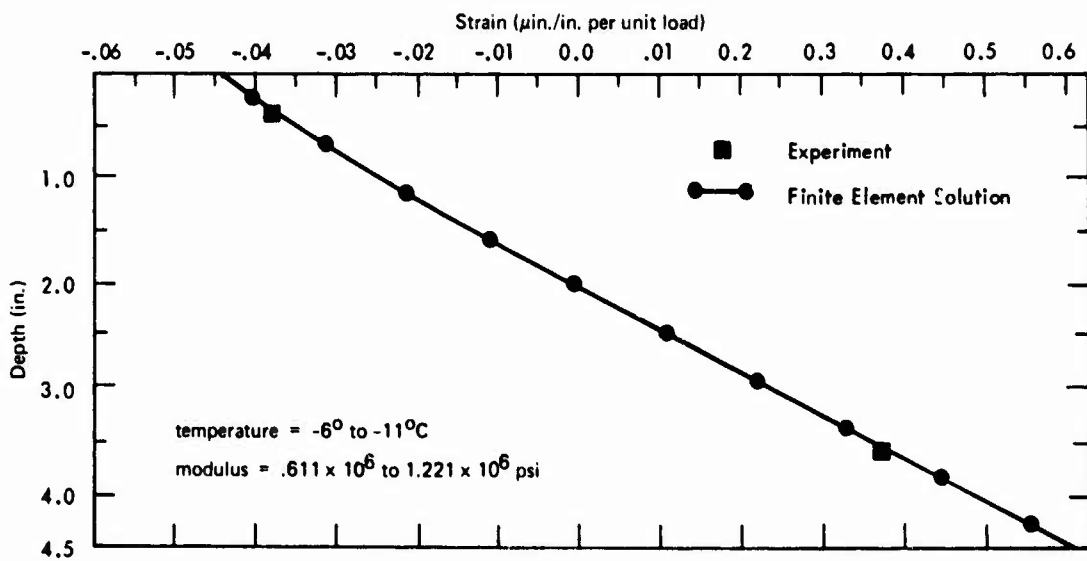


Figure 42a. Strain profiles on centerline of 4-1/2-in. sea-ice plate at a temperature gradient of -11 to -6°C .

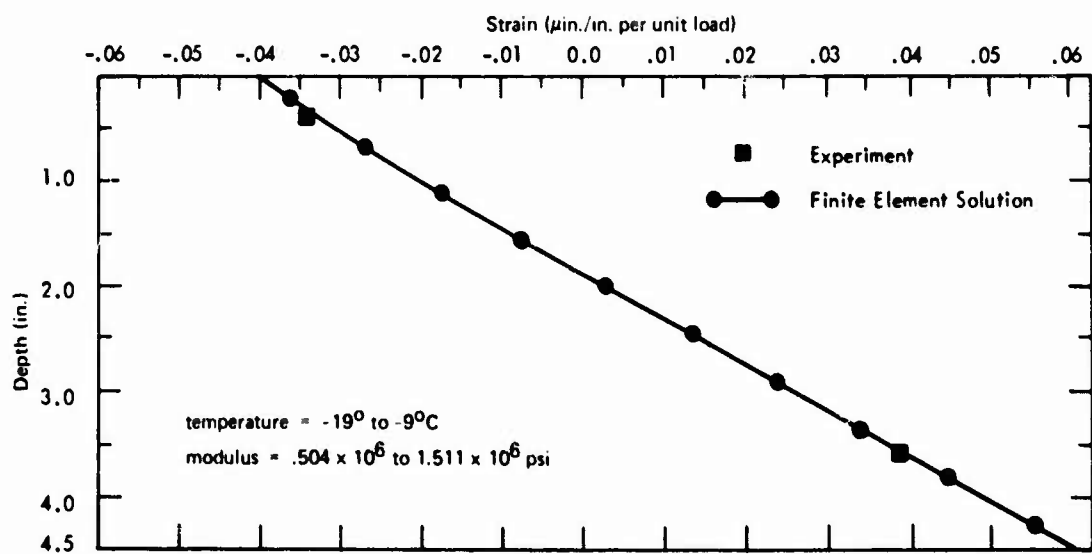


Figure 42b. Strain profiles on centerline of 4-1/2-in. sea-ice plate at a temperature gradient of -19 to -9°C .

A fluid foundation is incorporated into the formulation for plate-type structural systems, as well as a superposition technique for handling arbitrary surface loads on layered half-space systems.

The finite-element formulation requires that time-dependent sea-ice properties be given in the form of relaxation functions for both the bulk and shear moduli, $K(t)$ and $G(t)$.

$$K(t) = K_0 + \sum_{i=1}^n K_i e^{-t/\lambda_i} \quad (21)$$

$$\text{and } G(t) = G_0 + \sum_{i=1}^n G_i e^{-t/\beta_i} \quad (22)$$

Here the relaxation functions are represented by a constant and a series of exponential terms where $K_0, K_1, \dots, K_n, G_0, G_1, \dots, G_n$ are positive constant moduli value with units of stress, and $\lambda_1, \lambda_2, \dots, \lambda_n, \beta_1, \beta_2, \dots, \beta_n$ are positive constants called "relaxation times."

In this prony series form, the relaxation functions are capable of representing a large class of linear viscoelastic materials. In essence any linear viscoelastic material which exhibits an instantaneous elastic deformation followed by a creep phase can be modeled by Equations 21 and 22 with a sufficient number of exponential terms. In practice, the use of more than four exponential terms is seldom justified; usually two terms are sufficient.

Relaxation Functions From Creep Data. Strain histories from previously discussed uniaxial and beam experimental effort must be converted into relaxation functions. First, all creep data should be discretized into data points at specified times. Then, the objective is to

fit a creep function, $J(t)$, in the form of a prony series.

$$J(t) = J_0 + \sum_{i=1}^m J_i e^{-t/\lambda_i} \quad (23)$$

where $J(t)$ is defined as the strain history response to a prescribed unit Heaviside stress input. This curve-fitting technique can be accomplished by a linear least-square error analysis based on $m+1$ unknown creep moduli, J_0, J_1, \dots, J_m , with preselected retardation times, λ_i , which can be optimized by trial and error. Once $J(t)$ is determined, using LaPlace transformation - the inverse of $J(t)$, the relaxation function, $Y(t)$, can be found. However, while $Y(t)$ is of the form of Equation 23, it does not represent either the bulk, $K(t)$, or shear, $G(t)$, relaxation functions, but rather $Y(t) = E(t)$, the Young's modulus relaxation function. Assuming Poisson's ratio, μ , to be constant, then the relaxation functions for the bulk and shear moduli are easily determined by the following relations:

$$K(t) = \frac{E(t)}{3(1-2\mu)} \quad (24)$$

$$G(t) = \frac{E(t)}{2(1+\mu)}$$

Ice-sheet bending creates a critical biaxial stress state beneath the load where the ice is in tension applied perpendicular to normal crystal growth (horizontally). Consequently, relaxation functions were determined for the uniaxial tensile laboratory creep tests on horizontal specimens (see Figure 32). Each ice temperature has its own governing relaxation function for the modulus of elasticity, $E(t)$.

$$-4^{\circ}\text{C}: E(t) = 1.48(10^5)e^{-t/4.10}$$

$$+ 6.73(10^3)e^{-t/2400} \quad (25)$$

$$-10^{\circ}\text{C}: E(t) = 2.31(10^5)e^{-t/3.58}$$

$$+ 1.07(10^4)e^{-t/2540} \quad (26)$$

$$-20^{\circ}\text{C}: E(t) = 3.79(10^5)e^{-t/3.51}$$

$$+ 1.47(10^4)e^{-t/1350} \quad (27)$$

$$-27^{\circ}\text{C}: E(t) = 5.66(10^5)e^{-t/4.5}$$

$$+ 2.26(10^4)e^{-t/2010} \quad (28)$$

where the term coefficients are given in lb/sq in. while the exponential coefficients are "relaxation times" in minutes.

The same format was followed to calculate the relaxation function $E(t)$ for both -4 and -10C laboratory beam creep data (shown in Figure 35)

$$-4^{\circ}\text{C}: E(t) = 1.71(10^5)e^{-t/3.10}$$

$$+ 5.39(10^3)e^{-t/1340} \quad (29)$$

$$-10^{\circ}\text{C}: E(t) = 2.55(10^5)e^{-t/3.76}$$

$$+ 9.79(10^4)e^{-t/820} \quad (30)$$

Again, the units for both term and exponential coefficients remain the same.

A composite creep function was generated for field beams, representing the deflection-time history of beams 3 and 7 from Figure 39. The resulting relaxation function for $E(t)$ at an average

ice surface temperature of -16C becomes

$$E(t) = 5.23(10^5)e^{-t/6.0}$$

$$+ 4.19(10^4)e^{-t/1510} \quad (31)$$

Good agreement exists between both sets of laboratory results and the field effort. In general, the field beams responded with higher relaxation values for equivalent ice temperatures, but these were averages not taking the entire thermal gradient of the beam into account.

Viscoelastic Ice Plate Example. To demonstrate the capability of the viscoelastic finite-element computer code (5), the structural response of an infinite sea-ice plate on a fluid foundation is investigated for a simulated aircraft loading condition and, using relaxation functions, is determined from experimental creep data. The time-dependent surface deflections of an Arctic sea-ice sheet were measured during a CEL field effort to simulate long-term (4 to 6 days) loading of a C-130 aircraft on floating ice sheets.

The main landing gear were represented by four wood blocks, each having the same area as each tire print of a C-130. These blocks were placed at the corners of a 5 x 14 ft rectangle, the same spacing as the aircraft wheels. A series of 900-gallon (3.4 kiloliter) fuel bladders were stacked on a deck spanning across the wood blocks and filled with seawater by a 600-gpm pump. The test setup is shown in Figure 43. Of course, the entire weight of a fully loaded C-130 could not be placed on the loading platform, but a P/h^2 ratio of ≈ 60 psi was attained for the relatively thin ice sheet, ranging from 20 to 24 in. This ratio corresponds to a C-130, weighing 180,000



Figure 43. Test setup for simulating a parked C-130 aircraft on an annual ice sheet.

lb, parked on a 55-in.-thick ice sheet.

No radial or circumferential cracking was observed, but ice deflections were measured beneath the load by means of a manometer containing antifreeze and radially outward from the load by taking level readings. To determine the actual applied load, all platform components were weighed, and a flowmeter monitored the number of gallons of seawater pumped into the bladders. Temperature and salinity profiles were measured several times during the test period. Salinities remained fairly constant, averaging between 5.5 to 6.0 ppt, while average ice-sheet surface temperatures ranged from -8 to -30C.

Two of the deflection time histories from the ice-sheet creep tests are shown in Figure 44 for two different loadings and ice thicknesses. The solid lines are results of the finite element analysis.

The thin ice sheet of Test 2 was approximated by a single layer with an average temperature of -10C. The relaxation functions for bulk and shear moduli were calculated by substituting Equation 26 into Equation 24. In Test 3 the ice sheet had a significant temperature gradient across the thickness, so two layers were used in the analysis: the top layer having a mean temperature of -24C and the bottom -10C. To model the time-dependent material properties of this ice sheet, two sets of bulk and shear relaxation functions were computed from Equations 26 and 28 obtained from uniaxial laboratory studies. Both experimental and analytical results represent wheel deflections, including the effects of superposition by the other three wheels. Both analyses agree with field measurements very closely, not differing by more than 0.5 in. during 80 hours of testing.

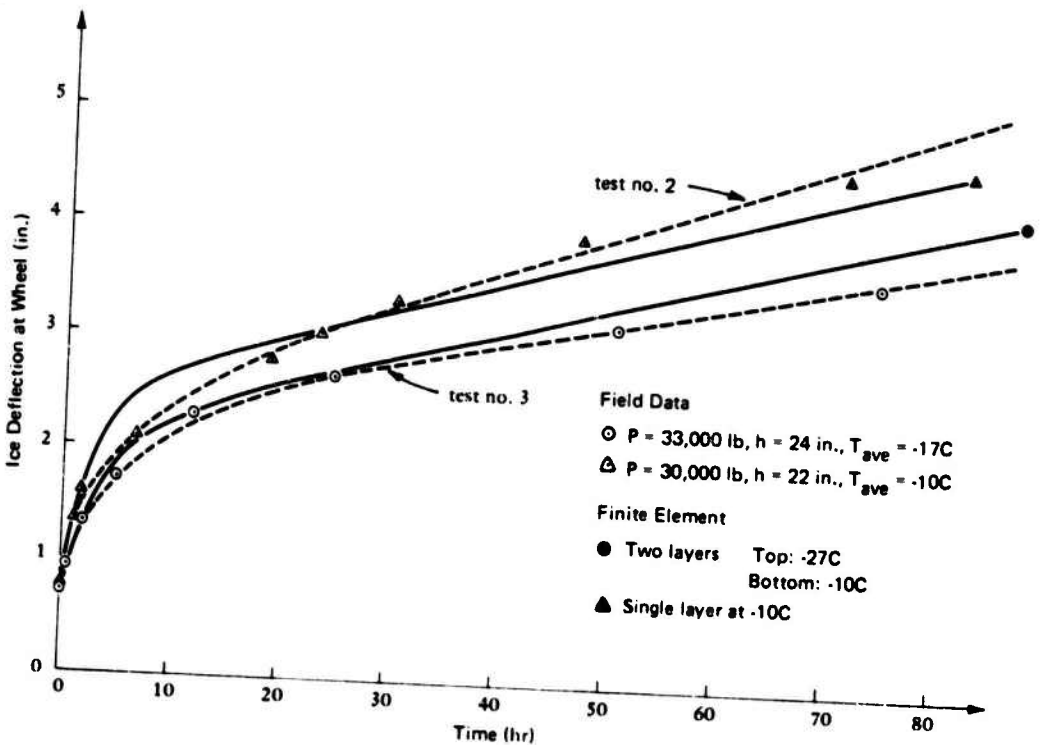


Figure 44. Comparison of ice deflection time histories using field data and finite element analysis of simulated parked C-130 aircraft.

BEARING CAPACITY OF FLOATING ICE SHEETS

Once field and laboratory experimentation establishes reasonable values for sea-ice mechanical properties and analytical approaches have been devised to adequately model sea-ice behavior, it is possible to solve real ice-sheet problems, such as landing and parking aircraft, moving vehicular traffic, and storing cargo. A rational utilization of floating ice plates for all these operations requires the knowledge of their bearing capacity when they encounter short- and long-term loading. In the past, numerous attempts have been made to determine the bearing capacity of ice sheets subjected to vertical loads. A critical literature survey of the subject has been written by Kerr (28).

Failure Criteria

The most widely used method for predicting the bearing capacity of a floating ice sheet subjected to short-duration loads is based on a maximum stress, σ_{\max} , in the ice sheet, determined for a given load and assuming that the ice plate is elastic. Next, the load, P_{cr} , at which the first crack occurs is found using the criterion

$$\sigma_{\max} = \sigma_f \quad (32)$$

where σ_f is generally given as an experimental tensile or flexural failure stress. Of course, P_{cr} does not cause a complete breakthrough failure of the ice sheet; in fact, using P_{cr} does provide a built-in factor of safety. Usually,

however, an allowable load, P_{all} , is calculated as some percentage of P_{cr} to provide an additional safety factor.

To support loads for extended periods of time, the theory of elasticity is no longer valid for analysis. Applying the theory of linear viscoelasticity, deflection-time histories can be predicted. One common criterion states the maximum deflection should not exceed the freeboard of the ice sheet, generally taken as $0.08 h$, where h is the ice-plate thickness (29). If the freeboard is exceeded, water can flood the surface through cracks and disrupt activities. This criterion is definitely conservative and safe, and a maximum deflection criterion of

$$w_{max} = 0.1 h \quad (33)$$

is used to determine allowable parking times for vehicles and aircraft on floating ice sheets. Even though Equation 33 represents a 25% increase over the freeboard criterion, Kingery (30) has indicated there was no failure during field tests, even for deflection ratios, w/h , greater than 0.25.

Computer Code Input Parameters

Elastic Finite Element Method. The input requirements for the elastic finite-element code are based on a circular, plate-shaped solid, supported by a fluid foundation. The ice sheet can be of arbitrary dimensions with as many as 12 material layers and can accommodate circular loadings of uniform pressure but arbitrary radius and magnitude. These input parameters can be divided into three basic categories: (1) program control and finite-element mesh generation, (2) ice-sheet material properties, and (3) aircraft or vehicle loading conditions.

The first category sets the boundary conditions and defines the number of material layers and number of element rows for each layer of the ice sheet. Also, the mesh generator establishes the number of total elements, elements under the load, and elements in contact with the supporting fluid.

In the second category, temperatures are assigned to the top and bottom of different material layers within the ice sheet, along with a corresponding elastic modulus and Poisson's ratio for each temperature. The thickness for each material layer is given, as well as the density of the fluid foundation (in this case, seawater).

For the last category, the input parameters are the number of circular loadings (e.g., wheels or tracks) and the total load (weight of aircraft or vehicles), in addition to such individual wheel or track circle characteristics as (1) the radius and pressure of load; (2) the x-y coordinates (to locate each loading); and (3) the fraction of total weight carried by each individual loading. Details of all of these input parameters are presented in Appendix A.

Viscoelastic Finite Element Method.

The input requirements for the viscoelastic computer code are similar to those for the elastic code, except for the consideration of time dependency (5). Again, the infinite ice sheet is assumed to be a large circular, plate-shaped solid of arbitrary dimensions resting on a fluid foundation. The ice sheet can have as many as 12 layers with separate material properties and be subjected to any number of circular loadings of uniform pressure, but with arbitrary radius and magnitude. The input parameters fall into five different categories: (1) program control and finite element mesh generation, (2) time-dependent material

Table 1. Annual Ice-Sheet Mechanical Properties

Thermal Period	Surface Temperature (°C)	Elastic Modulus Gradient (psi x 10 ⁵)	Flexural Strength (psi)
1	-20 to -10	7.0 to 2.9 ^a	70.0
2	-10 to -5	6.0 to 2.9 ^a	62.0
3	-5 to -3	4.0 to 2.9 ^a	58.0
4	-3 to -2	2.9 ^b	40.0

^aCorresponds to temperature gradient, top to bottom.

^bIsothermal condition.

properties for each ice-sheet layer, (3) time information, (4) aircraft or vehicle loading conditions, and (5) output control and suppression.

As before, the first category established the boundary conditions and defines the number of material layers and element rows for each layer of the ice sheet. The mesh generator sets the number of total elements, elements under the load, and elements in contact with the fluid foundation.

In the second category, modulus coefficients and relaxation times are input for both exponential series defining the bulk and shear moduli for each ice layer. The thickness of each layer is given as well as the density of the supporting fluid foundation.

In the third category, both the time-step increment and total number of time steps must be input, as well as the load duration.

For the fourth group the input parameters are the number of circular loadings, total load, and individual tire-print characteristics: (1) the radius and pressure, (2) the x-y coordinates (to locate each loading on the ice sheet), and (3) its percentage of the total weight.

The fifth category simply gives the user the opportunity to control the printed output (deflections, stresses, and strains). All of these input parameters

are explained in more detail in the user instructions section of Appendix B.

Aircraft Load Curves

Calculating the required effective ice-sheet thicknesses for the load ranges of different aircraft requires exercising the elastic finite element computer code in two series of repeated steps (31). Initially, the input parameters for a single thermal period are selected from Table 1, and several ice-sheet thicknesses are chosen for this period. By performing consecutive computer runs, maximum tensile stresses are found at the bottom of the ice sheet for each specified thickness. This iterative process generates an aircraft-load versus ice-thickness curve for a given thermal period, and the entire cycle is repeated for the remaining periods. In Figure 45 curves for both C-130 and C-141 military aircraft are shown for all four thermal periods defined in Table 1. Period 1 curves for both aircraft are determined by comparison of the calculated stresses with an allowable stress that is found by reducing beam failure strengths by 30% (an equivalent safety factor of 1.20). All other curves reflect a reduction of 25% in the failure strength, representing a safety factor of 1.15.

Vehicle Ice Thickness Table

Minimum ice-sheet thicknesses for typical polar vehicles are presented in Table 2 (31). Again, the iterative process is repeated for each thermal period. However, for relatively constant loads (like vehicles), the iterations converge to a single, tabular point rather than forming a curve as in the case of aircraft, which have a wide cargo/fuel range. All vehicles are a sampling of typical logistics support equipment

operating in polar regions. Vehicle weights used in thickness calculations are also given in Table 2. Allowable stresses represent a sufficient reduction in failure strength to produce a safety factor of 1.50.

Allowable Parking Times for Aircraft

Maximum allowable parking times in hours for both C-130 and C-141 aircraft are presented in Table 3. Using the viscoelastic finite element computer code (5), time-dependent deflections beneath the main landing gear of both aircraft were calculated for three separate ice-sheet thicknesses at each thermal period of operation. The first ice thickness listed for each period was taken from the minimum ice thickness curves in Figure 45 for the particular aircraft weight. An aircraft can hardly be allowed to park on an ice sheet thinner than landing thickness. The remaining two ice thicknesses were simply 6 and 12 in. greater than the first. The four seasonal periods are defined by the surface ice temperatures listed in Table 1, but the elastic modulus gradients presented in Table 1 are invalid for these time-dependent cases. Thus, for thermal period 1 the ice sheet was divided into four layers, each governed by its own set of relaxation functions for bulk and shear moduli calculated from Equations 25 through 28. For period 2 the ice sheet was divided into three layers, using relaxation functions based on Equations 25 through 27. This pattern was repeated for period 3 using three layers, while the ice sheet was considered virtually isothermal for period 4, governed only by Equation 25. The failure criterion in Equation 33 was applied to determine the allowable parking times. Superposition was employed to consider contributions from all other aircraft wheels. It should

be noted that during these computer simulations of parked aircraft, the principal biaxial tensile stresses at the bottom of the ice sheet relaxed on the order of 60% of their initial value at $t = 80$ hr. The fact that stresses are reduced as time goes on should encourage the development of a failure criterion for sea-ice sheets based on limiting strain.

Operational Field Procedure

Once ice-thickness curves and tables are determined, proper field procedure is still necessary to operate safely on any ice sheet. Of course, both ice thicknesses and temperatures must be monitored. At the start of the operating season, a detailed thickness survey should be made down each edge of sea-ice runways, alongside ice roads, and around all other operating areas. Maintenance of a complete up-to-date temperature record of the ice sheet is necessary for a verification that the proper thermal period is being used. Ice temperatures should be measured by thermocouple or thermistor stations at five or more locations dispersed for general coverage of the entire operational area. Routine inspection of the ice-sheet surface should be made for existence of cracks. Such cracks should be recorded for length, location, and whether they are wet or refrozen.

CONCLUSIONS

1. The comprehensive testing program on the mechanical properties of sea ice has provided a wealth of basic information necessary for understanding sea-ice behavior under different loading conditions.

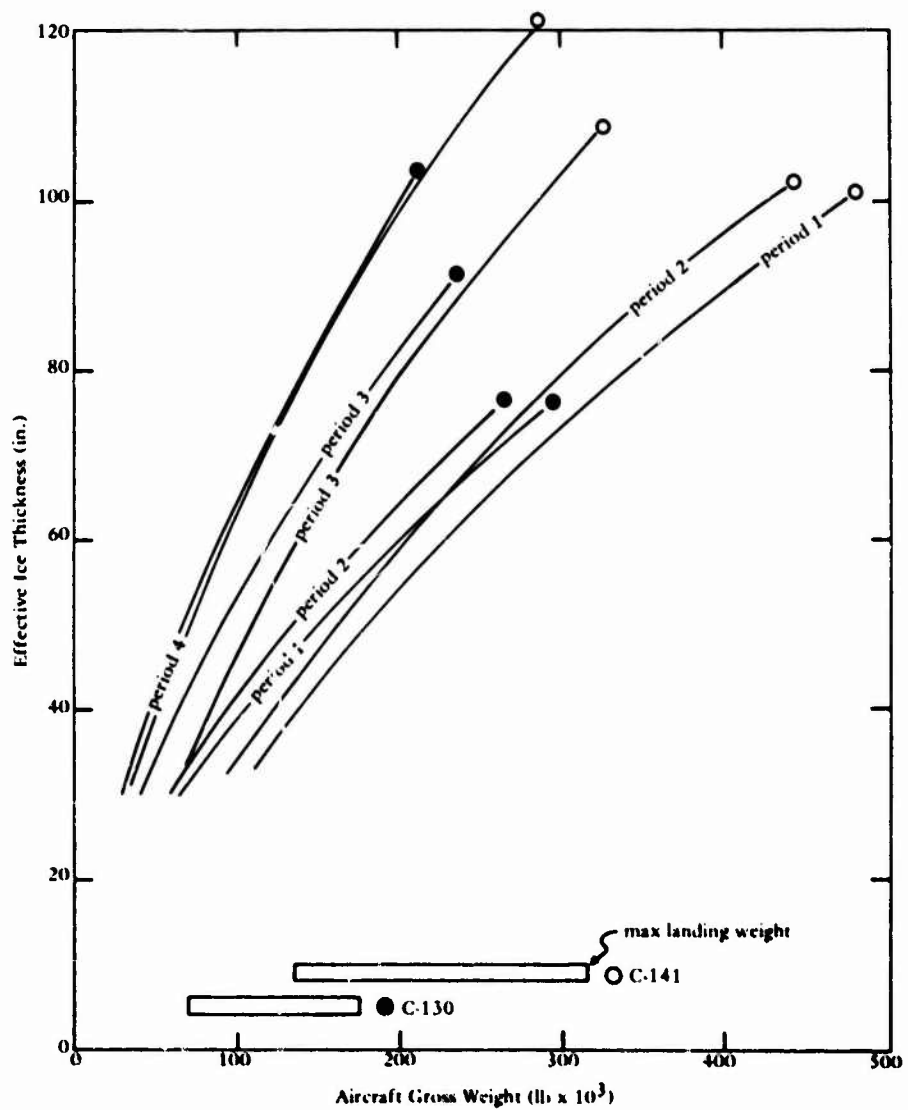


Figure 45. Load curves for both C-130 and C-141 aircraft over four thermal periods.

Table 2. Minimum Allowable Ice Thicknesses for Representative Equipment and Vehicles

Vehicle or Equipment	Minimum Allowable Ice Thickness (in.)			
	Thermal Period 1	Thermal Period 2	Thermal Period 3	Thermal Period 4
1. Pickup, 1T-Dodge W300 (GVW = 9,000 lb) ^a	11	13	17	21
2. Cargo/personnel-Nodwell 45TT (15,000 lb)	16	18	23	28
3. Personnel carrier-Nodwell RN110 (GVW = 27,500 lb)	17	21	28	34
4. Personnel carrier-Trackmaster 601 (7,540 lb)	10	12	16	20
5. Caterpillar D-4 STD (17,250 lb)	20	24	31	38
6. Caterpillar D-8 LGP (85,000 lb)	44	48	59	71
7. Caterpillar 950 (24,900 lb)	24	28	35	42
8. Caterpillar 955 STD (30,200 lb)	29	33	42	50
9. Road grader - Cat 12F (28,310 lb)	26	29	37	44
10. Crane, wheeled-Pettibone 70 (70,730 lb)	40	45	57	69
11. 5T tractor (military) + 12T trailer (Fruehauf) (GVW = 56,000 lb)	27	31	39	43
12. 10T tractor (Fabco) + 20T trailer (Fabco) (GVW = 65,000 lb)	29	33	42	51
13. 10T tractor (military) + 60T lowboy (military) (GVW = 180,000 lb)	52	58	74	88
14. Caterpillar D-8 LGP + 20T sled (GVW = 145,000 lb)	45	51	61	72

^aGVW is gross vehicle weight.

Table 3. Allowable Parking Times for C-130 and C-141 Aircraft for Different Ice-Sheet Thicknesses

Thermal Period ^a	Ice-Sheet Thickness (in.)	Allowable Parking Times (hr)	Ice-Sheet Thickness (in.)	Allowable Parking Times (hr)
C-130 Aircraft ^b		C-141 Aircraft ^c		
1	54	7	74	15
	60	16	80	31
	66	37	86	43
2	60	8	78	14
	66	21	84	28
	72	42	90	44
3	76	55	102	106
	82	87	108	121
	88	122	114	152
4	90	97	122	149
	96	130	128	180
	102	164	134	208

^aDefined by ice temperatures from Table 1.

^bAircraft weight, 180,000 lb.

^cAircraft weight, 300,000 lb.

2. Two finite-element computer codes developed at CEL have established a capability to analyze ice-sheet behavior through the viscoelastic range. This analytical software has the ability to consider the influence of the existing temperature gradient across the ice sheet and to handle multiple wheel or track loadings on the ice sheet.

3. By a combination of mechanical property testing and finite-element analysis, workable, realistic ice thickness requirements have been determined for aircraft and vehicle operations on floating sea-ice sheets, as well as

allowable times for parked aircraft and effects of cargo/fuel storage and snow overburden near ice-sheet operations.

RECOMMENDATIONS

1. Further experimental and analytical effort is recommended to develop an accurate, sensible failure criterion to better define the safe limits of long-term sea-ice-sheet behavior.
2. Any further laboratory or field testing of sea ice will require better strain and deflection measurement techniques to

insure accurate and reliable deformation data necessary to establish any failure criterion or to verify developed constitutive relations.

3. It is recommended that a user manual be prepared containing a complete and detailed description of the application and limitations of the finite-element computer codes, including a complete listing of computer programs, input format, and varied examples to illustrate the solution of elastic and viscoelastic ice problems. The manual preparation should be preceded by a thorough review of the computer codes for restructuring the program toward simplification to assist the practitioner who may not be highly skilled in computer technology.

4. As an ultimate goal, it is recommended that viscoplastic theory be incorporated into a finite-element program for analyzing systems composed of sea ice. Viscoplasticity is a logical extension of linear viscoelastic theory such that plastic flow is also included in the formulation. For example, viscoplastic models are capable of replicating primary, secondary, and tertiary deformation characteristics of sea ice. Moreover, nonlinear and time-dependent failure criteria are inherent in the formulation. Further, these failure criteria (i.e., flow laws) can be rationally defined to exhibit different behavior characteristics for tension and compression stress states as is observed with sea ice.

Preliminary investigations of applying viscoplastic models to sea ice have been extraordinarily encouraging (32). It is recommended that these models be vigorously researched and developed as the final answer to the characterization of sea ice.

ACKNOWLEDGMENTS

The author thanks Mr. J. E. Dykins for his consultation and direction on sea-ice mechanical property tests and for his technical review of this manuscript. Thank-yous go to Dr. Michael Katona for the development of the finite-element computer codes and consultation on ice-sheet analysis, and to Ms. Barbara Hamilton for editing and typing of the report draft. The author expresses his gratitude to Messrs. Michael Thomas and Jess Mooney for their long hours in the cold, preparing and testing sea-ice specimens both in the laboratory and the field, and for their innovative ideas to improve experimental techniques.

REFERENCES

1. Naval Civil Engineering Laboratory. Technical Report R-415: Ice engineering - tensile and bending properties of sea ice grown in a confined system, by J. E. Dykins. Port Hueneme, Calif., Jan 1966.
2. ———. Technical Report R-689: Ice engineering - tensile properties of sea ice grown in a confined system, by J. E. Dykins. Port Hueneme, Calif., Jul 1970.
3. ———. Technical Report R-720: Ice engineering - material properties of saline ice for a limited range of conditions, by J. E. Dykins. Port Hueneme, Calif., Apr 1971.
4. ———. Technical Report R-797: Ice engineering - summary of elastic properties research and introduction to viscoelastic and nonlinear analysis of saline ice, by M. G. Katona and K. D. Vaudrey. Port Hueneme, Calif., Aug 1973.

5. ——. Technical Report R-803: Ice engineering: viscoelastic finite element formulation, by Michael G. Katona. Port Hueneme, Calif., Jan 1974.
6. Army Cold Regions Research and Evaluation Laboratory. Report CRSE-II-C3: The mechanical properties of sea ice, by W. Weeks and A. Assur. Hanover, N.H., Sep 1967.
7. A. Assur. "Composition of sea ice and its tensile strength," in proceedings of Arctic Sea Ice. Easton, Md, 24-27 Feb 1958. Washington, D. C., National Academy of Sciences-National Research Council, Dec 1958, pp. 106-138. (Publication 598)
8. Naval Civil Engineering Laboratory. Technical Note N-653: NCEL ice and snow laboratory, by J. E. Dykins. Port Hueneme, Calif., Oct 1964.
9. ——. Technical Report R-396: Ice engineering - growth rate of sea ice in a closed system, by N. S. Stehle. Port Hueneme, Calif., Jun 1965.
10. K. O. Bennington. "Some crystal growth features of sea ice," Journal of Glaciology, vol 4, no. 36, Oct 1963, pp. 669-688.
11. I. Hawker and M. Mellor. "Deformation and fracture of ice under uniaxial stress," Journal of Glaciology, vol 2, no. 61, 1972.
12. Civil Engineering Laboratory. Technical Note N-1417: Ice engineering - elastic property studies on compressive sea ice specimens, by K. D. Vaudrey. Port Hueneme, Calif., Dec 1975.
13. N. H. Polakowski and E. J. Rippling. Strength and structure of engineering materials. Englewood Cliffs, N. J., Prentice-Hall, 1966.
14. Naval Civil Engineering Laboratory. Technical Note N-1310: Development of sea-ice strain transducer, by K. D. Vaudrey. Port Hueneme, Calif., Nov 1973.
15. D. J. Naus, G. B. Batson, and J. L. Lott. "Fracture mechanics of concrete," Fracture Mechanics of Ceramics, vol 2, edited by R. C. Bradt, et al. New York, N.Y., Plenum Press, 1974.
16. H. H. G. Jeileneck and R. Brill. "Viscoelastic properties of ice," Journal of Applied Physics, vol 27, no. 10, 1956, pp. 1198-1209.
17. T. Tabata. "Studies on viscoelastic properties of sea ice," Arctic Sea Ice. Washington, D.C., National Academy of Sciences - National Research Council, Dec 1958. (Publication 598.)
18. Army Cold Regions Research and Evaluation Laboratory. Research Report 196: Time dependent deflection of a floating ice sheet, by D. E. Nevel. Hanover, N.H., Jul 1966.
19. Civil Engineering Laboratory. Technical Memorandum M-61-76-3: Preliminary creep results from viscoelastic laboratory testing program, by K. D. Vaudrey. Port Hueneme, Calif., Mar 1976.
20. Naval Civil Engineering Laboratory. Technical Report R-641: Sea-ice bearing strength in Antarctica: Aircraft load curves for McMurdo ice runway, by J. E. Dykins. Port Hueneme, Calif., Sep 1969. (AD 694954)
21. Army Cold Regions Research and Evaluation Laboratory. Research Report 265: Concentrated Loads on Plates, by D. E. Nevel. Hanover, N. H., Mar 1970.

22. H. Hertz. "Über das Gleichgewicht schwimmender elastischer platten," Wiedemann's Annalen der Physik und Chemie, vol 22, 1884, pp. 449-455.
23. M. Wyman. "Deflections of an infinite plate," Canadian Journal of Research, vol 28, no. 3, sect. A, May 1950, pp. 293-302.
24. H. M. Westergaard. "Stresses in concrete pavements computed by theoretical analysis," Public Roads, vol 7, no. 2, Apr 1926, pp. 25-35.
25. E. L. Wilson. "Structural analysis of axisymmetric solids," American Institute of Aeronautics and Astronautics Journal, vol 3, no. 12, Dec 1965, pp. 2269-2274.
26. W. Flugge. Viscoelasticity. Waltham, Mass., Blaisdell Pub. Company, 1967.
27. R. M. Christensen. Theory of viscoelasticity. New York, N. Y., Academic Press, Inc., 1971.
28. Army Cold Regions Research and Evaluation Laboratory. Research Report 333: The bearing capacity of floating ice plates subjected to static or quasi-static loads, a critical survey, by A. D. Kerr. Hanover, N. H., Mar 1975.
29. R. M. W. Frederking and L. W. Gold. "The bearing capacity of ice covers under static loads," Canadian Journal of Civil Engineering, vol 3, no. 2, Jun 1976, pp. 288-293. (National Research Council of Canada, DBR Paper No. 676)
30. Naval Civil Engineering Laboratory. Technical Report R-189: Sea ice engineering summary report - Project ICE WAY, by W. E. Kingery et al. Port Hueneme, Calif., Sep 1962.
31. Civil Engineering Laboratory. Technical Note N-1431: Revised aircraft load curves and vehicle ice-thickness tables for annual ice sheet operations near McMurdo, Antarctica, by K. D. Vaudrey. Port Hueneme, Calif., Apr 1976.
- 32.———. Technical Report: A viscoelastic-plastic constitutive model with a finite element solution methodology, by M. G. Katona. Port Hueneme, Calif., (to be published).
33. R. L. Taylor. "An approximate method for thermoviscoelastic stress analysis," Nuclear Engineering and Design, vol 4, 1966, p. 21.

Appendix A

FINITE-ELEMENT COMPUTER CODE FOR ELASTIC ANALYSIS [4]

ANALYTICAL DEVELOPMENT

General

The main portion of the general axisymmetric finite element computer code employed in this study was written by Edward L. Wilson [25] and extended by M. G. Katona [4]. Formulation is based on the direct stiffness method with triangular or quadrilateral conical elements representing the axisymmetric structure. The structural system may be of complex configuration and composite construction, and the constitutive relations may be orthotropic, nonlinear, and temperature dependent. External loading may be mechanical or thermal in nature with an option to include body forces.

A special mesh generator was added to the program to facilitate input for the plate-shaped solids considered in this study. In addition, subroutines to simulate a fluid foundation and superposition of loads from arbitrary load configurations were incorporated into the main computer deck. These subroutines, as well as input instructions and examples, are discussed in the following sections.

Fluid Foundation

Development of the simulated fluid foundation was achieved by calculating a vertical resistance proportional to the displaced volume and adding it to the global stiffness matrix of the solid for every node on the solid-fluid interface. In formulating the vertical resistance, compatibility of displacements requires off-diagonal terms as well as diagonal terms; all of these terms are determined by energy principles consistent with the finite element formulation. The following derivation is based on these concepts.

Consider a solid supported by a fluid foundation with a typical node trio i, j, k and an arbitrary vertical displacement, Δ_j , at node j as shown in Figure A-1. Denoting the horizontal surface of a one-radian segment bounded by r_i and r_j as face **A**, and the horizontal surface bounded by r_j and r_k as face **B** the following relations are valid after point j deforms through the imposed displacement Δ_j .

Vertical displacements consistent with the finite element interpolation function along faces **A** and **B** are given by:

$$v_A(r) = \frac{r - r_i}{r_j - r_i} \Delta_j , \quad r_i \leq r \leq r_j$$

(A-1)

$$v_B(r) = \frac{r_k - r}{r_k - r_j} \Delta_j , \quad r_j \leq r \leq r_k$$

Vertical loading intensities along faces A and B are expressed as:

$$f_A(r) = \int_0^1 \gamma_w v_A(r) r d\theta = \gamma_w v_A(r) r , \quad r_i \leq r \leq r_j$$

(A-2)

$$f_B(r) = \int_0^1 \gamma_w v_B(r) r d\theta = \gamma_w v_B(r) r , \quad r_j \leq r \leq r_k$$

where γ_w = fluid density.

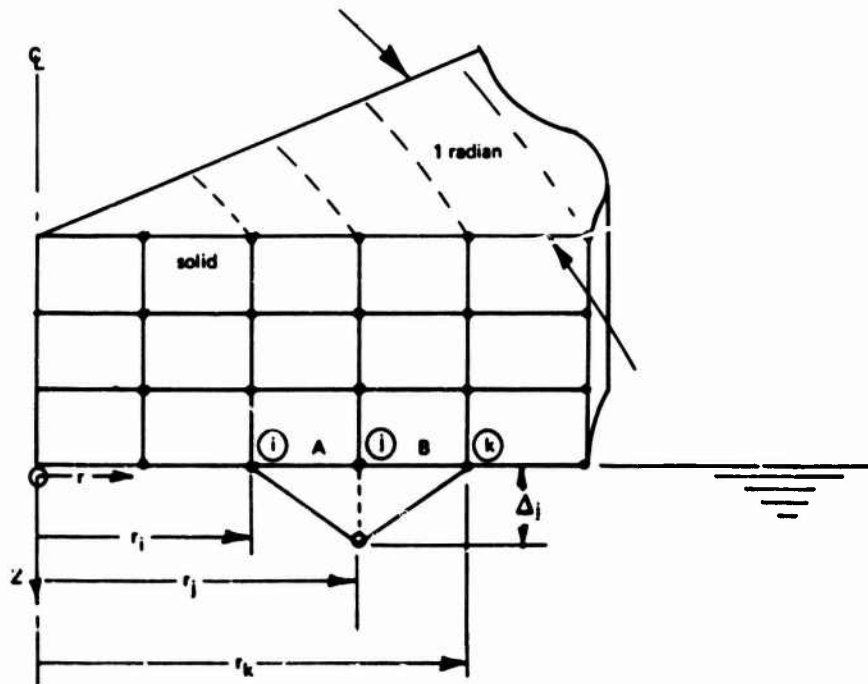


Figure A-1. Illustration of deformation from displacement, Δ_j .

The net vertical restoring forces on faces A and B are:

$$F_A = \int_{r_i}^{r_j} f_A(r) dr = \frac{\Delta_j \gamma_w}{12} (4r_j^2 - 2r_j r_i - 2r_i^2) \quad (A-3)$$

$$F_B = \int_{r_j}^{r_k} f_B(r) dr = \frac{\Delta_j \gamma_w}{12} (2r_k^2 + 2r_k r_j - 4r_j^2)$$

Next, energy principles are employed to determine kinematically equivalent nodal forces, F_{Ai} , F_{Aj} , F_{Bj} and F_{Bk} , depicted in Figure A-2 with the stipulation that:

$$\begin{aligned} F_{Ai} + F_{Aj} &= F_A \\ F_{Bj} + F_{Bk} &= F_B \end{aligned} \quad (A-4)$$

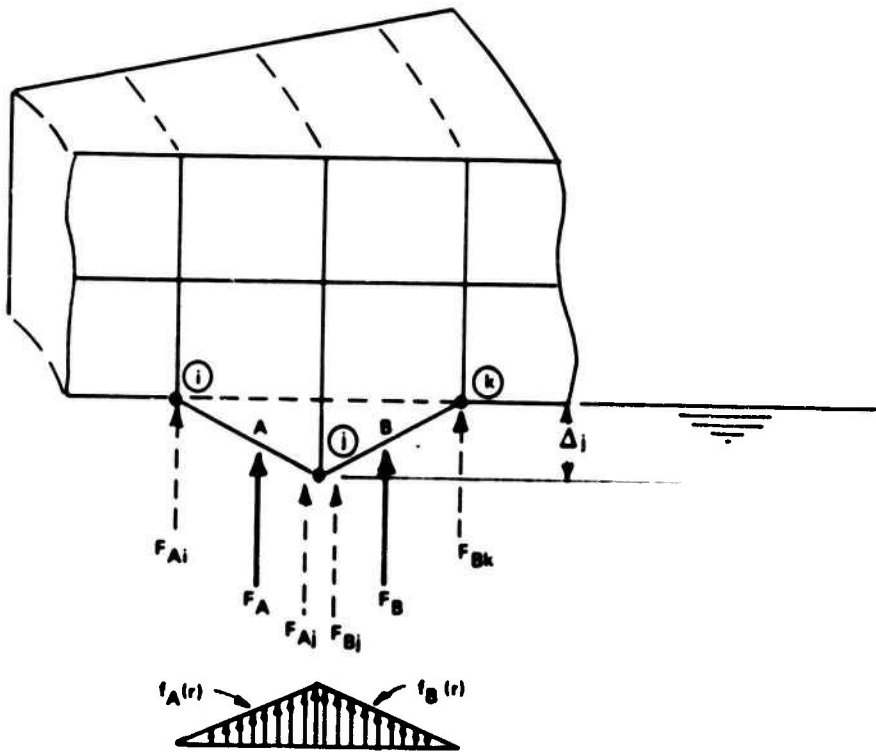


Figure A-2. Kinematically equivalent nodal forces.

Thus, for face A an impressed force, F_{Aj} , is sought which displaces a unit virtual load at node j through the distance Δ_j . The magnitude of this force can be determined by equating the virtual work of the unit load to the work of the virtual loading intensity along face A as it deforms under impressed load F_{Aj} . The virtual loading intensity is simply the ratio $1/F_{Aj}$ times the loading intensity given by Equation A-2. Therefore, the virtual work relation is given as:

$$1 \cdot \Delta_j = \int_{r_i}^{r_j} \int_0^{v_A(r)} \frac{1}{F_{Aj}} f_A(r) dz dr$$

which gives:

$$F_{Aj} = \frac{\Delta_j \gamma_w}{12} (3r_j^2 - 2r_j r_i - r_i^2) \quad (A-5)$$

By the same procedure the kinematically equivalent nodal force F_{Bj} can be determined. By applying Equations A-3 and A-4 the complete set of nodal forces can be determined as:

$$F_{Ai} = \frac{\Delta_j \gamma_w}{12} (r_j^2 - r_i^2)$$

$$F_{Aj} = \frac{\Delta_j \gamma_w}{12} (3r_j^2 - 2r_j r_i - r_i^2) \quad (A-6)$$

$$F_{Bi} = \frac{\Delta_j \gamma_w}{12} (-3r_j^2 + 2r_j r_k + r_k^2)$$

$$F_{Bj} = \frac{\Delta_j \gamma_w}{12} (r_k^2 - r_j^2)$$

Equations A-6 form the basis of the algorithm in the computer code for determining the stiffness additions representing the fluid foundation.

Superposition

The purpose of the superposition development is to determine the combined state of stress in a plate-solid resulting from an arbitrary loading configuration of circular loads. As is generally the case, the principle of

superposition has inherent limitations; first, the constitutive relations must be linear, and second, the plate-solid must be free of variations of material property and layer geometry with respect to any horizontal plane. Fortunately typical ice sheets are composed of horizontal layers which have material property variations and temperature changes solely in the vertical direction. Moreover, the "infinite" extent of the ice sheet nullifies the effect of boundaries confounding the superposition principle; hence, the only significant limitation is the restriction to linear stress-strain laws.

The process of determining the superimposed stress state begins by choosing a point in the plate-solid where the combined state of stress is to be calculated. The chosen point is referenced by an **XYZ** rectangular coordinate system at $(0, 0, z^*)$ where z^* is an explicit depth from the coordinate origin on the plate surface to the designated point in the plate-solid. Next, for each load, i , the load center is referenced by the coordinate pair (x_i, y_i) , then transformed to a local polar coordinate pair (r_i, θ_i) by the transformations:

$$r_i = \sqrt{x_i^2 + y_i^2}$$

$$\theta_i = \arctan(y_i/x_i)$$

The ordered pair (r_i, z^*) defines a corresponding coordinate point in the plate-solid of a single-load finite element program where stresses can be extracted from data storage. However, the local state of stress thus obtained is at angle θ_i with respect to the global **XYZ** coordinate system; consequently, a coordinate transformation is performed to determine the local state of stress in the global system. This process is repeated and the stress contribution of each load at the designated point is summed to yield the complete combined state of stress. Lastly, the principal stresses and unit normals are calculated from the complete combined state of stress.

DISCUSSION OF APPLICATION

General

Due to the general nature of the finite element code developed in this study, a variety of engineering investigations could be undertaken such as determining the effect of material and geometrical variations on the structural behavior of ice sheets. However, the objective of this Appendix is aimed at development of the analytical model rather than application. Thus, the limited number of test problems solved in this study are directed toward representation of an infinite boundary by a finite model.

Representation of an Infinite Boundary

For many applications an infinite expanse of ice is characteristic of the problem to be solved. In such cases defining an infinite expanse by an axisymmetric solid of finite extent is justifiable only if the boundary radius is chosen large enough so that changes in the boundary condition do not appreciably alter the structural response.

Preliminary investigations show that the structural response of typical ice sheets tends toward plate-theory behavior in the outer region beginning several loading radii away from the load center. Consequently, the minimum boundary radius required may be determined in terms of the plate-theory parameter, radius of relative stiffness, defined as:

$$\ell = \sqrt[4]{\frac{E h^3}{12(1-\mu^2)k}}$$

where ℓ = radius of relative stiffness

E = Young's modulus

h = thickness of plate

μ = Poisson's ratio

k = fluid density

Figure A-3 illustrates the variation in maximum tensile stress for a typical ice sheet and loading as a function of boundary length in units of ℓ . The three boundary conditions specified on the periphery which demonstrate convergence are (1) completely free, (2) horizontal fixed with vertical free, (3) completely fixed. As illustrated by the graphs, convergence occurs at approximately 10ℓ with the fixed-boundary condition converging fastest. Moreover, a maximum lower and a minimum upper bound is given by the fixed and free boundary conditions, respectively. Thus, in general, a boundary radius of 10ℓ with a fixed boundary condition will adequately represent an infinite ice sheet and, if desired, the accuracy may be tested by applying a free boundary condition to bracket the solution.

Although the method presented above will suffice for most applications, optimum use of the element is not being achieved in the outer regions where plate behavior is dominant. A higher degree of accuracy and saving of computer time could be realized by combining the Ritz method with the finite element technique in order to simulate the infinite boundary.

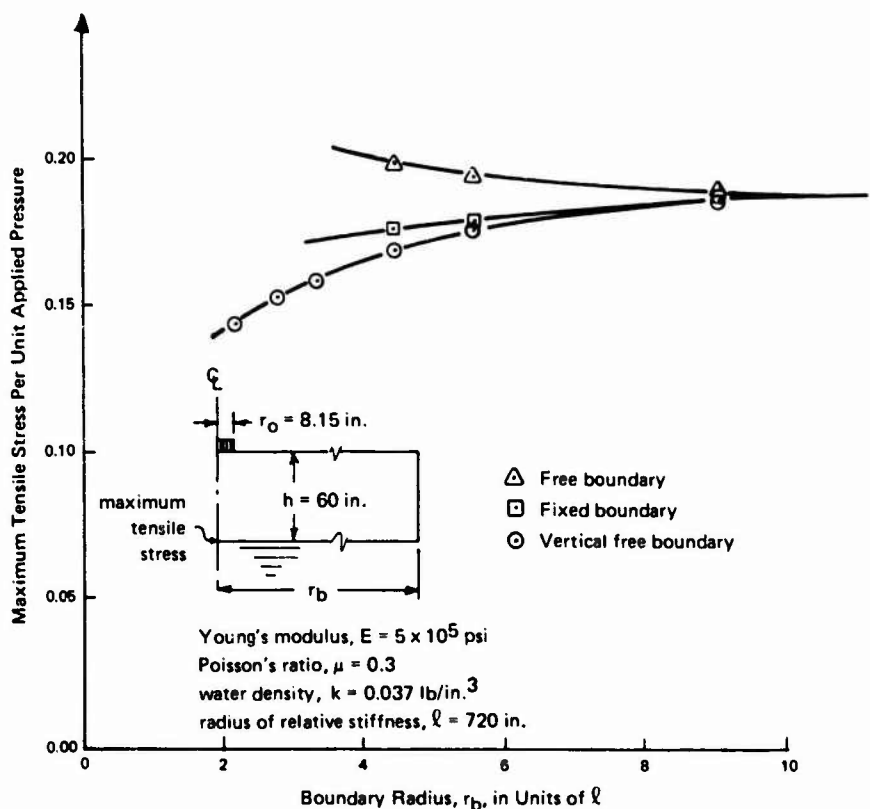


Figure A-3. Variation of maximum tensile stress for increasing boundary radius for typical ice sheet.

PROGRAM INPUT FOR PLATES ON FLUIDS

The input requirements are given for a circular, plate-shaped solid supported by a fluid foundation. The plate solid may be of arbitrary dimensions with as many as twelve material layers and can accommodate circular loadings of uniform pressure of arbitrary radius and magnitude. A superposition routine is available to determine the local state of stress resulting from any configuration of circular loadings at any desired point.

A. Identification Card (72H)

Columns 1 – 6 MESHGN (This activates mesh generator)
 7 – 72 Descriptive title of problem

B. Fluid Property Card (F10.0)

Columns 1 – 10 Density of supporting fluid

C. Control Card (10X, I5, 25X, F10.0, I5, 5X, I5)

Columns 11 – 15 Number of different material layers
(maximum of 12)

41 – 50 Reference temperature (stress-free
temperature)

51 – 55 Number of approximations (set to 1 for
elastic)

61 – 65 Boundary code: 0, 1, 2, or 3

0 – Nodes on periphery are free

1 – Nodes on periphery are vertically free
2 – Nodes on periphery are horizontally
free

3 – Nodes on periphery are fixed

D. Material Layer Properties – (one card per layer, followed by
temperature cards)

–First Card (2I5, 2F10.0, I10, 3F10.0)

Columns 1 – 5 Layer identification number (from 1 to 12)

6 – 10 Number of different temperatures for which
layer properties are given (8 maximum,
1 minimum)

11 – 20 Mass density of material (leave blank when
not considering body forces)

21 – 30 Ratio of plastic modulus to elastic modulus
(leave blank for elastic problem)

31 – 40 Number of element rows in this layer

41 – 50 Thickness of this layer

51 – 60 Temperature at top of layer

61 – 70 Temperature at bottom of layer

(Note: program will linearly distribute
temperature through the layer)

–Following Cards (one card-group for each temperature indicated
above) (8F10.0)

Columns 1 – 10 Temperature for which the following
properties are valid

11 – 20 Modulus of elasticity, E_r , and E_z

21 - 30 Poisson's ratio, ν_{rz}
31 - 40 Modulus of elasticity, E_θ
41 - 50 Poisson's ratio, $\nu_{\theta r}$ and $\nu_{\theta z}$
51 - 60 Coefficient of thermal expansion, α_r and α_z
61 - 70 Coefficient of thermal expansion, α_θ
71 - 80 Yield stress (leave blank for elastic case)

E. Mesh Generation Control Cards (2F10.0, 4I5)

Columns 1 - 10 Radius of loading
11 - 20 Pressure of loading
21 - 25 Number of radial elements under the load
26 - 30 Number of radial elements total
31 - 35 Number of loading radii to periphery (to represent an infinite plate this number should be at least ten times the radius of relative stiffness divided by the radius of loading)
36 - 40 Number of elements in contact with fluid foundation (in general set this equal to total number of radial elements)

F. Superposition Control Cards (I5, 2F10.0)

Columns 1 - 5 Number of circular loadings (number of wheels)
6 - 15 Total load (weight of aircraft)
16 - 25 Z-ordinate at which superposition is desired
(Note: The Z-ordinate in conjunction with the arbitrary surface coordinates, (x, y) define the spatial point, $(x, y, z) \leftrightarrow (0, 0, Z\text{-ord.})$, at which superposition will occur. The complete local state of stress will be determined and principal stresses with unit normals will be computed.)

-Individual wheel load characteristics---one card for each wheel
(3F10.0)

Columns 1 - 10 X-ordinate of load center
11 - 20 Y-ordinate of load center
21 - 30 Fraction of total load taken by this wheel

SAMPLE INPUT PROBLEMS

- I. A single wheel load of 8.15 inch radius and 200 psi pressure acting on a 60-inch-thick ice sheet of "infinite" extent.

1 MESHGN WHEEL OF A C-141 PLANE ON 60 INCHES OF ICE

2 0.037

3 1

1 3

4 1 1 10 60.0

5 500000. 0.3 500000. 0.3

6 8.15 200.0 5 20 880 20

7 1 21600. -60.

8 0.0 0.0 1.0

Comments:

1. In card #3 column #65, the boundary code of "3" signifies a fixed boundary which best represents the infinite boundary condition.
 2. In card #6, the infinite boundary is represented by 389 loading radii which was determined from 10 times the radius of relative stiffness divided by the loading radius. ($10 \times 720 / 8.15$)
 3. The superposition cards (#7 & 8) are trivial in this case since only one wheel is being considered. If the problem were to determine the maximum stress from the C-141 gear-group of four wheels, the superposition of maximum tensile stresses would be specified as follows:

Card #

7 4 86400. -60.

8 0.0 0.0 0.25

9 32.5 0.0 0.25

10 **0.0** **48.0** **0.25**

11 **32.5** **48.0** **0.25**

II. A single C-141 wheel load acting on a 60-inch-thick ice sheet composed of two different layers of material properties each 30 inches thick. There is a temperature differential across each layer which in turn affects the material properties.

Column #	1	5	10	15	20	25	30	35	40	45	50	55	60	65
Card #														
1	MESHGN TWO LAYERS OF ICE WITH TEMPERATURE DIFFERENTIAL													
2	0.037													
3			2								1		3	
4	1	3							5	30.0	-20.0		-10.0	
5	-25.0	600000.	0.3	600000.	0.3									
6	-15.0	550000.	0.3	550000.	0.3									
7	-5.0	520000.	0.3	520000.	0.3									
8	2	3						5	30.0	-10.	-10.		-0.0	
9	-15.0	510000.	0.3	510000.	0.3									
10	-5.0	490000.	0.3	490000.	0.3									
11	10.0	460000.	0.3	460000.	0.3									
12	8.15	200.0		5	20	880	20							
13	1	21600.	-60.											
14	0.0	0.0		1.0										

Appendix B

VISCOELASTIC ANALYTICAL FORMULATION AND COMPUTER CODE USER INSTRUCTION (5)

ANALYTICAL FORMULATION

The following discussion presents a brief description of the finite-element formulation implementing linear viscoelasticity and its associated assumption and limitations, and computer code user instructions developed by Katona (5). Viscoelastic materials are often called "memory" materials because the current state of stress in the material is determined not only by the current deformation, but also by all past deformation states. Moreover, the "memory" exhibits a fading phenomenon, since past deformations have less influence on the current stress state than do more recent deformation states.

Viscoelastic Representation

The above characteristics can be modeled either by differential or integral equations (26). The differential equation approach interprets the viscoelastic model in terms of a mechanical analogy composed of springs and dashpots. However, integral equations are more readily adaptable to laboratory testing results and, thus, easily applied to the solution of boundary value problems. An expression for stress as an integral function of any arbitrary strain input, $\epsilon(t)$, can be written as:

$$\sigma(t) = Y(t)\epsilon_0 + \int_0^t Y(t-\tau) \frac{\partial \epsilon(\tau)}{\partial \tau} d\tau \quad (B-1)$$

where ϵ_0 is the initial elastic strain, while $Y(t)$ is termed the relaxation function and is an inherent characteristic of the material model.

It is desirable here to elaborate on the merits of the integral form of Equation B-1. First, standard laboratory procedures for testing viscoelastic materials involve only direct measurement of the relaxation function (or its inverse, the creep function). A test specimen is subjected to a constant state of unit deformation, and the resulting stress is measured as a function of time. Clearly, it is not necessary to deduce an equivalent mechanical analog, since the laboratory data can be used directly in Equation B-1.

For isotropic materials, it can be shown that there are only two independent relaxation functions required to describe the constitutive relation. In solving boundary value problems, it is convenient to choose the relaxation functions as the responses to bulk and shear deformation. The bulk relaxation function, $K(t)$, is defined as the hydrostatic stress history due to a prescribed unit Heaviside volume deformation. Likewise, the shear relaxation function, $G(t)$, is defined as the shear stress history due to a prescribed unit Heaviside shear strain. Both $K(t)$ and $G(t)$ are positive, monotonically decreasing, independent relaxation functions. They can be written in the form of a prony series:

$$K(t) = K_0 + \sum_{i=1}^{m_K} K_i e^{-t/\lambda_i}; G(t) = G_0 + \sum_{i=1}^{m_G} G_i e^{-t/\beta_i} \quad (B-2)$$

Here, both relaxation functions are represented as a constant and summation of exponential terms; where $K_0, K_1, \dots, K_{m_K}, G_0, G_1, \dots, G_{m_G}$ are positive moduli constants with units of stress, and $\lambda_1, \dots, \lambda_{m_K}, \beta_1, \dots, \beta_{m_G}$ are positive constants referred to as "relaxation times."

In the Prony series form, the relaxation functions are capable of representing a large class of linear viscoelastic materials. In essence, any linear viscoelastic material which exhibits an instantaneous elastic deformation followed by a creep phase can be modeled by Equation B-2 with a sufficient number of exponential terms. In practice, it is seldom justified to use more than four exponential terms; usually two terms are sufficient. It can be noted that neither $K(t)$ nor $G(t)$ is the most convenient response for laboratory measurement, but converting normal laboratory results will be discussed later for specific viscoelastic saline-ice tests.

Displacement Method

In this derivation a brief outline of the finite element technique is presented, wherein quasi-static loading, small deformations, axisymmetric/plane strain geometry, and the absence of thermal effects are assumed. First, the viscoelastic constitutive relation of Equation B-1 can be presented as a matrix of Stieltjes integrals:

$$\{\sigma(t)\} = [D(t)] \{\epsilon(0)\} + \int_0^t [D(t-\tau)] \frac{\partial}{\partial \tau} \{\epsilon(\tau)\} d\tau \quad (B-3)$$

where $\{\sigma(t)\}$ is the stress vector at the current time, t ; $\{\epsilon(\tau)\}$ is the strain history vector for $0 \leq \tau \leq t$; and $[D(t-\tau)]$ is the constitutive matrix, composed of the two independent relaxation functions, $K(t)$ and $G(t)$, in the form of Equation B-2.

When this constitutive model is used in a displacement finite-element formulation based on virtual work, the resulting equilibrium equations have the form:

$$\int_0^t [K(t-\tau)] \frac{\partial}{\partial \tau} \{u(\tau)\} d\tau = \{R(t)\} \quad (B-4)$$

where $\{u(\tau)\}$ is the nodal point displacement history vector, $\{R(t)\}$ is the current load vector, and $[K(t-\tau)]$ is the viscoelastic stiffness-history matrix. For the sake of clarity, inertial terms are not included in Equation B-4 because they can be treated independently of the viscoelastic terms.

In order to solve Equation B-4 for the nodal displacements at the current time, $t = t_N$, a step-by-step numerical integration procedure must be employed. To this

end', the time integral is subdivided into n time increments and the time increment, Δt , is chosen sufficiently small to assume that the nodal displacements vary linearly within each time step. With this approximation, the nodal velocities $\partial/\partial\tau\{u(\tau)\}$ can be replaced by displacement increments for each time step, Δt_k , by $(1/\Delta t_k)\{\Delta u_k\}$. Next, by shifting all time-interval integrations to the right-hand side, except the current time interval, Δt_n , Equation B-4 can be expressed as

$$[K(\Delta t_n)]\{\Delta u_n\} = \{R(t_n)\} - \{H(t_n)\} \quad (B-5)$$

where $[K(\Delta t_n)]$ is the current viscoelastic stiffness matrix which is dependent only on the current time-step size, and $\{H(t_n)\}$ is the viscoelastic force-history vector dependent upon all past time steps,

$$\{H(t_n)\} = \sum_{k=1}^{n-1} [K(t_n - t_k)]\{\Delta u_k\} \quad (B-6)$$

Using Equation B-5, it is possible to solve for $\{\Delta u_n\}$ in a step-by-step fashion beginning with elastic solution, $n = 0$, and increasing n successfully through the time of interest while accumulating the incremental displacements. Since the current viscoelastic stiffness matrix is dependent only on the time-step size, the matrix need only be reformed and triangularized again when the size of time step is changed.

Although this procedure is tractable, the calculation of the force history vector in its defined form is computationally unpractical since it requires the storage of all past incremental displacements and the formation of new viscoelastic stiffness matrices at each time step. To circumvent this difficulty, a technique introduced by Taylor (33) can be exploited. Taylor's technique requires that the relaxation functions in Equation B-3 be in the form of a prony series, such as Equation B-2. When the relaxation functions are of the form given in Equation B-2, it is possible to restructure the force history vector as a summation of only $m_K + m_G + 1$ vectors rather than a summation of all history vectors. Moreover, the exponential form of the relaxation functions permits a simple recursion relationship for updating the force history vector at each time step.

Fluid Foundation

In the previous section, the viscoelastic boundary value problem was generated to include any arbitrary, axisymmetric or plane-strain, geometrical application. Now the geometry is specialized to plate-type structures, supported by a Winkler-type fluid foundation. By definition, a Winkler foundation produces a vertical resistance force proportional to the vertical displacement of the nodes at the plate-fluid interface. Consequently, these additional vertical nodal forces at the interface can be expressed as $[K_w]\{u_n\}$, where $[K_w]$ is a sparse global Winkler stiffness matrix with non-zero entries associated only with vertical displacements at the plate-fluid interface.

Considering Equation B-5 as a force equilibrium equation, the influence of the fluid foundation can be added directly to give:

$$[K(\Delta t_n)] \{ \Delta u_n \} + [K_w] \{ u_n \} = \{ R(t_n) \} - \{ H(t_n) \} \quad (B-7)$$

To complete the inclusion of the fluid foundation, the components of the Winkler stiffness matrix, $[K_w]$, need to be derived, consistent with the concept of virtual work.

Superposition of Loads

For this concept the geometry is assumed to be an axisymmetric, half-space system such that material properties vary only in the vertical direction, and the radial boundary extends to infinity (5). Loading is represented by uniform circular surface pressure discs, and their location is completely arbitrary. Specified load histories are assumed proportional to one another; in other words, the pressure of each disc, $p_i g(t)$, contains a pressure magnitude, p_i , and a loading history, $g(t)$, which is common to all discs. With the above assumptions, the state of stress under any pressure disc can be determined by solving for the stresses produced by that single disc and using stress transformations and superposition to calculate the stress contributions from all other discs.

USER INSTRUCTION FOR COMPUTER CODE

The following input instructions require some discussion with regard to attempting half-space boundary value problems and using the mesh generator. By definition, a half-space boundary value problem implies that the boundaries extend to infinity in one or two coordinate directions. However, the finite-element formulation used in this study requires selecting boundaries of some finite extent. In order to justify a finite boundary representing an infinite boundary, it is necessary to employ St. Venant's principle which contends that if the finite boundaries are chosen far enough away from the area of interest, then the boundaries and boundary conditions will have a negligible effect. For infinite plates on a fluid foundation, it has been found that selecting the outer radius of the plate at a distance ≥ 10 times the radius-of-relative-stiffness is sufficient. For a general half-space problem, several attempts of extending the boundaries may be required to demonstrate that the boundaries are not influencing the solution. The general mesh configuration of a plate is shown in Figure B-1.

USER INSTRUCTIONS FOR INPUT AND FORMATS FOR PROGRAM VISICE
BY M. G. KATONA (5)

VISICE IS A FINITE ELEMENT VISCOELASTIC PROGRAM DESIGNED TO SOLVE
FOR STRESSES IN AN AXISYMMETRIC, VISCOELASTIC, LAYERED PLATE
RESTING ON A WINKLER FOUNDATION SUBJECTED TO AN ARBITRARY
CONFIGURATION OF CIRCULAR SURFACE LOADS.

A. PROBLEM INITIATION AND MASTER CONTROL CARDS

CARD A1. (A6,11A6)

COL 1 TO 6 MESHGN, HOLLERITH WORD TO CALL MESH GENERATOR.
COL 7 TO 72 DESCRIPTIVE TITLE OF PROGRAM.

CARD A2. (2I5,3F10.0)

COL 1 TO 5 NUMAT, NUMBER OF MATERIAL LAYERS IN PLATE.
COL 6 TO 10 NSTEPS, TOTAL NUMBER OF TIME-STEPS.
COL 11 TO 20 DELT, TIME-STEP INCREMENT.
COL 21 TO 30 ACELZ, ACCELERATION IN Z-DIRECTION, (GRAVITY).
COL 31 TO 40 ANGFQ, ANGULAR VELOCITY (ROTATING PLATE)

CARD A3. (4F10.0,4I5)

COL 1 TO 10 RLOAD, LOADING RADIUS OF WHEEL (TIRE PRINT)
COL 11 TO 20 RMAX, RADIUS OF PLATE
COL 21 TO 30 PSI, PRESSURE OF TIRE PRINT
COL 31 TO 40 GAMMA, UNIT WEIGHT OF SUPPORTING FLUID.
COL 41 TO 45 NELOAD, NUMBER OF RADIAL ELEMENTS IN CONTACT
WITH ONE TIRE.
COL 46 TO 50 NUMELR, TOTAL NUMBER OF RADIAL SURFACE ELEMENTS
IN THE PLATE.
COL 51 TO 55 NUMSPG, TOTAL NUMBER OF RADIAL BOTTOM ELEMENTS
IN CONTACT WITH FLUID. (USUALLY, NUMSPG=NUMELR)
COL 56 TO 60 KBOUND, OUTER PERIPHERY BOUNDARY CODE...

- * KBOUND=0, OUTER EDGE IS FREE
- * KBOUND=1, OUTER EDGE IS HORIZONTALLY FIXED.
- * KBOUND=2, OUTER EDGE IS VERTICALLY FIXED.
- * KBOUND=3, OUTER EDGE IS COMPLETELY FIXED.
- *
- * NOTE, TO REPRESENT PLATES OF INFINITE EXTENT
- * IT IS RECOMMENDED TO CHOOSE KBOUND=3, AND
- * RMAX=10*RADIUS OF RELATIVE STIFFNESS

B. MATERIAL-LAYER CHARACTERIZATION (ONE GROUP B FOR EACH LAYER,M)

CARD B1. (I5,2F10.0,2I5,2F10.0)

COL 1 TO 5 NELAY(M), NUMBER OF ELEMENT ROWS IN THIS LAYER.
COL 6 TO 15 HEIGHT(M), THICKNESS OF THIS LAYER.
COL 16 TO 25 PO(M), DENSITY OF THIS LAYER. (BODY FORCES)
COL 26 TO 30 IB(M), NO. OF BULK EXPONENTIAL TERMS. (4 MAX)
COL 31 TO 35 IG(M), NO. OF SHEAR EXPONENTIAL TERMS. (4 MAX)
COL 36 TO 45 BK0(M), INFINITE-TIME BULK RELAXATION MOD.
COL 46 TO 55 GKO(M), INFINITE-TIME SHEAR RELAXATION MOD.

CARD B2. (8F10.0)

COL 1 TO 10 BK(MTYPE,1), BULK MOD. OF FIRST EXPONENTIAL.
COL 11 TO 20 BK(MTYPE,2), BULK RELAX. OF FIRST EXPONENTIAL.
COL 21 TO 30 BK(MTYPE,3), BULK MOD. OF SECOND EXPONENTIAL.
COL 31 TO 40 BK(MTYPE,4), BULK RELAX. OF SECOND EXPONENTIAL.
•
• CONTINUE AS REQUIRED FOR BULK EXPONENTIAL TERMS
•

CARD B3. (8F10.0)

COL 1 TO 10 GK(MTYPE,1), SHEAR MOD. OF FIRST EXPONENTIAL.
COL 11 TO 20 GK(MTYPE,2), SHEAR RELAX. OF FIRST EXPONENTIAL.
COL 21 TO 30 GK(MTYPE,3), SHEAR MOD. OF SECOND EXPONENTIAL.
COL 31 TO 40 GK(MTYPE,4), SHEAR RELAX. OF SECOND EXPONENTIAL.
•
• CONTINUE AS REQUIRED FOR SHEAR EXPONENTIAL TERMS
•

C. LOAD FACTOR CONTROL CARDS FOR TIME DEPENDENT LOADING.

CARD C1. (I5,2F10.0)

COL 1 TO 5 TLOAD, LOAD-CASE NO. FOR PROPORTIONAL LOADING.
COL 6 TO 15 T1, LOAD DURATION PARAMETER
COL 16 TO 25 T2, LOAD DURATION PARAMETER

★ TLOAD=1, CONSTANT LOAD OF DURATION T1.
★ TLOAD=2, TRIANGULAR LOAD, PEAK AT T1, STOP AT T2
★ TLOAD=3, SINE-SQUARED LOAD PERIOD OF T1.
★
★ THE ABOVE LOAD-CASES ARE NORMALIZED LOAD-
★ HISTORY FUNCTIONS WITH A MAXIMUM VALUE OF 1
★ WHICH MULTIPLY ALL EXTERNAL LOADS (PRESSURE
★ AND POINT FORCES). FOR EXAMPLE, A CONSTANT

* LOAD FOR ALL TIME WOULD BE DESIGNATED BY,
* TLOAD=1, AND T1=DELT*NSTEPS.
*
* ADDITIONAL LOAD-CASES MAY BE PROGRAMMED BY THE
* USER IN SUBROUTINE TLOAD.

D. OUTPUT CONTROL CARD

CARD D1. (7I5)

COL 1 TO 5 IPINT, PRINT INTERVAL IN TIME-STEPS.
COL 6 TO 10 NDISP1, FIRST NODE IN A SEQUENCE FOR DISP.
COL 11 TO 15 NDISP2, LAST NODE IN THE SEQUENCE FOR DISP.
COL 16 TO 20 NSTN1, FIRST ELEMENT IN A SEQUENCE FOR STRAIN.
COL 21 TO 25 NSTN2, LAST ELEMENT IN THE SEQUENCE FOR STRAIN.
COL 26 TO 30 NSTR1, FIRST ELEMENT IN A SEQUENCE FOR STRESS.
COL 31 TO 35 NSTR2, LAST ELEMENT IN THE SEQUENCE FOR STRESS.

* FOR EXAMPLE, IF PRINTED OUTPUT FOR EVERY THIRD
* TIME-STEP IS DESIRED, SUCH THAT, DISPLACEMENTS
* OF NODES 10 THROUGH 20 ARE PRINTED, NO STRAINS
* ARE PRINTED, AND STRESSES OF FIRST 5 ELEMENTS
* ARE PRINTED, THEN THE ABOVE PARAMETERS WOULD
* BE INPUT AS... IPINT=3, NDISP1=10, NDISP2=20,
* NSTN1=0, NSTN2=0, NSTR1=1, NSTR2=5.

E. SUPERPOSITION OF STRESSES CONTROL CARDS

CARD E1. (15)

COL 1 TO 5 INTSUP, SUPERPOSITION INTERVAL IN TIME-STEPS.
FOR EXAMPLE, IF THE SUPERIMPOSED STRESSES ARE
DESIRED OF EVERY FIFTH TIME-STEP, THEN INTSUP=5
INTSUP=0 RETURN TO MAIN PROGRAM.

CARD E2. (15,2F10.0)

COL 1 TO 5 NLOADS, NUMBER OF WHEELS
COL 6 TO 15 PTOTAL, TOTAL WEIGHT OF AIRPLANE. (FORCE)
COL 16 TO 25 ZPLANE, DEPTH BELOW THE PLATE SURFACE WHERE
SUPERPOSITION OF STRESSES IS DESIRED (NEGATIVE).
THE ACTUAL POINT, (X,Y,Z) IN THE PLATE WHERE
SUPERIMPOSED STRESSES ARE CALCULATED IS THE
POINT, (0,0,ZPLANE). THE VARIABLES X AND Y
DESCRIBE THE LOCATION OF THE WHEELS ON THE
PLATE SURFACE WITH RESPECT TO THIS POINT AND
ARE INPUT IN THE FOLLOWING CARDS.

CARD E3. (3F10.0) ONE CARD FOR EACH WHEEL TO BE SUPERIMPOSED.

COL 1 TO 10 XLOC(N), X-COORD. OF WHEEL LOAD CENTER
COL 11 TO 20 YLOC(N), Y-COORD. OF WHEEL LOAD CENTER
COL 21 TO 30 PLD(N), FRACTION OF TOTAL LOAD TAKEN BY WHEEL.

CARD E4. (I5) EXIT SUPERPOSITION AND RETURN TO MAIN PROGRAM

COL 1 TO 5 BLANK CARD SIGNALS EXIT.

- * PRIOR TO CARD E4., NEW SUPERPOSITION PROBLEMS
- * MAY BE DEFINED AND EXECUTED BY REPEATING CARDS
- * E1., E2., AND E3. THEREBY, THE USER MAY
- * DETERMINE THE SUPERIMPOSED STATE OF STRESS AT
- * NUMEROUS POINTS AND/OR FOR DIFFERENT WHEEL
- * CONFIGURATIONS AS LONG AS THE BASIC TIRE-PRINT
- * RADIUS IS THE SAME.

F. TERMINATION CARD (THIS CARD FOLLOWS LAST DATA DECK)

CARD F1. (A6)

COL 1 TO 6 STOP HOLLERITH WORD TO STOP EXECUTION.

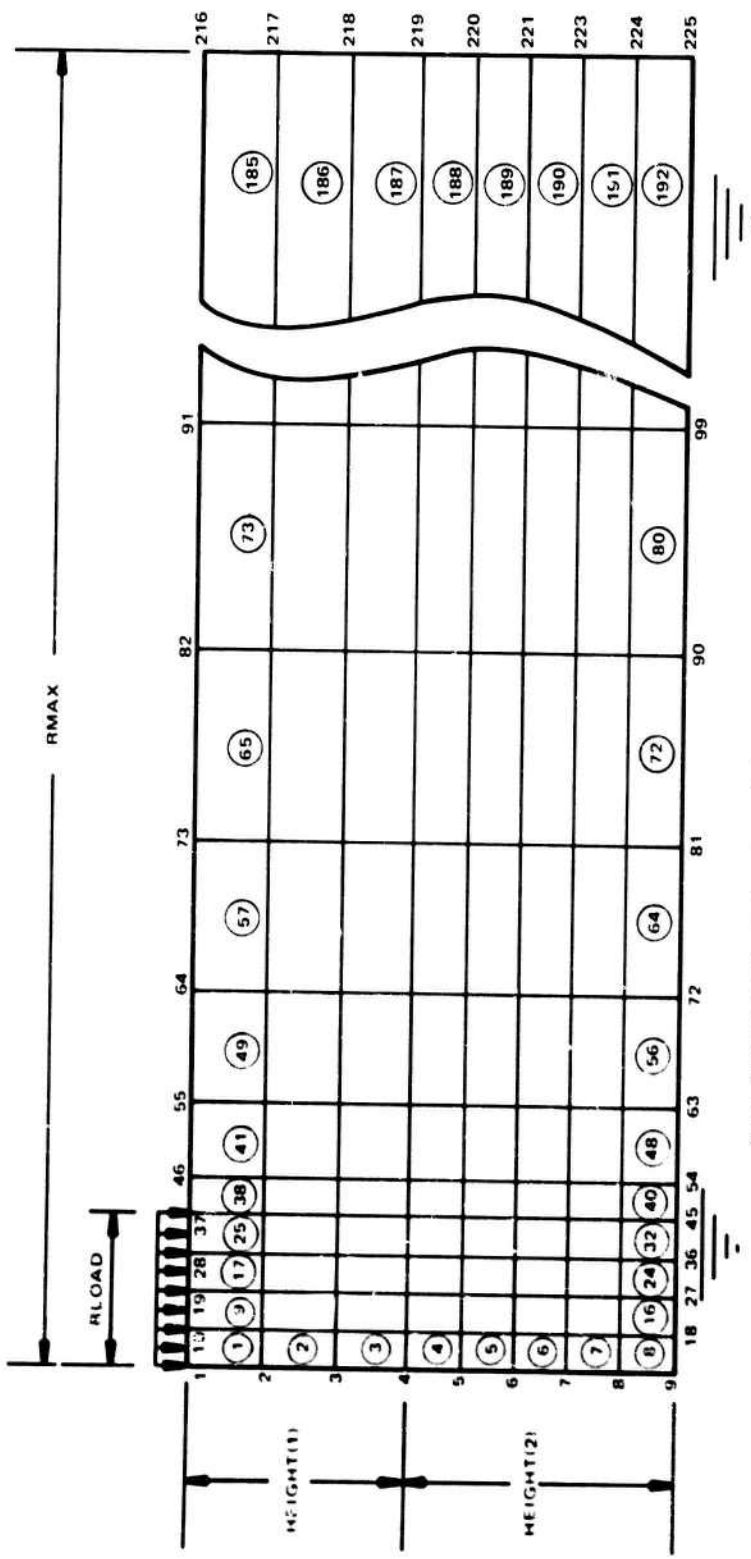


Figure B-1. Mesh configuration of a plate structure.

DISTRIBUTION LIST

AFB CESCH, Wright-Patterson; Stinfo Library, Offutt NE
ARMY BMDSC-RE (H. McClellan) Huntsville AL; DAEN-FEU, Washington DC; DAEN-MCE-D Washington DC
ARMY CORPS OF ENGINEERS MRD-Eng. Div., Omaha NE
ARMY CRREL A. Kovacs, Hanover NH; AK Proj. Off (P. Johnson), Fort Wainwright AK; Library, Hanover NH
ARMY ENVIRON. HYGIENE AGCY Water Qual Div (Doner), Aberdeen Prog Ground, MD
ASST SECRETARY OF THE NAVY Spec. Assist Energy (P. Waterman), Washington DC; Spec. Assist Submarines, Washington DC
MCB ENSS.D. Keisling, Quantico VA
CINCLANT Civil Engr. Supp. Plans, Offr Norfolk, VA
CNO Code NOP-964, Washington DC; Code OP 987 Washington DC; OP987J (J. Boosman), Pentagon
COMNAVBEACHPHIBREFTRAGRU ONE San Diego CA
DEFENSE DOCUMENTATION CTR Alexandria, VA
DTNSRDC Code 284 (A. Rufolo), Annapolis MD
MARINE CORPS BASE M & R Division, Camp Lejeune NC
MCAS Facil. Engr. Div. Cherry Point NC; J. Taylor, Iwakuni Japan; PWO Kaneohe Bay HI
NAF PWO, Atsugi Japan
NAS Code 18700, Brunswick ME; ENS Buchholz, Pensacola, FL; PWO. Glenview IL; SCE Norfolk, VA
NATL ACADEMY OF SCIENCES Polar Res Com (DeGoes)
NATL RESEARCH COUNCIL, Naval Studies Board, Washington DC
NAVAEROSPREGMEDCEN SCE, Pensacola FL
NAVAL FACILITY PWO, Barbados
NAVARCLAB CO, Pt Barrow AK
NAVCOASTSYSLAB Library Panama City, FL
NAVCOMMAREAMSTRSTA SCE Unit 1 Naples Italy
NAVCOMMSTA Code 401 Nea Makri, Greece; PWO, Exmouth, Australia
NAVEDTRAPRODEVCECEN Tech. Library
NAVENVIRHLTHCEN CO, Cincinnati, OH
NAVEODFAC Code 605, Indian Head MD
NAVFACENGCOM Code 043 Alexandria, VA; Code 044 Alexandria, VA; Code 0451 Alexandria, VA; Code 0454B Alexandria, Va; Code 1023 (T. Stevens) Alexandria, VA; Morrison Yap, Caroline Is.; P W Brewer, PC-22/E, Spencer) Alexandria, VA
NAVFACENGCOM - CHES DIV, Code FPO-IP4 (Gregory); Code FPO-ISP (Dr. Lewis) Wash, DC; Code FPO-IP12 (Mr. Scola), Washington DC
NAVFACENGCOM - LANT DIV, RDT&E/O 09P2, Norfolk VA
NAVFACENGCOM - NORTH DIV, Code 1028, RDT&E/O, Philadelphia PA
NAVFACENGCOM - PAC DIV, Code 402, RDT&E, Pearl Harbor HI; Commander, Pearl Harbor, HI
NAVFACENGCOM - WEST DIV, Code 04B; 09P/20; RDT&E/O Code 2011 San Bruno, CA
NAVFACENGCOM CONTRACT OICC, Southwest Pac, Manila, PI; ROICC (LCDR J.G. Leech), Subic Bay, R.P.; ROICC, Keflavik, Iceland
NAVNPWRU MUSE DET, Code NPU80 (ENS W. Morrison), Port Hueneme CA
NAVOCANO Code 1600 Bay St. Louis, MS; Code 3408 (J. Kravitz) Bay St. Louis
NAVOCTRANSYSCEN Code 52 (H. Talkington) San Diego CA; Code 6565 (Tech. Lib.), San Diego CA
NAVPETRIS Director, Washington DC; No 4 Anchorage AK
NAVPGSCOL, Code 1424 Monterey, CA; E. Thornton, Monterey CA
NAVPHIBASE CO, ACH 2 Norfolk, VA; Code SIT, Norfolk VA
NAVSEASYSOM Code 00C (L.T.R. MacDougal), Washington DC
NAVSEC Code 715 (J. Quirk) Panama City, FL
NAVSHIP PYD PWD (L.T.N. B. Hall), Long Beach CA; Tech Library, Vallejo, CA
NAVSTA PWO, Mayport FL; Utilities Engr Off. (L TJG A.S. Ritchie), Rota Spain
NAVSUBASE L.TJG D.W. Peck, Groton, CT
NAVSUPPACT CO, Brooklyn NY; Code 413, Seattle WA; L.TJG McGarrah, Vallejo CA
NAVSURFWPNCEN PWO, White Oak, Silver Spring, MD; Silver Spring MD
NAVTECHTRACEN SCE, Pensacola FL
NAWPNCEN Code 2636 (W. Bonner), China Lake CA
NAWPNSTA PW Office (Code 09C1) Yorktown, VA; PWO, Seal Beach CA

NAVWPNSUPPCEN Code 09 (Boennighausen) Crane IN
NCBC CEL (CAPTN. W. Petersen), Port Hueneme, CA; CEL AOIC Port Hueneme CA; Code 10 Davisville, RI;
Code 155, Port Hueneme CA
NCR 20, Commander
NSF Polar Info Service
NTC Code 54 (ENS P. G. Jackel), Orlando FL
NUSC Code 131 New London, CT
OCEANNAV Mangmt Info Div., Arlington VA
ONR BROFF, CO Boston MA; Code 461, Arlington VA (McGregor); Code 481, Arlington VA; Code 700F Arlington
VA
PMTC Pat. Counsel, Point Mugu CA
PWC CO Norfolk, VA; CO, Great Lakes IL; Code 116 (LTJG. A. Eckhart) Great Lakes, IL; Code 120C (Library) San
Diego, CA; Code 220.I, Norfolk VA; Code 30C (Boettcher) San Diego, CA
U.S. MERCHANT MARINE ACADEMY Kings Point, NY (Reprint Custodian)
US DEPT OF COMMERCE NOAA, Pacific Marine Center, Seattle WA
USCG (G-MP-3/USP/82) Washington DC
USCG R&D CENTER Tech. Dir. Groton, CT
USNA Ocean Sys. Eng Dept (Dr. Monney) Annapolis, MD
LIBRARY OF CONGRESS WASHINGTON, DC (SCIENCES & TECH DIV)
MICHIGAN TECHNOLOGICAL UNIVERSITY Houghton, MI (Haas)
MIT Cambridge MA; Cambridge MA (Rm 10-500, Tech. Reports, Engr. Lib.)
NATL ACADEMY OF ENG. ALEXANDRIA, VA (SEARLE, JR.)
UNIV. NOTRE DAME Notre Dame, IN
OREGON STATE UNIVERSITY CORVALLIS, OR (CE DEPT, BELL); Corvalis OR (School of Oceanography)
PURDUE UNIVERSITY Lafayette, IN (Altschaeffl); Lafayette, IN (CE Engr. Lib)
STANFORD UNIVERSITY STANFORD, CA (DOUGLAS)
TEXAS A&M UNIVERSITY COLLEGE STATION, TX (CE DEPT)
UNIVERSITY OF ALASKA Arctic Data Center; Doc Collections Fairbanks, AK
UNIVERSITY OF CALIFORNIA BERKELEY, CA (CE DEPT, GERWICK)
UNIVERSITY OF ILLINOIS Metz Ref Rm, Urbana IL; URBANA, IL (NEWARK)
UNIVERSITY OF NEBRASKA-LINCOLN Lincoln, NE (Ross Ice Shelf Proj.)
UNIVERSITY OF WASHINGTON (FH-10, D. Carlson) Seattle, WA; SEATTLE, WA (APPLIED PHYSICS LAB);
Seattle, WA (OCEAN ENG RSCH LAB, GRAY); Seattle WA (E. Linger)
AMOCO PROD. CO (Cox) Res. Dept, Tulsa, OK
ATLANTIC RICHFIELD CO. DALLAS, TX (SMITH)
BECHTEL CORP. SAN FRANCISCO, CA (PELPS)
CANADA Library, Calgary, Alberta; Lockheed Petrol. Srv. Ltd., New Westminster BC; Mem Univ Newfoundland
(Chari), St John's; Surveyor, Nenninger & Chenevert Inc., Montreal; Warnock Hersey Prof. Srv Ltd, La Sale,
Quebec
CHEVRON OIL FIELD RESEARCH CO. LA HABRA, CA (BROOKS)
CONCRETE TECHNOLOGY CORP. TACOMA, WA (ANDERSON)
DRAVO CORP Pittsburgh PA (Giannino)
GULF SCI.& TECH CO (Vaudrey), Houston, TX
JAMESCO, R. Girdley, Orlando FL
MARATHON OIL CO Houston TX (C. Seay)
MARINE CONCRETE STRUCTURES INC. MEFARIE, LA (INGRAM)
MEDALL & ASSOC. INC. J.T. GAFFEY II SANTA ANA, CA
NORWAY J. Creed, Skr
OFFSHORE DEVELOPMENT ENG. INC. BERKELEY, CA
RAYMOND INTERNATIONAL INC. CHERRY HILL, NJ (SOIL TECH DEPT)
SHELL DEVELOPMENT CO. Houston TX (C. Sellars Jr.); Houston, TX (Earle)
SHELL OIL CO. Houston TX (R. de Castongre, Jr.); 1 Boaz, Houston TX
SWEDEN VBB (Library), Stockholm
UNITED KINGDOM Cement & Concrete Assoc (G. Somerville) Wexham Springs, Slough; Cement & Concrete Assoc.
(Lit. Ex), Bucks; Taylor, Woodrow Constr (014P), Southall, Middlesex
BRAHTZ La Jolla, CA
BULLOCK La Canada
R. F. BESIER Old Saybrook CT
CEC Donofrio, John L., ENS